SURFACE FUNCTIONALIZATION OF TiO_2 NANOPARTICLES: PHOTO-STABILITY AND REACTIVE OXYGEN SPECIES (ROS) GENERATION

By

Kacie M. Louis

A dissertation submitted in partial fulfillment of the

requirements for the degree of

Doctor of Philosophy

(Chemistry)

at the

UNIVERSITY OF WISCONSIN-MADISON

2012

Date of Final oral examination: 06/19/12

The dissertation is approved by the following members of the Final oral committee:

Robert J. Hamers, Professor, Chemistry
Joel Pedersen, Associate Professor, Soil Science
Gilbert Nathanson, Professor, Chemistry
John C. Wright, Professor, Chemistry
Ralph Albrecht, Professor, Animal Sciences

Abstract

Surface Functionalization of TiO_2 Nanoparticles: Photo-stability and Reactive Oxygen Species (ROS) Generation

Kacie M. Louis

Under the supervision of Professor Robert J. Hamers

University of Wisconsin-Madison

Metal oxide nanoparticles are becoming increasingly prevalent in society for applications of sunscreens, cosmetics, paints, biomedical imaging, and photovoltaics. Due to the increased surface area to volume ratio of nanoparticles compared to bulk materials, it is important to know the health and safety impacts of these materials.

One mechanism of toxicity of nominally "safe" materials such as TiO_2 is through the photocatalytic generation of reactive oxygen species (ROS). ROS production and ligand degradation can affect the bioavailability of these particles in aqueous organisms. We have investigated ROS generation by functionalized TiO_2 nanoparticles and its influence on aggregation and bioavailability and toxicity to zebrafish embryos/larvae. For these studies we investigated anatase TiO_2 nanoparticles. For application purposes and solution stability, the TiO_2 nanoparticles were functionalized with a variety of ligands such as citrate, 3,4-dihydroxybenzaldehyde, and ascorbate. We quantitatively examined the amount of ROS produced in aqueous solution using fluorescent probes and see that more ROS is produced under UV light than in the dark control.

Our measurements show that TiO_2 toxicity reaches a maximum for nanoparticles with smaller diameters, and is correlated with surface area dependent changes in ROS generation. In an effort to reduce toxicity through control of the surface and surface ligands, we synthesized anatase nanoparticles of different sizes, functionalized them with different ligands, and examined the resulting ROS generation and ligand stability.

Using a modular ligand containing a hydrophobic inner region and a hydrophilic outer region, we synthesized water-stable nanoparticles, via two different chemical reactions, having much-reduced ROS generation and thus reduced toxicity. These results suggest new strategies for making safer nanoparticles while still retaining their desired properties. We also examine the degradation of the different ligands on the surface of the particles using XPS and FTIR. The combination of ROS production and ligand degradation can affect the bioavailability of these particles in aqueous species.

Acknowledgements

After 5 years of graduate school and 4 years of undergraduate school, it seems almost impossible to fit all the acknowledgements of the people who supported me through this journey in such a short amount of space.

I want to first start out by thanking my undergraduate chemistry professors, Dr. Byron, Dr. Scamehorn, Dr. Katahira, and Dr. Iimura. Without them I would never have learned I had a huge love for chemistry and I would not have discovered that I was fully capable of surviving graduate school.

And of course, I am eternally thankful of my PhD advisor Professor Robert Hamers. On November 1, 2007, I couldn't have picked a better advisor and group to work with. First of all, we share the best qualities of both being from Wisconsin and naturally being die-hard Packer fans. On top of that, he has further extended by appreciation for chemistry and all sciences. Throughout the 5 years, Bob has been a constant image of optimism and brilliance while showing me the tools of research. He has also demonstrated the importance of family, friends, and life.

My project involved a great deal of collaboration with various groups, and I would never have made it through all the biology terms without the help of Sarah and Paige. I also want to thank the whole NSEC Thrust 4 for insightful and fruitful conversations about science. I would also like to thank Rob McClain, Jackie Bastyr-Cooper, and Monika Ivancic for help with instrumentation and analysis.

I also owe my survival over the last 5 years to the support and friendship of every single one of my group-mates, past and present. I thank Drew for showing me the ropes

with nanoparticle synthesis and teaching me how to navigate the Hamers labs. I want to thank Rose for her love and adoration of my puppy Havarti and Michelle for being the best bowling partner I've ever had. And of course I will never forget, I want to thank Mike for all the friendship, support, and fun times we had together…I miss you bud.

. Now my officemates, what to say about them? Ryan, Beth, Joe, Becca, and Linghong, thank you for putting up with me in the office for all these years. I could not have asked for a more awesome group of people. We have struggled together and celebrated our successes together and watched terrible music videos together. Those will be some of the most memorable times of my life. Thank you.

Most of all I want to thank my family. This has been a long journey for all of us. My mom has dealt with my tear-filled calls and my detailed stories about how awesome my research is. Mom, dad, g-ma, Katie, Cory, David, Hudson, and Brandon thank you for the support, the hugs, the food, and the laughter, I can honestly say I would not be who I am without every one of you. And since I'm from a close knit family, this also extends to all my aunts, uncles, and cousins. Last but not least, thank you to my wonderful dog for being the joy I needed in life (and for putting up with me spending more time typing on the computer lately). I love you all.

Table of Contents

Chapter 1

Introduction and Background

1.1 Introduction to Nanoscale Materials

Nanomaterials are defined as having at least one dimension in the range of 1 to 100 nm.(*1*, *2*) Although nanomaterials have been used for hundreds of years as dyes, the modern emergence of nanotechnology began in the 1980s with the invention of the scanning tunneling microscope in 1981 by Gerd Binnig and Heinrich Rohrer and the discovery of fullerenes in 1985 by Harry Kroto, Richard Smalley, and Robert Curl.(*3*) However, the first use of the idea, later termed nanotechnology, was introduced by physicist Richard Feynman who gave a talk at the American Physical Society meeting at CalTech in 1959 titled "There's Plenty of Room at the Bottom." This talk focused on the ability to manipulate materials at the atom or molecular scale and that at this scale gravity would become less important as surface tension and Van der Waals interactions become more important. In the 1980s, Dr. K. Eric Drexler authored books titled "Engines of Creation: The Coming Era of Nanotechnology" and "Nanosystems: Molecular Machinery, Manufacturing, and Computation" where the former is considered the first book on the topic of nanotechnology.(*4*, *5*)

The nanodomain deals with nanoparticles, nanofibers, nanowires, thin films, and a variety of other morphologies. Nanomaterials have attracted attention due to the fascinating electronic, optical, magnetic, and catalytic properties that are associated with their nanoscale dimensions.(*1*, *2*) Once materials are in the nanometer range, one can manipulate their properties by size and shape control.

The stability of a colloid system is determined by a balance between the attractive van der Waals forces which want to cause aggregation and the repulsive electrostatic forces which keep the particles apart. This interplay is known as the Derjaguin-Landau-Verwey-Overbeek (DLVO) theory which describes the forces between two charged surfaces interacting in a liquid medium.(*6*) Colloid suspensions are not thermodynamically stable; therefore a "stabile" suspension refers to a suspension that is sustained over a given period of time. Once the particles have fallen into the primary minimum of DLVO, the particles are agglomerated and unable to be separated. However, there is a secondary minimum where the particles are aggregated but can be agitated by an external force to separate the particles. For good suspension, typically the colloids need to have a large surface charge with an expanded double layer (the surface charge with the corresponding layer of counter charges). The mobilization and stability, however, are dependent not only on surface charge but also on colloid-surface contact, grain size, flow rate, and chemical properties of the solution.(*1*, *6*)

To maintain stability of colloids in a solvent, the repulsive forces must dominate. To do this there are two primary mechanisms: steric and electrostatic repulsion. For steric repulsion, large organic molecules (i.e. polymers) are adsorbed onto the surface of the particles, preventing the surfaces of the particles from coming into contact. The thickness of the organic layer needs to be sufficient to ensure the van der Waals forces will be weak. For electrostatic repulsion, a distribution of charges is formed on the surface through either pH or charged organic ligands. Nanoparticles have a specific pH

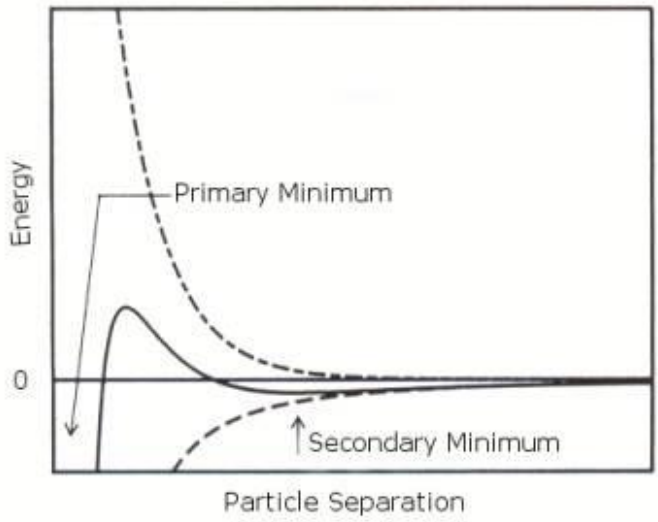

Figure 1.1: Derjaguin-Landau-Verwey-Overbeek (DLVO) theory which describes the forces between two charged surfaces interacting in a liquid medium.

where the net charge on the surface is zero, which is called the point of zero charge (PZC).(*3,4*) At this point the particles will not repel each other and will irreversibly agglomerate. Below the PZC the charge on the particles is positive and above it the charge is negative; in both these cases the particles electrostatically repel each other.

1.2 Synthesis and Functionalization of Metal Oxide Nanomaterials

Metal oxide nanoparticles are attractive for many applications including catalysis, sensors, electronic materials, and environmental remediation.(*8–16*) Controlled synthesis of these materials is important for success in these applications. A number of synthetic approaches fully investigated and reported in the literature include flame aerosol, sol-gel, hydrolysis, chemical vapor deposition, and various others.(*17–32*) As Oskam describes, solution-phase methods provide a large degree of control over the synthesis products including the nanoparticle size.(*33*)

The solution-based synthesis of nanoparticles can be described in four steps: precursor formation, nucleation, growth, and aging as shown in Figure 1.2. The graph described each of the four steps in terms of precursor concentration and time. The precursor groups are commonly formed via hydroxylation and hydrolysis reactions. Then condensation of M-OH_2 and HO-M groups and condensation of 2M-OH groups contribute to the nucleation of a solid material. There are two main growth mechanisms. If the incorporation of atoms is slow, the growth is kinetically limited, whereas if the incorporation of atoms is fast, growth is diffusion limited. The two different mechanisms lead to different particle size distributions. Kinetically limited particles tend to have larger size distributions since the growth rate is dependent on the surface area leading to

faster growth of the larger particles. The diffusion limited growth mechanism has a greater impact on smaller particles leading to a narrowing of the size distribution. For metal oxide synthesis, diffusion-limited growth is generally expected. After growth, the particle sizes can change by the aging process, normally Ostwald ripening and aggregation.(*33*)

Size control once the growth of the nanoparticles is complete can be accomplished using surface functionalization with organic molecules. In addition to size control, functionalization can also stabilize nanoparticles in colloidal suspensions by adding steric or ionic repulsion and can also be useful for the applications of the nanoparticles. Several approaches have been studied for the formation of molecular layers on the surface of metal oxides.(*20*, *25*, *26*, *30*, *34–47*) These surface functionalizations of metal oxides have commonly been performed using carboxylic acids, catechols, phosphonates, amines, thiols, and silanes as the anchoring groups to the surface. Recently the Hamers group has been exploring possible ways of creating more stable linkages to the surface including photochemical grafting(*48–50*) and thermal grafting through Williamson Ether type reactions.(*51*)

1.2 Photocatalysis of TiO_2

The heterogeneous photocatalytic properties of titanium dioxide were discovered in 1972 by Fujishima and Honda with the splitting of water on TiO_2 electrodes.(*52*) In a heterogeneous photocatalysis system, the photoinduced molecular transformations occur at the surface of the catalyst.(*52*) In the case of a catalyzed photoreaction, the initial

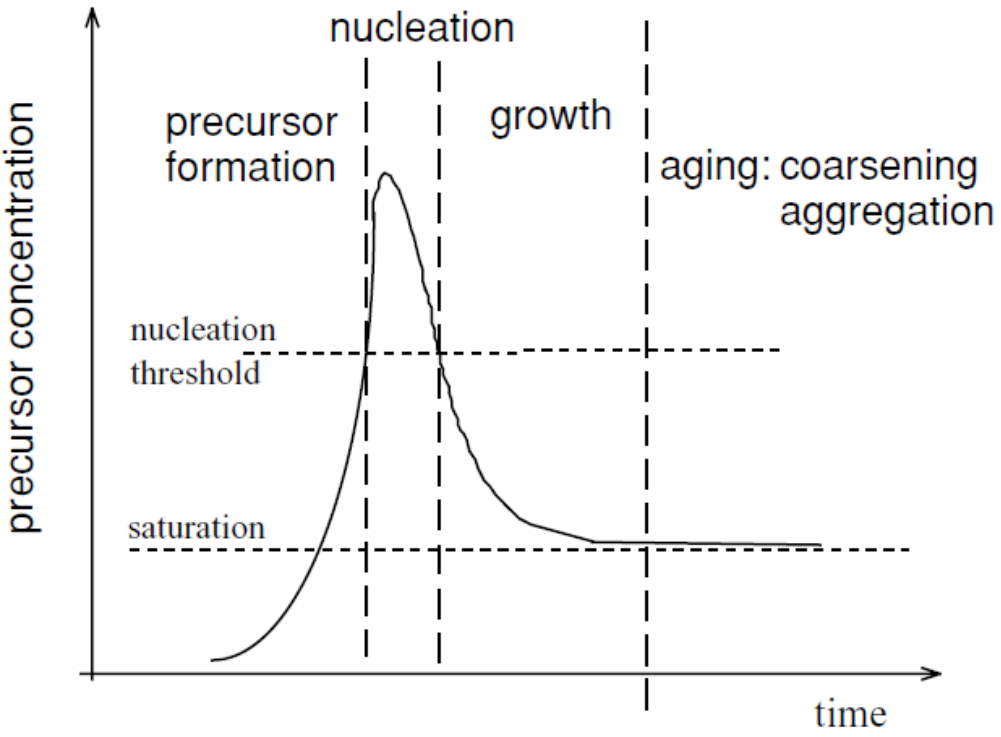

Figure 1.2: Precursor concentration versus time for the precursor formation nucleation, growth and aging of nanoparticles synthesized using a solution-based method.(*33*)

photoexcitation occurs in an adsorbed molecule which then interacts with the ground state of the catalyst substrate. For a sensitized photoreaction, the excitation takes place in the catalyst substrate and then transfers an electron into the ground state of the adsorbed molecule. It is the subsequent electron transfer that leads to the chemical reactions in the heterogenous photocatalysis system. A good photocatalyst maximizes the efficiency of the electron-hole reactions and has little recombination resulting in heat dissipation.(*52–58*)

As a photocatalyst, TiO_2 produces reactive oxygen species (ROS) when exposed to light at or above its band-gap (3.2 eV or 386 nm for the anatase phase) where the electron can reduce molecular oxygen into the superoxide anion ($O_2^{\cdot -}$) and the hole can oxidize water into hydroxyl radicals ($OH^{\cdot}$). It is also possible for the hole to directly oxidize organic material at the surface of the TiO_2, which can be advantageous for the destruction of organic compounds in polluted air and wastewaters.(*11*)

1.3 Introduction to the Health and Safety of Nanoscale Materials

Titanium dioxide (TiO_2) nanoparticles are becoming more prevalent in society in a variety of applications including electronics, food packaging, paint, cosmetics, sunscreens, and waste water treatments.(*8–11*, *13–16*, *59*) By 2015, Nel et al predict the sale of products using nanotechnology may reach $1 trillion.(*13*) The chemical and physical properties of nanoparticles are primarily determined by their size, shape, composition, reactivity, and surface chemistry.(*2*, *13*) For these reasons, it is important to know if there is a difference in the toxicity of the materials in the nanoscale regime compared to the bulk regime.

Although there is increasing use of TiO_2 nanoparticles, there is still little known about the health and safety of these materials. Due to the expected growth of the field and also the increased public exposure to nanomaterials, from both intentional (direct use of sunscreens or cosmetics on the skin) and inadvertent contact (leaching of materials into water streams), it is necessary to improve characterization and toxicity screening tools for these materials.

Although TiO_2 has been shown to be non-toxic as a bulk material and in the dark, the photoactivation of TiO_2, resulting in the generation the reactive oxygen species $O_2^{\cdot -}$ and $OH^{\cdot}$, could have adverse effects.(*60*) Reactive oxygen species (ROS) are known to cause oxidative stress and therefore can cause toxicity in organisms. The oxidative stress and ultimate toxicity of various commercial TiO_2 nanoparticles have been studied in zebrafish and other organisms.(*10, 13, 14, 16, 61–69*) For these specific samples, the addition of simulated light has shown an increase in the toxicity and malformations in the zebrafish.(*69*)

Due to the increased surface area to volume ratio, there are more reactive surface sites on nanoparticles than for the same mass of bulk materials, increasing the chances for the production of ROS. Also because of the increased surface area to volume ratio, surface functionalization has been shown to change the properties of a variety of nanomaterials.(*2*)

1.4 Scope of Thesis

This thesis presents a study on the determination and prevention of reactive oxygen species generation by titanium dioxide nanoparticles based on variety of

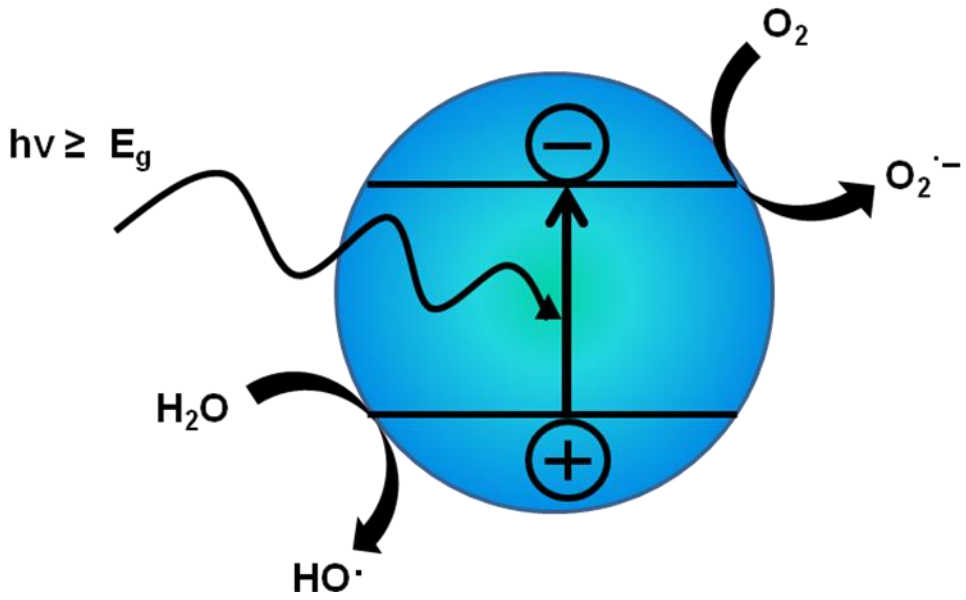

Figure 1.3: Photoactivation of TiO_2. When light above the band gap of TiO_2 is absorbed by the material, an electron is excited into the conduction band and can reduce molecular oxygen into a superoxide anion and the hole can react oxidize water to form hydroxyl radicals. These are known as reactive oxygen species.

conditions including size and surface functionalization. This study concentrates on the molecular scale of what is causing ROS generation with the intention of controlling those parameters to ultimately reduce ROS production and toxicity. Chapter 2 describes the synthetic, surface functionalization, and characterization procedures used to reproducibly control the nanoparticles examined. With interest being at the molecular scale, small chemical or environmental changes between sample to sample can lead to large differences in the reactive oxygen species generation results. Chapter 3 contains detailed investigations into the role solution and nanoparticle parameters play in the generation of reactive oxygen species and also giving insight into better experimental design. These conditions include the presence of a buffer, nanoparticle size, excess organic ligand, and ligand degradation. Chapter 4 discusses the use of surface chemistry not only to determine but to also decrease ROS generation. This is done by developing a modular ligand composed of hydrophobic and hydrophilic groups that can be altered based on the application of the particles. Chapter 5 contains information on computational studies of ligand stability on metal oxide surfaces to be used as a comparison to experimental results.

1.5 References

(1) Birdi, K. S. *Handbook of Surface and Colloid Chemistry*; 3rd ed.; CRC Press: Boca Raton, FL, 2009.

(2) Grassian, V. H. When size really matters: Size-dependent properties and surface chemistry of metal and metal oxide nanoparticles in gas and liquid phase environments. *Journal of Physical Chemistry C* **2008**, *112*, 18303-18313.

(3) Kroto, H. W.; Heath, J. R.; O'Brien, S. C.; Curl, R. F.; Smalley, R. E. C60: Buckminsterfullerene. *Nature* **1985**, *318*, 162-163.

(4) Drexler, K. E. *Nanosystems: Molecular machinery, manufacturing, and computation*; Wiley & Sons: New York, 1992.

(5) Drexler, K. E. *Engines of creation: The coming era of nanotechnology*; 1986.

(6) Buff, H., Graf, K., Kappl, M. *Physics and Chemistry of Interfaces*; 2nd ed.; Wiley-VCH, 2006.

(7) Vayssieres, L. On the effect of nanoparticle size on water-oxide interfacial chemistry. *Journal of Physical Chemistry C* **2009**, *113*, 4733-4736.

(8) Auffan, M.; Pedeutour, M.; Rose, J.; Masion, A.; Ziarelli, F.; Borschneck, D.; Chaneac, C.; Botta, C.; Chaurand, P.; Labille, J.; Bottero, J.-Y. Structural degradation at the surface of a TiO(2)-based nanomaterial used in cosmetics. *Environmental Science & Technology* **2010**, *44*, 2689-94.

(9) Fenoglio, I.; Greco, G.; Livraghi, S.; Fubini, B. Non-UV-induced radical reactions at the surface of TiO_2 nanoparticles that may trigger toxic responses. *Chemistry* **2009**, *15*, 4614-21.

(10) Jones, C. F.; Grainger, D. W. In vitro assessments of nanomaterial toxicity. *Advanced Drug Delivery Reviews* **2009**, *61*, 438-56.

(11) Kiser, M. A.; Westerhoff, P.; Benn, T.; Wang, Y.; Pérez-Rivera, J.; Hristovski, K. Titanium nanomaterial removal and release from wastewater treatment plants. *Environmental Science & Technology* **2009**, *43*, 6757-63.

(12) Liu, X.; Chen, G.; Su, C. Effects of material properties on sedimentation and aggregation of titanium dioxide nanoparticles of anatase and rutile in the aqueous phase. *Journal of Colloid and Interface Science* **2011**, *363*, 84-91.

(13) Nel, A.; Xia, T.; Mädler, L.; Li, N. Toxic potential of materials at the nanolevel. *Science* **2006**, *311*, 622-7.

(14) Sanders, K.; Degn, L. L.; Mundy, W. R.; Zucker, R. M.; Dreher, K.; Zhao, B.; Roberts, J. E.; Boyes, W. K. In vitro phototoxicity and hazard identification of nano-scale titanium dioxide. *Toxicology and Applied Pharmacology* **2012**, *258*, 226-36.

(15) Teow, Y.; Asharani, P. V.; Hande, M. P.; Valiyaveettil, S. Health impact and safety of engineered nanomaterials. *Chemical Communications* **2011**, *47*, 7025-38.

(16) Turkez, H. The role of ascorbic acid on titanium dioxide-induced genetic damage assessed by the comet assay and cytogenetic tests. *Experimental and Toxicologic Pathology* **2011**, *63*, 453-7.

(17) Madhusudan Reddy, K. Preparation, characterization, and spectral studies on nanocrystalline anatase TiO_2. *Journal of Solid State Chemistry* **2001**, *158*, 180-186.

(18) Okuyama, K.; Wuled Lenggoro, I. Preparation of nanoparticles via spray route. *Chemical Engineering Science* **2003**, *58*, 537-547.

(19) Park, H. K.; Park, K. Y. Vapor-phase synthesis of uniform silica spheres through two-stage hydrolysis of SiCl4. *Materials Research Bulletin* **2008**, *43*, 2833-2839.

(20) Chen, X.; Mao, S. S. Titanium dioxide nanomaterials: synthesis, properties, modifications, and applications. *Chemical Reviews* **2007**, *107*, 2891-959.

(21) Liqiang, J.; Xiaojun, S.; Weimin, C.; Zili, X.; Yaoguo, D. The preparation and characterization of nanoparticle TiO_2 / Ti films and their photocatalytic activity. *Journal of Physics and Chemistry of Solids* **2003**, *64*, 615-623.

(22) Briesen, H.; Fuhrmann, A.; Pratsinis, S. E. The effect of precursor in flame synthesis of SiO_2. *Chemical Engineering Science* **1998**, *53*, 4105-4112.

(23) Dai, Y.; Cobley, C. M.; Zeng, J.; Sun, Y.; Xia, Y. Synthesis of anatase TiO_2 nanocrystals with exposed {001} facets. *Nano Letters* **2009**, *9*, 2455-9.

(24) Ehrman, S. H.; Friedlander, R. S. K.; Zachariahs, M. R. Characteristics of SiO_2/TiO_2 nanocomposite particles formed in a premixed flat flame. *Journal of Aerosol Science* **1998**, *29*, 687-706.

(25) Kotsokechagia, T.; Cellesi, F.; Thomas, A.; Niederberger, M.; Tirelli, N. Preparation of ligand-free TiO_2 (anatase) nanoparticles through a nonaqueous process and their surface functionalization. *Langmuir* **2008**, *24*, 6988-97.

(26) Trewyn, B. G.; Slowing, I. I.; Giri, S.; Chen, H.-T.; Lin, V. S.-Y. Synthesis and functionalization of a mesoporous silica nanoparticle based on the sol-gel process and applications in controlled release. *Accounts of Chemical Research* **2007**, *40*, 846-53.

(27) Yan, X.; Pan, D.; Li, Z.; Liu, Y.; Zhang, J.; Xu, G.; Wu, M. Controllable synthesis and photocatalytic activities of water-soluble TiO_2 nanoparticles. *Materials Letters* **2010**, *64*, 1833-1835.

(28) Joo, J.; Yu, T.; Kim, Y. W.; Park, H. M.; Wu, F.; Zhang, J. Z.; Hyeon, T. Multigram scale synthesis and characterization of monodisperse tetragonal zirconia nanocrystals. *Journal of the American Chemical Society* **2003**, *125*, 6553-7.

(29) Niederberger, M.; Garnweitner, G. Organic reaction pathways in the nonaqueous synthesis of metal oxide nanoparticles. *Chemistry* **2006**, *12*, 7282-302.

(30) Taylor, S.; Qu, L.; Kitaygorodskiy, A.; Teske, J.; Latour, R. a; Sun, Y.-P. Synthesis and characterization of peptide-functionalized polymeric nanoparticles. *Biomacromolecules* **2004**, *5*, 245-8.

(31) Yu, M.-Z.; Lin, J.-Z.; Chan, T.-L. Effect of precursor loading on non-spherical nanoparticle synthesis in a diffusion flame reactor. *Chemical Engineering Science* **2008**, *63*, 2317-2329.

(32) Hu, M. Z.-C.; Harris, M. T.; Byers, C. H. Nucleation and growth for synthesis of nanometric zirconia particles by forced hydrolysis. *Journal of Colloid and Interface Science* **1998**, *198*, 87-99.

(33) Oskam, G. Metal oxide nanoparticles: synthesis , characterization and application. *Journal of Sol-Gel Science Technology* **2006**, *37*, 161-164.

(34) Araujo, P. Z.; Morando, P. J.; Blesa, M. a Interaction of catechol and gallic acid with titanium dioxide in aqueous suspensions. 1. Equilibrium studies. *Langmuir* **2005**, *21*, 3470-4.

(35) Bélanger, D.; Pinson, J. Electrografting: a powerful method for surface modification. *Chemical Society Reviews* **2011**, *40*, 3995-4048.

(36) Creutz, C.; Chou, M. H. Binding of catechols to mononuclear titanium(IV) and to 1- and 5-nm TiO_2 nanoparticles. *Inorganic Chemistry* **2008**, *47*, 3509-14.

(37) Dobson, K. D.; Mcquillan, A. J. In situ infrared spectroscopic analysis of the adsorption of aromatic carboxylic acids to TiO_2, ZrO_2, Al_2O_3, and Ta_2O_5 from aqueous solutions. *Spectrochimica Acta Part A* **2000**, *56*, 557 - 565.

(38) Gao, W.; Dickinson, L.; Grozinger, C.; Morin, F. G.; Reven, L. Self-assembled monolayers of alkylphosphonic acids on metal oxides. *Langmuir* **1996**, *12*, 6429-6435.

(39) Hug, S.; Bahnemann, D. Infrared spectra of oxalate, malonate and succinate adsorbed on the aqueous surface of rutile, anatase and lepidocrocite measured with

in situ ATR-FTIR. *Journal of Electron Spectroscopy and Related Phenomena* **2006**, *150*, 208-219.

(40) Martin, S. T.; Kesselman, J. M.; Park, D. S.; Lewis, N. S.; Hoffmann, M. R. Surface structures of 4-chlorocatechol adsorbed on titanium dioxide. *Environmental Science & Technology* **1996**, *30*, 2535-2542.

(41) Mcnamara, W. R.; Milot, R. L.; Song, H.-eun; Iii, R. C. S.; Batista, V. S.; Schmuttenmaer, C. A.; Brudvig, G. W.; Crabtree, R. H. Water-stable , hydroxamate anchors for functionalization of TiO_2 surfaces with ultrafast interfacial electron transfer. *Energy & Environmental Science* **2010**, *3*, 917-923.

(42) Mendive, C. B.; Bredow, T.; Feldhoff, A.; Blesa, M. a; Bahnemann, D. Adsorption of oxalate on anatase (100) and rutile (110) surfaces in aqueous systems: Experimental results vs. theoretical predictions. *Physical Chemistry Chemical Physics* **2009**, *11*, 1794-808.

(43) Mudunkotuwa, I. a; Grassian, V. H. Citric acid adsorption on TiO_2 nanoparticles in aqueous suspensions at acidic and circumneutral pH: surface coverage, surface speciation, and its impact on nanoparticle-nanoparticle interactions. *Journal of the American Chemical Society* **2010**, *132*, 14986-94.

(44) Pettibone, J. M.; Cwiertny, D. M.; Scherer, M.; Grassian, V. H. Adsorption of organic acids on TiO_2 nanoparticles: effects of pH, nanoparticle size, and nanoparticle aggregation. *Langmuir* **2008**, *24*, 6659-67.

(45) Rajh, T.; Chen, L. X.; Lukas, K.; Liu, T.; Thurnauer, M. C.; Tiede, D. M. Surface restructuring of nanoparticles: An efficient route for ligand−metal oxide crosstalk. *The Journal of Physical Chemistry B* **2002**, *106*, 10543-10552.

(46) Schmuck, C.; Schwegmann, M. A molecular flytrap for the selective binding of citrate and other tricarboxylates in water. *Journal of the American Chemical Society* **2005**, *127*, 3373-9.

(47) Stone, A. T. Adsorption of catechols , metal (hydr) oxide / water interface: Effect of ring substituents on the adsorption onto TiO_2. *Environmental Science & Technology* **1996**, *30*, 1604-1613.

(48) Franking, R. a; Landis, E. C.; Hamers, R. J. Highly stable molecular layers on nanocrystalline anatase TiO_2 through photochemical grafting. *Langmuir* **2009**, *25*, 10676-84.

(49) Franking, R.; Hamers, R. J. Ultraviolet-induced grafting of alkenes to TiO_2 surfaces: Controlling multilayer formation. *Journal of Physical Chemistry C* **2011**, *115*, 17102-17110.

(50) Li, B.; Franking, R.; Landis, E. C.; Kim, H.; Hamers, R. J. Photochemical grafting and patterning of biomolecular layers onto TiO_2 thin films. *ACS Applied Materials & Interfaces* **2009**, *1*, 1013-22.

(51) Chen, J.; Franking, R.; Ruther, R. E.; Tan, Y.; He, X.; Hogendoorn, S. R.; Hamers, R. J. Formation of molecular monolayers on TiO_2 surfaces: a surface analogue of the Williamson ether synthesis. *Langmuir* **2011**, *27*, 6879-89.

(52) Fujishima, A., Honda, K. Electrochemical photolysis of water at a semiconductor electrode. *Nature* **1972**, *238*, 37-38.

(53) Thompson, T. L.; Yates, J. T. Surface science studies of the photoactivation of TiO_2--new photochemical processes. *Chemical Reviews* **2006**, *106*, 4428-53.

(54) Berger, T.; Sterrer, M.; Diwald, O.; Knözinger, E.; Panayotov, D.; Thompson, T. L.; Yates, J. T. Light-induced charge separation in anatase TiO_2 particles. *The Journal of Physical Chemistry B* **2005**, *109*, 6061-8.

(55) Hagfeldt, A.; Graetzel, M. Light-induced redox reactions in nanocrystalline systems. *Chemical Reviews* **1995**, *95*, 49-68.

(56) Diebold, U. The surface science of titanium dioxide. *Surface Science Reports* **2003**, *48*, 53-229.

(57) Davydov, L. Quantification of the primary processes in aqueous heterogeneous photocatalysis using single-stage oxidation reactions. *Journal of Catalysis* **2000**, *191*, 105-115.

(58) Linsebigler, A. L.; Lu, G.; Yates, J. T. Photocatalysis on TiO_2 surfaces: principles, mechanisms, and selected results. *Chemical Reviews* **1995**, *95*, 735-758.

(59) Liu, Y.; Liu, C.-yan; Zhang, Z.-ying Effects of carboxylic acids on the microstructure and performance of titania nanocrystals. *Chemical Engineering Journal* **2008**, *138*, 596-601.

(60) Aruoja, V.; Dubourguier, H.-C.; Kasemets, K.; Kahru, A. Toxicity of nanoparticles of CuO, ZnO and TiO_2 to microalgae *Pseudokirchneriella subcapitata*. *The Science of the total environment* **2009**, *407*, 1461-8.

(61) Karlsson, H. L.; Gustafsson, J.; Cronholm, P.; Möller, L. Size-dependent toxicity of metal oxide particles--a comparison between nano- and micrometer size. *Toxicology Letters* **2009**, *188*, 112-8.

(62) Heinlaan, M.; Ivask, A.; Blinova, I.; Dubourguier, H.-C.; Kahru, A. Toxicity of nanosized and bulk ZnO, CuO and TiO_2 to bacteria *Vibrio fischeri* and crustaceans *Daphnia magna* and *Thamnocephalus platyurus*. *Chemosphere* **2008**, *71*, 1308-16.

(63) Fabian, E.; Landsiedel, R.; Ma-Hock, L.; Wiench, K.; Wohlleben, W.; van Ravenzwaay, B. Tissue distribution and toxicity of intravenously administered titanium dioxide nanoparticles in rats. *Archives of Toxicology* **2008**, *82*, 151-7.

(64) Warheit, D. B.; Hoke, R. a; Finlay, C.; Donner, E. M.; Reed, K. L.; Sayes, C. M. Development of a base set of toxicity tests using ultrafine TiO_2 particles as a component of nanoparticle risk management. *Toxicology Letters* **2007**, *171*, 99-110.

(65) Chen, J.; Zhou, H.; Santulli, A. C.; Wong, S. S. Evaluating cytotoxicity and cellular uptake from the presence of variously processed TiO_2 nanostructured morphologies. *Chemical Research in Toxicology* **2010**, *23*, 871-9.

(66) Sayes, C. M.; Wahi, R.; Kurian, P. a; Liu, Y.; West, J. L.; Ausman, K. D.; Warheit, D. B.; Colvin, V. L. Correlating nanoscale titania structure with toxicity: a cytotoxicity and inflammatory response study with human dermal fibroblasts and human lung epithelial cells. *Toxicological Sciences* **2006**, *92*, 174-85.

(67) Wang, J.; Zhou, G.; Chen, C.; Yu, H.; Wang, T.; Ma, Y.; Jia, G.; Gao, Y.; Li, B.; Sun, J.; Li, Y.; Jiao, F.; Zhao, Y.; Chai, Z. Acute toxicity and biodistribution of different sized titanium dioxide particles in mice after oral administration. *Toxicology Letters* **2007**, *168*, 176-85.

(68) Baccheta, R., Santo, N., Fascio, U., et al. Nano-sized CuO, TiO_2 and ZnO affect *Xenopus laevis* development. *Nanotoxicology* **2012**, *6*, 381-398.

(69) Bar-Ilan, O.; Louis, K. M.; Yang, S. P.; Pedersen, J. A; Hamers, R. J.; Peterson, R. E.; Heideman, W. Titanium dioxide nanoparticles produce phototoxicity in the developing zebrafish. *Nanotoxicology* **2011**, *Early Online*, 1-10.

Chapter 2

Synthesis, Surface Functionalization, and Characterization of TiO_2 Nanoparticles

2.1 Introduction

Several processes have been previously developed for the synthesis of TiO_2 and other metal oxide nanoparticles that can be categorized into two main categories: bottom-up and top-down approaches.(*1*) Top-down applies to the disintegration of bulk materials into smaller pieces by milling or lithography processes. Bottom-up approaches are methods where a new nanoparticle phase is created due to a phase separation process from the supersaturated mother phase. This is caused by a change in a physical parameter such as pressure or temperature, or by changes in chemical composition such as mixing with a poor solvent or chemical reaction. These approaches include flame aerosol, sol-gel, hydrolysis, and chemical vapor deposition.(*2–19*) The physical properties of nanoparticles are dependent on the synthesis used. These physical properties include phase, size, shape (morphology), defect density, and surface speciation. In 2007, Chen and Mao summarized the different synthetic routes for TiO_2 along with the corresponding material properties.(*19*) The resulting material properties play a significant role in the reaction pathways of TiO_2 nanoparticles.(*20*) TiO_2 can be found in the rutile, anatase and brookite phases, with rutile and anatase being the most common. For bulk materials, rutile is the thermodynamically stable phase and anatase is kinetically stable at room temperature, where at high temperatures anatase converts into rutile. However, for nanoparticles less than 14 nm in diameter, anatase is more stable

than rutile.(*21*) For many types of studies, it is also crucial to not only control the size of the particles, but also the size dispersity. The morphology of the nanoparticles depends on the reaction conditions. Common structures include spherical particles, rods, wires and platelets. The surface species of the nanoparticles can also change depending on the starting materials of the synthesis. These surface species can affect subsequent surface functionalizations as well as the ultimate behavior of the particles. The synthetic route used for this study is a non-aqueous solution-based method which provides well-defined crystalline anatase nanoparticles with control over size, followed by a water-based procedure where hydrolyzable surface groups are removed to yield "ligand-free" nanoparticles.(*6*)

Several approaches have been studied for the formation of molecular layers on the surface of TiO_2. These surface functionalizations of TiO_2 have commonly been performed using carboxylic acids, catechols, phosphonates and silanes as the anchoring groups to the surface. Recently the Hamers group has been exploring possible ways of creating more stable linkages to the surface including photochemical grafting(*22–24*) and thermal grafting through Williamson Ether type reactions.(*25*)

For this research, surface functionalization of TiO_2 nanoparticles was done using carboxylates and catechols as the primary anchoring group to the surface. A number of studies have looked at the details of these types of functionalizations.(*6*, *26–39*) The single-molecule ligands originally examined for this study include citrate, 3,4-dihydroxybenzaldehyde, and ascorbate. Citrate is naturally abundant in the environment and is often used in nanomaterial syntheses to give control over size, morphology, and

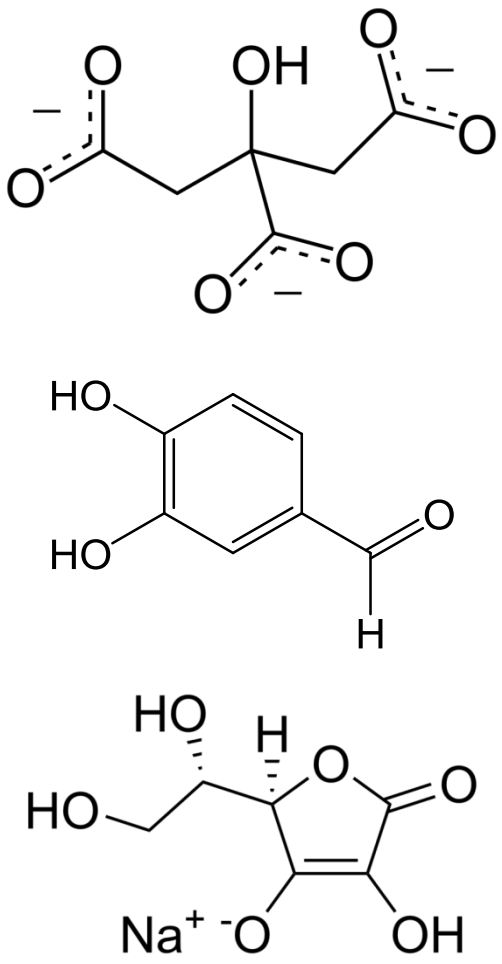

Figure 2.1: Chemical structures of citrate, 3,4-dihydroxybenzaldehyde, and sodium ascorbate.

solution stabilization.(*40*) For carboxylate functionalizations, an ionic bond is formed between one or both of the carboxyl oxygen atoms and one or two titanium atoms of the surface. Therefore, it is important to create a positively charged surface and a negatively charged molecule. The point of zero charge (PZC) of the material is the pH at which the particles have zero net charge. To get a positive surface, the solution pH needs to be lower than the PZC of the TiO_2. For TiO_2, that can range from pH values of 2.9 to 6.4 but can be higher for nanoparticles.(*41*, *42*) For the particles used in this study, the point of zero charge is around pH 5-6.(*6*) For a negatively charged molecule, the solution pH needs to be above the pKa of the acid. Therefore, the functionalization solutions should be kept at a pH that is between the pKa of the acid and the PZC of the nanoparticle.

Catechol (1,2-dihydroxybenzene) is a diprotic weak acid that prevails in the undissociated form over a wide pH range (pK_{a1}=9.2, pK_{a2}=13.0) and has been shown to form stable complexes with aqueous Ti (IV).(*27*, *36*) Stone et al. have shown that the catechol group binds to the surface with both ionic and covalent contributions, but is mainly controlled by ionic interactions.(*38*) The adsorption of catechol molecules is dependent on the pH of the functionalization solution, increasing in efficiency as the pH increases and reaching a plateau between the first and second pK_a values of the molecule which is above the point of zero charge of the surface. From computational studies, the adsorption stoichiometry that best fits the experimental data is a reaction between one ligand anion, one H^+, and one neutral surface site. (*38*)

This chapter aims to address the importance and details of a well-controlled and reproducible TiO_2 nanoparticle synthesis and functionalization, with emphasis on the

molecular interactions. The nanoparticles are fully characterized to give a complete picture of nanoparticle-ligand system for further applications shown in Chapters 3 and 4.

2.2 Experimental Methods

2.2.1 Chemicals

For the synthesis, $TiCl_4$ was purchased from Sigma-Aldrich (208556) is ReagentPlus® 99.9% trace metals basis, anhydrous benzyl alcohol purchased from Sigma-Aldrich (305197) is 99.8% pure, and 200 proof ethanol was purchased from Decon Laboratories Inc. (2716). Functionalization molecules included sodium citrate (51804, Sigma), 3,4-dihydroxybenzaldehye 97% (D108405, Aldrich), and (+)-sodium L-ascorbate (A7631, Sigma). All water used is brought to 18.0-18.2 MΩ-cm resistivity using a Barnstead NANOpure Infinity ultrapure water system with an organic-free filter cartridge. A 0.5 M sodium hydroxide solution was made using NaOH (S318, Fisher Scientific) in 18 MΩ-cm H_2O. HCl 37% (320321, Sigma Aldrich) and HNO_3 (NX0409, EMD) was used in full concentration.

2.2.2 Synthesis of TiO_2 Nanoparticles

The TiO_2 nanoparticles used for this study were based on the synthesis by Kotsokechagia et al.(*6*) In a round bottom flask, 5 mL of neat $TiCl_4$ were added to 25 mL of anhydrous ethanol to create titanol. After 2 minutes of stirring, 100 mL of anhydrous benzyl alcohol were added to the solution as the reaction medium. The solution was heated at 85°C for 6.5 hours after which the solution became cloudy and was transferred to centrifuge tubes with 15 mL of solution in each. The particles were precipitated out of

solution using a 1:2 (v:v) ratio of diethyl ether to nanoparticle suspension. The mixture was centrifuged at 4000 g for 10 minutes or until the supernatant was clear and the nanoparticles created a white solid pellet at the bottom. The liquid supernatant was decanted, and the nanoparticles were suspended by sonication in a 1:1 (v:v) solution of 18 MΩ-cm H_2O:ethanol adjusted to pH 1 using concentrated HCl. A variety of sizes can be synthesized by varying the time of heating which is further discussed in Chapter 3.

2.2.3 Characterization of TiO_2 Nanoparticles

The size distribution of the TiO_2 nanoparticles was determined using transmission electron microscopy (TEM). Samples of TiO_2 nanoparticles suspended in a 1:1 (v:v) water:ethanol solution were deposited onto a copper mesh grid coated with lacey carbon and a thin carbon coating and were then imaged using a Philips CM200 Ultra Twin TEM. Earlier samples used grids only with the lacey carbon (without the thin carbon coating) which resulted in less contrast between the TiO_2 nanoparticles and the carbon support. Samples were imaged using varying magnifications ranging from 190k to 630k and were collected using a Gatan CCD camera. Using ImageJ, the particles were manually counted and sized using a camera length calibration given by

$$\frac{pixels}{nm} = m_m \times mag(kx)$$

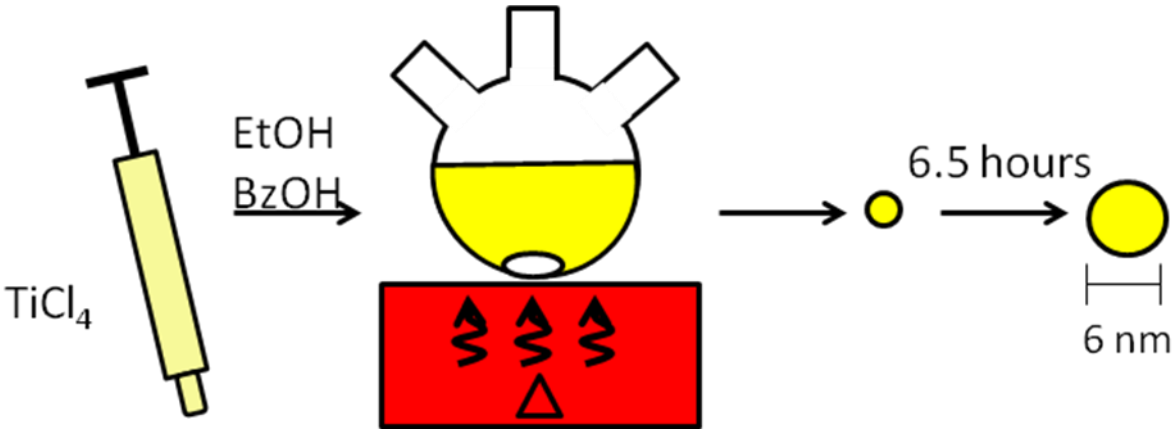

Figure 2.2: Synthesis scheme of the TiO_2 nanoparticles.

where m_m is the calibration factor for the CCD camera which was found to be 4.28 ± 0.06 x 10^{-2} and the magnification is given in kx. It is possible to see lattice fringes for the different TiO_2 faces if the particles are aligned on the grid with respect to the faces.

Larger nanoparticle samples were imaged using a Leo Supra55 VP scanningelectron microscope (SEM). Data shown were obtained using 2 kV incident electron energy obtained using the standard in-lens detector. The nanoparticle samples were spin-cast onto a boron doped (111) silicon wafer for imaging to prevent charging.

The phase of TiO_2 is determined using Raman spectroscopy since the two common phases of TiO_2, anatase and rutile, have characteristic Raman peaks. To prepare suitable Raman samples, the samples of TiO_2 in the water/ethanol solution are dripped onto a glass slide and dried in the oven at 80 °C. The spectra were taken with a DXR Raman Microscope from Thermo Scientific which uses visible wavelength lasers, a TE-cooled silicon CCD array detector, gratings, and Rayleigh filters. For the spectra, a 532 nm laser was used with 10.0 mW power. A full spectral range grating up to of 50 to 3500 cm^{-1} was used, which gives 5 cm^{-1} nominal resolution for the full width at half maximum (FWHM). Before each instrument use, the instrument was auto aligned and calibrated with a polystyrene alignment tool to correct any peak shifting. The spectra were taken with a 10x objective, with a collection time of 5 s, averaged over 10 exposures, fluorescence corrected with a 5^{th} order polynomial, and using a patented smart background within the OMNIC software that collects when the instrument is not in use and eliminates the need for the user to collect backgrounds.

2.2.4 Surface Functionalization of TiO_2 Nanoparticles

Prior to functionalization, the TiO_2 nanoparticles were precipitated from the acidic storage solution by the addition of 3:1 diethyl ether and methanol. The cloudy precipitate was then agitated to completely homogenize the contents followed by centrifugation (4000 g for 10 minutes) and decanting of the supernatant.

Sodium citrate is a tricarboxylate and was chosen to give better stability on the surface than a single carboxylate.(*33*) Citric acid has three pK_a values at 3.13, 4.76, and 6.40.(*33*) Since the solution needs to be below pH 6 to ensure a net positively charged surface, a final pH of 5 gives two mostly deprotonated acid groups and a positive surface. A functionalization solution was composed of 5 mM trisodium citrate in 20 mL of 18 MΩ-cm H_2O adjusted to a final pH of 8 using 0.5 M NaOH. Since the nanoparticles carried a positive surface from the H_2O/ethanol pH 1 storage solution, once the functionalization solution was added to the pellet of nanoparticles, the overall pH was 5. The pellet of nanoparticles was dispersed into the solution and then bath sonicated for 90 minutes. A successful functionalization produced a transparent solution.

For the catechol anchoring ligand functionalization, a solution of 7 mM 3,4-dihydroxybenzaldehye (DHBA) in 20 mL of 18 MΩ-cm H_2O adjusted to a pH of 10 using 0.5 M NaOH was heated at 80 °C to dissolve the molecule. Once cooled to room temperature, the solution was added to the pellet of TiO_2 nanoparticles crashed out of the storage solution. The final pH of the solution was 8, above the PZC of the TiO_2 and between the *pKa* values of the molecule (pKa_1 = 7.6 and pKa_2 is above 8). Once the

nanoparticles were agitated into solution, the solution immediately turned red and transparent.

Ascorbate functionalization is carried out similar to the catechol functionalization since they are both dienols. The *pKa* values for ascorbic acid are 4.10 and 11.79, giving a wide range of pH values for functionalization. The functionalization solution contained 6 mM sodium ascorbate in 20 mL of 18 MΩ-cm H_2O adjusted to a pH of 10 using 0.5 M NaOH. The solution was added to the pellet of TiO_2 nanoparticles centrifuged out of the acidic storage solution to give a final pH of the solution was 8. The particles were agitated into solution and immediately became a transparent orange colloidal solution.

After each functionalization, dialysis was conducted to remove excess ligand. Samples were dialyzed using a cellulose membrane (Sigma Aldrich #D9777, molecular weight cut-off 12,400 Da) in 18MΩ-cm H_2O for two 24-hour periods.

2.2.5 Characterization of Functionalized Nanoparticles

Fourier transform infrared spectroscopy measurements were performed using a Bruker Model Vertex70. Nanoparticle samples were prepared for FT-IR by placing a small amount of the functionalized nanoparticle suspension onto a ZnSe salt plate and heating to dryness at 80 °C. The FT-IR measurements were taken in transmission mode using an air background and averaged over 100 scans. For frequency comparisons, FT-IR spectra were taken of neat sodium citrate and citric acid. For these spectra, an ATR attachment was used with a diamond crystal.

X-Ray Photoelectron Spectroscopy (XPS) data were obtained using a modified Physical Electronics system equipped with an aluminum Kα source, a quartz-crystal X-

ray monochromator, and a 16-channel detector array. The samples prepared by placing a small amount of the functionalized nanoparticle solution onto a piece of boron doped (111) Silicon and heating to dryness at 80 °C. The survey was taken from 0-1400 eV, with 0.8 eV/step, a pass energy of 187.85, and averaged over 5 sweeps. For these samples, the multiplex scans were all taken with a pass energy of 23.50, with 0.05 eV/step, and averaged over 20 sweeps. All data was taken with an electron take-off angle was 45º and peak positions and areas were calculated by fitting raw data to Voigt functions after a Shirley background correction performed using the software package IGOR.

UV-Vis Spectroscopy was conducted on functionalized samples to determine the band gap of the samples and the success of dialysis. Samples were prepared by diluting by a factor of 200 in 18 MΩ-cm H_2O and using a quartz sub-micro cuvette with a path length of 1 cm. Spectra were taken with a Shimadzu UV-2401PC UV-Vis Recording Spectrophotometer.

Particle diffusivities were determined by dynamic light scattering using a Zetasizer Nano ZS (Malvern Instruments, Worcestershire, UK). Stock suspensions (500 μL) were transferred to low-volume, disposable cuvettes (Sarstedt, Part No. 67.758) and hydrodynamic diameters were determined using a ZetaSizer Nano ZS (Malvern Instruments, Worcestershire, UK; 633 nm laser, 173° scattering angle). Three measurements, each consisting of 10 runs, were obtained and averaged to yield mean hydrodynamic diameters ($d_{h,n}$). Particle diffusivities were converted to intensity-averaged hydrodynamic diameters using the Stokes-Einstein equation. Intensity

measurements were converted to number-averaged hydrodynamic diameters ($d_{h,n}$) using Mie theory. As this calculation involves numerous assumptions, confidence in the number-average is therefore less than for the intensity-average. Nonetheless, d_h number distributions can be used for comparative purposes between treatments.

2.2.6 Determination of Concentration

For the consequent reactive oxygen species and toxicity studies, it is necessary to know the concentration of TiO_2 in the aqueous samples. This was done using Inductively Coupled Plasma-Optical Emission Spectroscopy (ICP-OES). Two different types of digestion were done to determine the more complete: acid or base digestion.

For the base digestion, 10 μL of a nanoparticle solution was placed in a glass vial with 1 mL of a 5mM NaOH solution. The vials were loosely capped and placed in an oven at 60 °C for 24 hours to digest the nanoparticles into ions. The solutions are then brought to room temperature and were diluted to 10 mL in a volumetric flask using 18 MΩ-cm H_2O and were brought to an acidic pH using concentrated HCl. ICP standard solutions were prepared by diluting a 1000 mg/L Aldrich standard solution using 18 MΩ-cm H_2O.

For the aqua regia acid digestion, samples were first diluted by a factor of ten by taking 0.1 mL of each sample and adding 0.9 mL of 18 MΩ-cm H_2O. Then 10 μL of the diluted sample were added to a glass vial and 1 mL of concentrated HCl and 1 mL of concentrated HNO_3 were added to the vial. Without capping, the vials were heated to 120 °C for two hours to digest the nanoparticles into the corresponding ions. Once at room temperature, the digested samples were diluted to 10 mL in a volumetric flask using

10% HNO_3 in 18 MΩ-cm H_2O. ICP standard solutions were prepared by diluting a 1000 mg/L Aldrich standard solution using 1% HNO_3, concentrated HCl, and concentrated HNO_3 such that the standard solutions were identical in ionic strength to the experimental samples.

Ti concentrations were determined using a Varian Vista-MPX inductively coupled plasma-optical emission spectrometer (0.75 $L \cdot min^{-1}$ nebulizer flow; 15.0 $L \cdot min^{-1}$ plasma flow; Varian, Inc., California, USA). Emission was recorded at 334.188, 334.941, 336.122, and 337.280 nm and averaged.

The success of the aqua regia and base digestions were determined by gravimetric analysis. Two samples of TiO_2 that were also analyzed by digestion were crashed out of solution using a mixture of ether and methanol and centrifuging 4000 g for 10 min. The sample pellets were then dried overnight at 80 °C and then for two hours at 400 °C to remove any surface water. The mass of the samples were then determined and compared to the ICP-OES concentrations. For these ICP-OES samples we also wanted to determine the effect of dilution amounts. The original stock solutions were diluted by factors of 1000, 2000, and 4000.

2.3 Results and Discussion

2.3.1 Synthesis

Although there are a number of TiO_2 nanoparticle syntheses in the literature, the process used by Kotsokechagia et al. was ideal for the conditions we were interested in, giving us full control over the size, shape, and phase of the particles.(*6*) First of all, the synthesis provides completely anatase crystalline particles. It has been shown that rutile,

anatase, and rutile/anatase mixtures give different surface reactivities. In order to compare ROS generation and toxicity of different functionalized and sized surfaces, it is necessary to keep the phase constant. The Raman spectra of the synthesized nanoparticles (shown in Figure 2.3) show the characteristic peaks of anatase nanoparticles at 154, 406, 518, and 643 cm^{-1} and lack the characteristic peak of an anatase/rutile mixture at 290 cm^{-1}.(*4*, *43–45*)

The temperature and reaction time of the nanoparticle synthesis reaction are crucial to the resulting nanoparticles. First of all, it is important to maintain the temperature at 85 °C or lower. When the reaction reaches higher temperatures of over 100 °C, large structures of varying shape are formed shown in the SEM image in Figure 2.4. At temperatures lower than 85 °C, nanoparticles still form in the same fashion, however, kinetically take longer reaction times. The longer the nanoparticles are allowed to heat, the larger the nanoparticles become. As shown in Chapter 3, a variety of sizes can be synthesized with good monodispersity. However, the larger the particles are, the more polydisperse the solution becomes. Shown in Figure 2.4, extremely large particles samples are more polydisperse. An example of highly monodisperse samples of 6 ± 1 nm particles is shown in the TEM image in Figure 2.5 along with the statistical manual counting data in histogram form.

2.3.2 Surface Functionalization

FT-IR is a powerful tool for evaluating the nanoparticle-ligand system. Saturated carboxylic acids have a signature vibration peak at about 1740-1710 cm^{-1} which, in the case of the carboxylate salt species, becomes two peaks representing the asymmetric and

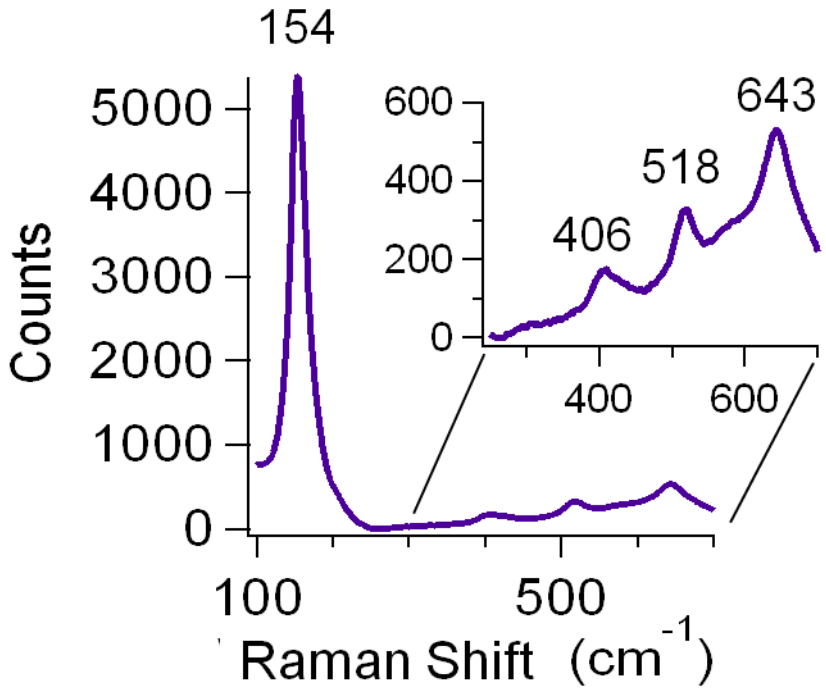

Figure 2.3: Raman spectrum of the synthesized TiO_2 nanoparticles. The peaks at 154, 406, 518, and 643 cm^{-1} all correspond to the anatase phase.

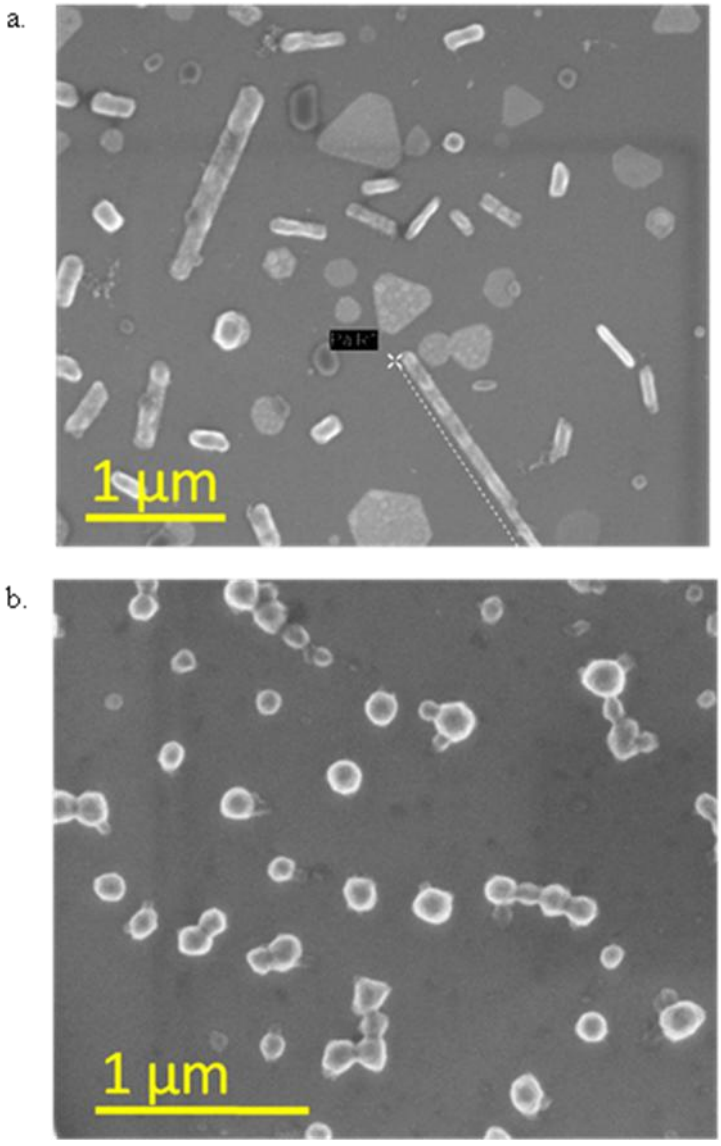

Figure 2.4: SEM images of the variations of time and temperature for the TiO_2 nanoparticle synthesis. a) portrays higher temperature of 110+ °C and b) portrays longer reaction time of 24 hours.

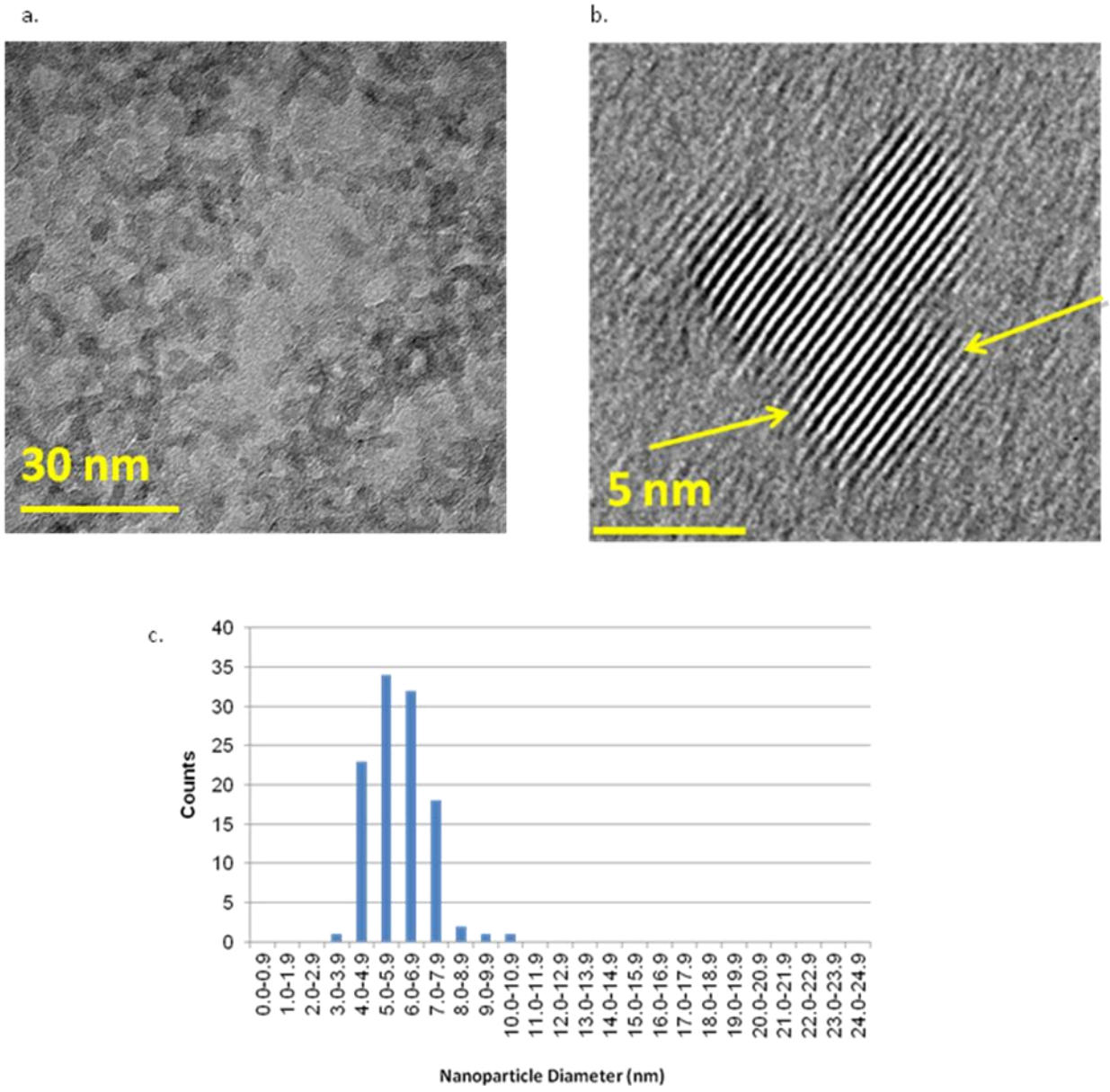

Figure 2.5: a) TEM micrograph of synthesized nanoparticles, b) TiO_2 nanoparticle with lattice fringes showing the (101) face, and c) the corresponding size analysis histogram. These represent a sample of 6 nm average particles.

symmetric stretches typically around 1695-1540 cm^{-1} and 1440-1335 cm^{-1} respectively.(*33*) The actual values of the asymmetric and symmetric vibration frequencies depend on the electron-withdrawing abilities of the attached group. Figure 2.6 shows the IR spectrum of citric acid, sodium citrate, and TiO_2 functionalized with the sodium citrate.

For the citric acid, the ν(C=O) is found at 1722 cm^{-1} which is consistent with the literature value for carboxylic acids. A ν(C-O) with OH deformation vibration is found at 1417 cm^{-1} and another ν(C-O) peak is found at 1205 cm^{-1}. Sodium citrate has an asymmetric peak at 1583 cm^{-1} and a symmetric peak at 1396 cm^{-1}. When absorbed to the surface of TiO_2, the asymmetric and symmetric peaks shift to 1622 and 1389 cm^{-1} respectively. This shift is caused by the carboxyl groups now bonded to Ti atoms at the surface instead of Na^+ ions. There is also a shoulder on the asymmetric peak showing up at 1716 cm^{-1}, similar to citric acid. Since it would be sterically difficult for all three carboxyl groups of citric acid to bind to the surface, it is possible that at least one carboxyl group is pointing toward the solution and is either protonated or still bound to a sodium ion.

Using XPS it is possible to obtain quantitative amounts of each element with respect to each other by comparing peak areas. Typically the Ti signal would be used as a reference point to determine surface area coverage; however, since the molecules used for functionalization contain only the elements carbon, oxygen, and hydrogen this is not possible. Hydrogen lacks valence electrons and therefore cannot be detected by the XPS, while carbon and oxygen are present in typical organic impurities found on the TiO_2

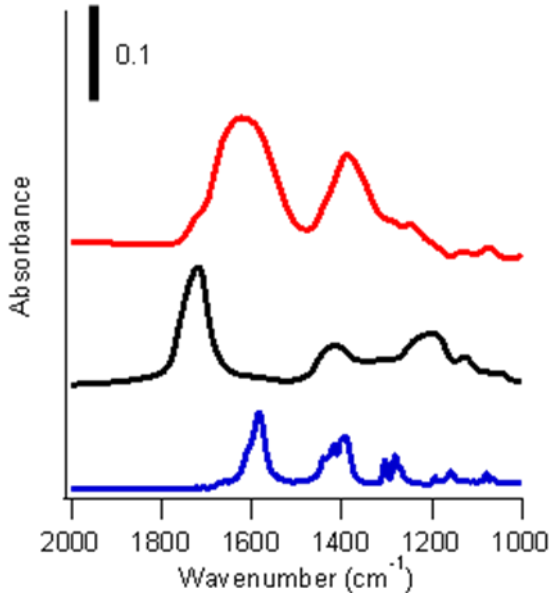

Citric Acid (cm^{-1})	Sodium Citrate (cm^{-1})	TiO_2+Citrate (cm^{-1})
ν(C=O) 1722	Asym. ν(C=O) 1583	Asym. ν(C=O) 1622
ν(C-O) 1417	Sym. ν(C=O) 1396	Sym. ν(C=O) 1389
ν(C-O) 1205	ν(C-O) 1282	ν(C-O) 1248

Figure 2.6: FTIR spectra of neat sodium citrate, neat citric acid, and citrate functionalized TiO_2 nanoparticles. The corresponding vibrational frequencies are displayed.

surface that it would be difficult to distinguish between functionalization molecules and the impurities. Figure 2.7 shows the XPS survey and multiplex spectra of C (1s), O (1s), and Ti (2p) for a citrate coated sample of TiO_2 nanoparticles.

The number averaged hydrodynamic diameter of the three different functionalizations is given in Figure 2.8. This data does not represent the principal particle sizes as found from TEM or SEM, but instead the size of the particle and ligands as they move in the aqueous solution known as the hydrodynamic diameter. This gives insight into the aggregation state of the particles as they are in the aqueous environment. From this data, the DHBA particles appear to be single nanoparticles in solution giving an average size of 5 nm. The citrate and ascorbate functionalized particles seem to form small aggregates with 17 and 23 nm diameters respectively. These are still considerably small aggregates since many commercially available nanoparticles give hydrodynamic diameters of 100-1000 nm.

2.3.3 Influence of Dialysis

For the functionalization step, an excess of ligand molecules is used to ensure the surface is fully coated. Dialysis was performed on the samples to remove any excess ligands in solution that are not associated with the TiO_2 nanoparticle surface. This is important to achieve reproducible samples where all the molecules are on the surface and not in solution. Also, as shown in Chapter 3, the amount of organic material in solution can influence the production of ROS which could cause inconsistent results which would not reflect only the influence of the ligand on the surface.

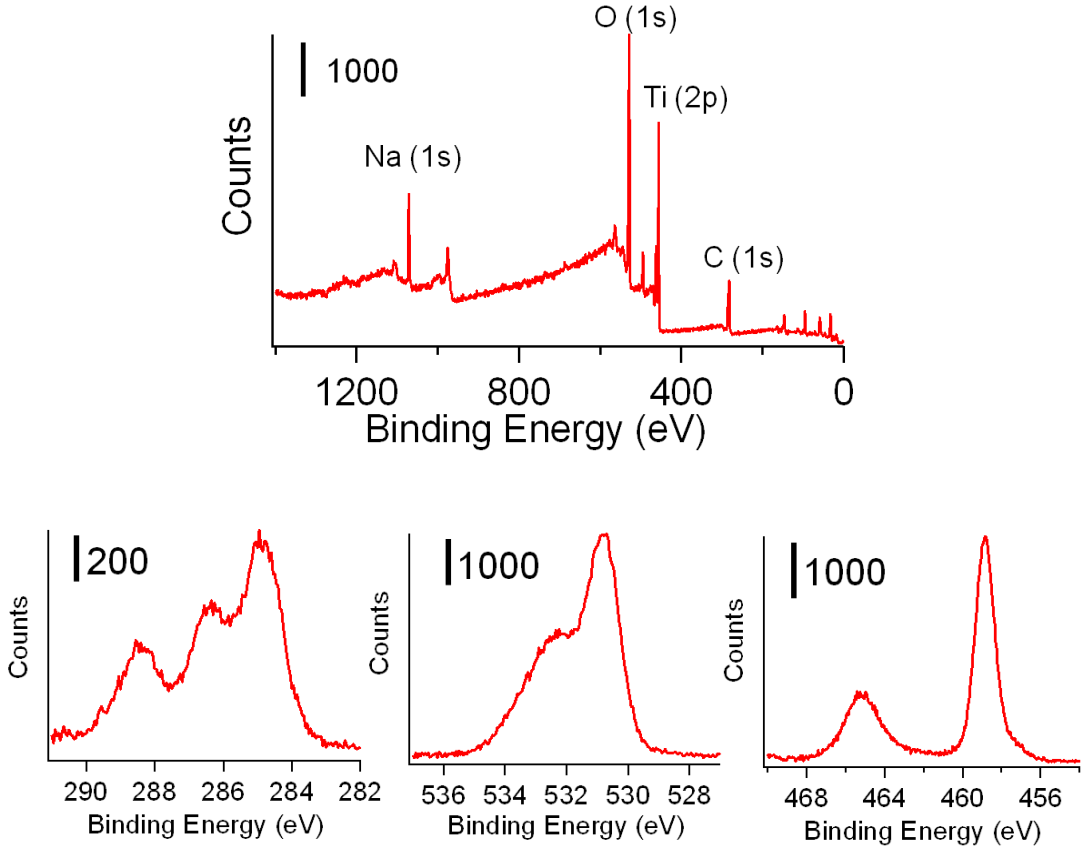

Figure 2.7: XPS survey and multiplex spectra of the carbon, oxygen, and titanium species for citrate coated nanoparticles.

Ligand	Citrate	Ascorbate	DHBA
DLS Run 1	16.79	16.45	3.64
DLS Run 2	16.61	23.35	5.01
DLS Run 3	17.06	9.397	6.473
DLS Run 4		42.88	
Mean	**16.82**	**23.02**	**5.04**
Std Dev	**0.23**	**14.41**	**1.42**

Figure 2.8: Hydrodynamic diameter (nm) values for citrate, ascorbate, and DHBA functionalized nanoparticles.

After the two 24 hour dialysis cycles, visually the colored nanoparticle solutions are different. Shown in Figure 2.9, is a functionalization of TiO_2 nanoparticles with DHBA where the sample on the left has been dialyzed twice and the sample on the right has not been dialyzed. The corresponding UV-Vis measurements show the removal of DHBA with considerably lower absorbance in the visible region. The FTIR spectrum also shows a reduction in overall absorbance. However, there is still DHBA on the surface of TiO_2 since there is still the presence of visible absorbance in the UV-Vis which corresponds to the ligand to metal charge transfer transition within the surface complexes and strong vibrations of the aldehyde and aromatic groups in the FTIR.

2.3.4 TiO_2 Concentrations

TiO_2 nanoparticle digestion into the corresponding ions was done with both NaOH and aqua regia solutions. To ensure the efficiency of the digestions, the concentration of two samples was also evaluated using gravimetric analysis. The Ti concentration detected by ICP-OES was converted to a concentration of TiO_2 in mg/L. The ratio of TiO_2 concentration from ICP analysis to the amount of TiO_2 detected by gravimetric analysis is shown in Figure 2.10 for both the acid and base digestions. For one sample, the full concentration of TiO_2 for both digestions produced large precipitates and could not be used for analysis since they would clog the ICP-OES nebulizer. The NaOH base digestions show a common trend of 60-80% of the TiO_2 mass detected by ICP. There is no dependence of the amount recovered on the concentration that was digested. However, the acid digestion shows a strong dependence on the concentration digested. Samples at higher concentration digested only 70% of the massed samples,

a.

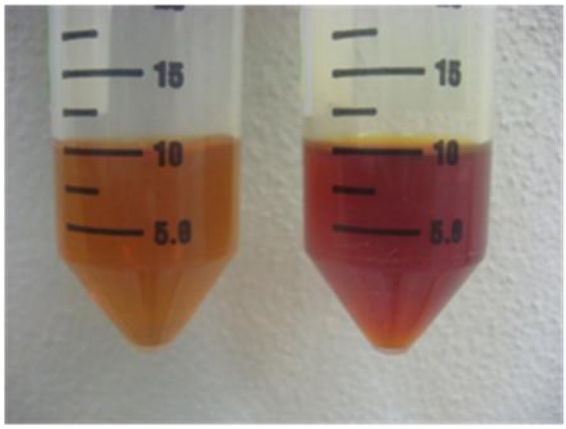
15
10
5.0
15
10
5.0

b.

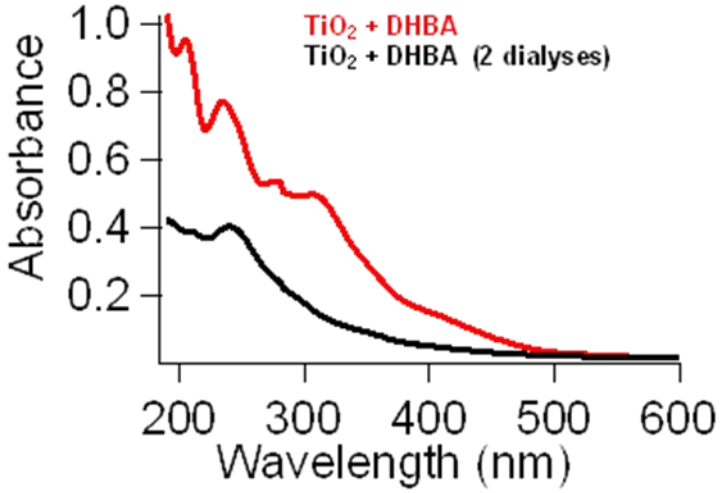
TiO2 + DHBA
TiO2 + DHBA (2 dialyses)
Absorbance
1.0
0.8
0.6
0.4
0.2
200
300
400
500
600
Wavelength (nm)

c.

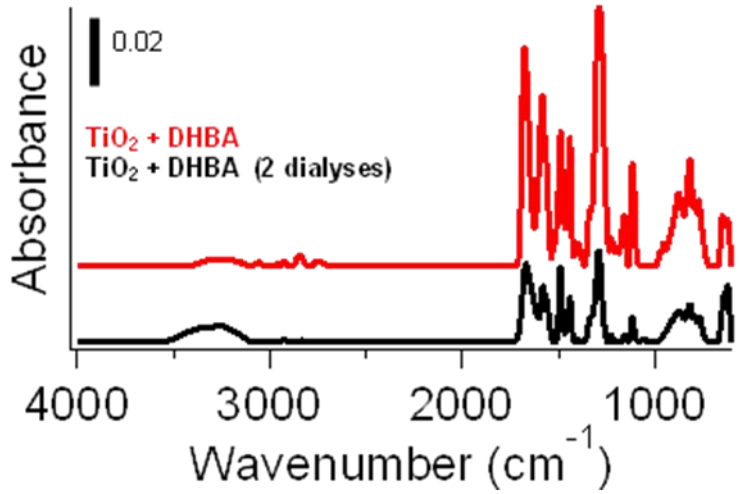
0.02
TiO2 + DHBA
TiO2 + DHBA (2 dialyses)
Absorbance
4000
3000
2000
1000
Wavenumber (cm-1)

Figure 2.9: Picture in a) displays the same sample of DHBA coated particles, the centrifuge tube on the left is after two dialyses and the tube on the right is before dialysis, b) is the UV-Vis spectrum of the DHBA coated particles before and after dialysis, and c) is the corresponding FTIR spectra.

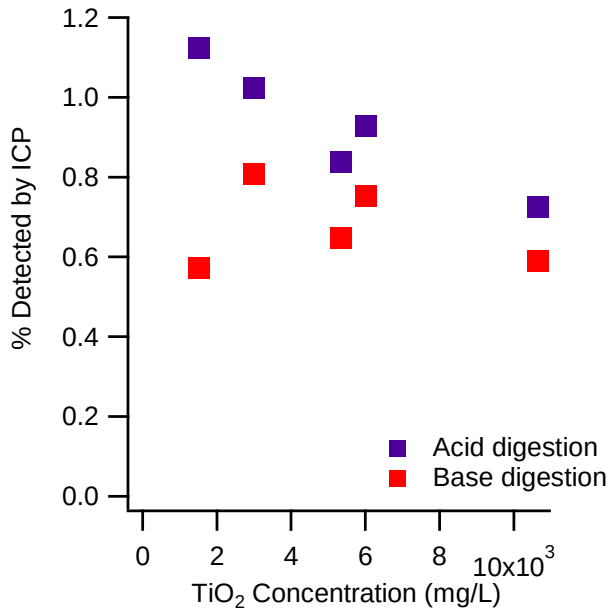

Figure 2.10: Percent of TiO_2 detected by the ICP-OES using both an acid digestion and a base digestion compared to the gravimetric analysis.

whereas at the lowest concentration were able to digest 100%. There were samples that gave higher than 100% digested, however, this can be attributed to balance errors for such small masses. From this data, the acid digestion is found to be superior to the base digestion, especially at lower concentrations. Therefore, it is best to first dilute the samples by a factor of 10 before doing the second dilution by a factor of 1000 to ensure full digestion.

2.5 Conclusions

TiO_2 nanoparticles are successfully synthesized in a controlled and reproducible manner using an organic solution based synthesis. The resulting nanoparticles are characterized by TEM, SEM, and Raman spectroscopy. The nanoparticles are then functionalized with citrate, 3,4-dihydroxybenzaldehyde, and ascorbate. The importance of the removal of excess ligands through dialysis is highlighted along with a successful aqua regia nanoparticle digestion for ICP-OES concentration quantification.

2.6 References

(1) Birdi, K. S. *Handbook of Surface and Colloid Chemistry*; 3rd ed.; CRC Press: Boca Raton, FL, 2009.

(2) Taylor, S.; Qu, L.; Kitaygorodskiy, A.; Teske, J.; Latour, R. a; Sun, Y.-P. Synthesis and characterization of peptide-functionalized polymeric nanoparticles. *Biomacromolecules* **2004**, *5*, 245-8.

(3) Yan, X.; Pan, D.; Li, Z.; Liu, Y.; Zhang, J.; Xu, G.; Wu, M. Controllable synthesis and photocatalytic activities of water-soluble TiO_2 nanoparticles. *Materials Letters* **2010**, *64*, 1833-1835.

(4) Nolan, N. T.; Seery, M. K.; Pillai, S. C. Spectroscopic investigation of the anatase-to-rutile transformation of sol-gel-synthesized TiO_2 photocatalysts. *Journal of Physical Chemistry C* **2009**, *113*, 16151-16157.

(5) Madhusudan Reddy, K. Preparation, characterization, and spectral studies on nanocrystalline anatase TiO_2. *Journal of Solid State Chemistry* **2001**, *158*, 180-186.

(6) Kotsokechagia, T.; Cellesi, F.; Thomas, A.; Niederberger, M.; Tirelli, N. Preparation of ligand-free TiO2 (anatase) nanoparticles through a nonaqueous process and their surface functionalization. *Langmuir* **2008**, *24*, 6988-97.

(7) Dai, Y.; Cobley, C. M.; Zeng, J.; Sun, Y.; Xia, Y. Synthesis of anatase TiO_2 nanocrystals with exposed {001} facets. *Nano Letters* **2009**, *9*, 2455-9.

(8) Yu, M.-Z.; Lin, J.-Z.; Chan, T.-L. Effect of precursor loading on non-spherical nanoparticle synthesis in a diffusion flame reactor. *Chemical Engineering Science* **2008**, *63*, 2317-2329.

(9) Liqiang, J.; Xiaojun, S.; Weimin, C.; Zili, X.; Yaoguo, D. The preparation and characterization of nanoparticle TiO_2 / Ti films and their photocatalytic activity. *Journal of Physics and Chemistry of Solids* **2003**, *64*, 615-623.

(10) Ehrman, S. H.; Friedlander, R. S. K.; Zachariahs, M. R. Characteristics of SiO_2/TiO_2 nanocomposite particles formed in a premixed flat flame. *Journal of Aerosol Science* **1998**, *29*, 687-706.

(11) Joo, J.; Yu, T.; Kim, Y. W.; Park, H. M.; Wu, F.; Zhang, J. Z.; Hyeon, T. Multigram scale synthesis and characterization of monodisperse tetragonal zirconia nanocrystals. *Journal of the American Chemical Society* **2003**, *125*, 6553-7.

(12) Hu, M. Z.-C.; Harris, M. T.; Byers, C. H. Nucleation and growth for synthesis of nanometric zirconia particles by forced hydrolysis. *Journal of Colloid and Interface Science* **1998**, *198*, 87-99.

(13) Fan, J.; Boettcher, S. W.; Stucky, G. D. Nanoparticle assembly of ordered multicomponent mesostructured metal oxides via a versatile sol−gel process. *Chemistry of Materials* **2006**, *18*, 6391-6396.

(14) Briesen, H.; Fuhrmann, A.; Pratsinis, S. E. The effect of precursor in flame synthesis of SiO_2. *Chemical Engineering Science* **1998**, *53*, 4105-4112.

(15) Okuyama, K.; Wuled Lenggoro, I. Preparation of nanoparticles via spray route. *Chemical Engineering Science* **2003**, *58*, 537-547.

(16) Niederberger, M.; Garnweitner, G. Organic reaction pathways in the nonaqueous synthesis of metal oxide nanoparticles. *Chemistry* **2006**, *12*, 7282-302.

(17) Trewyn, B. G.; Slowing, I. I.; Giri, S.; Chen, H.-T.; Lin, V. S.-Y. Synthesis and functionalization of a mesoporous silica nanoparticle based on the sol-gel process and applications in controlled release. *Accounts of Chemical Research* **2007**, *40*, 846-53.

(18) Park, H. K.; Park, K. Y. Vapor-phase synthesis of uniform silica spheres through two-stage hydrolysis of $SiCl_4$. *Materials Research Bulletin* **2008**, *43*, 2833-2839.

(19) Chen, X.; Mao, S. S. Titanium dioxide nanomaterials: synthesis, properties, modifications, and applications. *Chemical Reviews* **2007**, *107*, 2891-959.

(20) Liu, X.; Chen, G.; Su, C. Effects of material properties on sedimentation and aggregation of titanium dioxide nanoparticles of anatase and rutile in the aqueous phase. *Journal of Colloid and Interface Science* **2011**, *363*, 84-91.

(21) Grassian, V. H. When size really matters: Size-dependent properties and surface chemistry of metal and metal oxide nanoparticles in gas and liquid phase environments. *Journal of Physical Chemistry C* **2008**, *112*, 18303-18313.

(22) Li, B.; Franking, R.; Landis, E. C.; Kim, H.; Hamers, R. J. Photochemical grafting and patterning of biomolecular layers onto TiO_2 thin films. *ACS Applied Materials & Interfaces* **2009**, *1*, 1013-22.

(23) Franking, R. a; Landis, E. C.; Hamers, R. J. Highly stable molecular layers on nanocrystalline anatase TiO_2 through photochemical grafting. *Langmuir* **2009**, *25*, 10676-84.

(24) Franking, R.; Hamers, R. J. Ultraviolet-induced grafting of alkenes to TiO_2 surfaces: Controlling multilayer formation. *Journal of Physical Chemistry C* **2011**, *115*, 17102-17110.

(25) Chen, J.; Franking, R.; Ruther, R. E.; Tan, Y.; He, X.; Hogendoorn, S. R.; Hamers, R. J. Formation of molecular monolayers on TiO_2 surfaces: a surface analogue of the Williamson ether synthesis. *Langmuir* **2011**, *27*, 6879-89.

(26) Araujo, P. Z.; Morando, P. J.; Blesa, M. a Interaction of catechol and gallic acid with titanium dioxide in aqueous suspensions. 1. Equilibrium studies. *Langmuir* **2005**, *21*, 3470-4.

(27) Creutz, C.; Chou, M. H. Binding of catechols to mononuclear titanium(IV) and to 1- and 5-nm TiO_2 nanoparticles. *Inorganic Chemistry* **2008**, *47*, 3509-14.

(28) Dobson, K. D.; Mcquillan, A. J. In situ infrared spectroscopic analysis of the adsorption of aromatic carboxylic acids to TiO_2, ZrO_2, Al_2O_3, and Ta_2O_5 from aqueous solutions. *Spectrochimica Acta Part A* **2000**, *56*, 557 - 565.

(29) Hug, S.; Bahnemann, D. Infrared spectra of oxalate, malonate and succinate adsorbed on the aqueous surface of rutile, anatase and lepidocrocite measured with in situ ATR-FTIR. *Journal of Electron Spectroscopy and Related Phenomena* **2006**, *150*, 208-219.

(30) Li, S.-C.; Wang, J.-guo; Jacobson, P.; Gong, X.-Q.; Selloni, A.; Diebold, U. Correlation between bonding geometry and band gap states at organic-inorganic interfaces: catechol on rutile TiO_2(110). *Journal of the American Chemical Society* **2009**, *131*, 980-4.

(31) Martin, S. T.; Kesselman, J. M.; Park, D. S.; Lewis, N. S.; Hoffmann, M. R. Surface structures of 4-chlorocatechol adsorbed on titanium dioxide. *Environmental Science & Technology* **1996**, *30*, 2535-2542.

(32) Mendive, C. B.; Bredow, T.; Feldhoff, A.; Blesa, M. a; Bahnemann, D. Adsorption of oxalate on anatase (100) and rutile (110) surfaces in aqueous systems: Experimental results vs. theoretical predictions. *Physical Chemistry Chemical Physics* **2009**, *11*, 1794-808.

(33) Mudunkotuwa, I. a; Grassian, V. H. Citric acid adsorption on TiO_2 nanoparticles in aqueous suspensions at acidic and circumneutral pH: surface coverage, surface speciation, and its impact on nanoparticle-nanoparticle interactions. *Journal of the American Chemical Society* **2010**, *132*, 14986-94.

(34) Pettibone, J. M.; Cwiertny, D. M.; Scherer, M.; Grassian, V. H. Adsorption of organic acids on TiO_2 nanoparticles: effects of pH, nanoparticle size, and nanoparticle aggregation. *Langmuir* **2008**, *24*, 6659-67.

(35) Rajh, T.; Chen, L. X.; Lukas, K.; Liu, T.; Thurnauer, M. C.; Tiede, D. M. Surface restructuring of nanoparticles: An efficient route for ligand−metal oxide crosstalk. *The Journal of Physical Chemistry B* **2002**, *106*, 10543-10552.

(36) Rodríguez, R.; Blesa, M.; Regazzoni, A. Surface complexation at the TiO(2) (anatase)/aqueous solution interface: Chemisorption of catechol. *Journal of Colloid and Interface Science* **1996**, *177*, 122-131.

(37) Schmuck, C.; Schwegmann, M. A molecular flytrap for the selective binding of citrate and other tricarboxylates in water. *Journal of the American Chemical Society* **2005**, *127*, 3373-9.

(38) Stone, A. T. Adsorption of catechols , metal (hydr) oxide / water interface: Effect of ring substituents on the adsorption onto TiO_2. *Environmental Science & Technology* **1996**, *30*, 1604-1613.

(39) Xu, Y.; Chen, W.-K.; Liu, S.-H.; Cao, M.-J.; Li, J.-Q. Interaction of photoactive catechol with TiO_2 anatase (101) surface: A Periodic density functional theory study. *Chemical Physics* **2007**, *331*, 275-282.

(40) Ojea-Jiménez, I.; Puntes, V. Instability of cationic gold nanoparticle bioconjugates: the role of citrate ions. *Journal of the American Chemical Society* **2009**, *131*, 13320-7.

(41) Vayssieres, L. On the effect of nanoparticle size on water-oxide interfacial chemistry. *Journal of Physical Chemistry C* **2009**, *113*, 4733-4736.

(42) Buff, H., Graf, K., Kappl, M. *Physics and Chemistry of Interfaces*; 2nd ed.; Wiley-VCH, 2006.

(43) Wachs, I. E. Raman and IR studies of surface metal oxide species on oxide supports: Supported metal oxide catalysts. *Catalysis Today* **1996**, *27*, 437-455.

(44) Zhang, W. F.; He, Y. L.; Zhang, M. S.; Yin, Z.; Chen, Q. Raman scattering study on anatase TiO_2 nanocrystals. *Journal of Physics D: Applied Physics* **2000**, *33*, 912-916.

(45) Balachandran, U.; Eror, N. G.; Mammone, R. Raman spectra of titanium dioxide. *Journal of Solid State Chemistry* **1982**, *42*, 276-282.

Chapter 3

Reactive Oxygen Species Generation on TiO_2: Influence of Nanoparticle Size, Surface Ligands, and Excess Ligands

3.1 Introduction

Titanium dioxide (TiO_2) nanoparticles are becoming more prevalent in society in a variety of applications including electronics, food packaging, paint, cosmetics, sunscreens, ceramics, plastics, and waste water treatment.(*1–9*) By 2015, Nel et al predict the sale of products using nanotechnology may reach $1 trillion.(*6*) The chemical and physical properties of nanoparticles are determined primarily by their size, shape, composition, reactivity, and surface chemistry.(*10, 11*)

Although TiO_2 nanoparticles are becoming more prevalent in society, little is still known about the health and safety of these materials. As a photocatalyst, TiO_2 produces reactive oxygen species (ROS) when exposed to light above its band-gap where the electron can reduce molecular oxygen into superoxide anion ($O2^{\cdot-}$) and the hole can oxidize water into hydroxyl radicals ($OH^{\cdot}$). Reactive oxygen species are known to cause oxidative stress and therefore toxicity in organisms. The oxidative stress and ultimate toxicity of various TiO_2 nanoparticles have been studied in zebrafish and other organisms.(*3, 6, 7, 9, 12–20*)

Due to the increased surface-area-to-volume ratio, there are more reactive surface sites on nanoparticles than for the same mass of bulk materials, increasing the chances for the production of ROS.(*6, 11*) Particles on the order of 5 nm in diameter have about 50% of their atoms at the surface, highlighting the need to understand the surface properties

and surface chemistry of nanoparticles.(*6, 11*) The size of the nanoparticle can have a direct effect on both their microscopic and macroscopic behaviors such as electronic band gaps, magnetic moments, specific heats, melting points, particle morphologies, and surface reactivities.(*10*, *11*)

Previous studies that have examined the surface functionalization, generation of reactive oxygen species, and/or toxicity of TiO_2 nanoparticles have focused on commercial products since those are the materials currently being released to the environment.(*1, 2, 4, 5, 7, 9, 12–15, 17, 19–26*) Unfortunately, these studies are limited to what is commercially available, which generally leads to results based on a very limited size range or a comparison of particles with a variety of sizes, shapes, and crystal phases. These nanoparticles can also vary slightly from batch to batch, making results less consistent. Some TiO_2 ROS and degradation studies have looked at the cosmetic products themselves since most everyday applications of nanomaterials use nanoparticles that are surface modified and embedded in the final product that also contains a number of chemicals.(*1*)

The purpose of this research is to determine, at a molecular scale, the components of the nanoparticle ligand system which impact the generation of reactive oxygen species. For that reason it is important to synthesize the nanoparticles directly in the laboratory where they will be characterized and used for ROS and toxicity studies to ensure highly controlled and reproducible samples. The parameters that are evaluated to determine their effect on ROS generation for this study are the presence of a buffer, presence of excess ligand, nanoparticle size, light exposure time, and ligand degradation.

The presence of a buffer and excess ligand are examples of how the surrounding environment of the nanoparticles can influence the system. These parameters could have the potential to increase or decrease the generation of ROS production. A phosphate buffer is expected to bind to the surface in equilibrium with the surface citrate ligand and thus the amount of ROS generated will be a combination of ROS expected from citrate coated particles and ROS expected from phosphate coated particles. Whereas presence of excess ligand would be expected to decrease the ROS generation since as the ligand on the surface is degraded, citrate from solution would be able to bind to the surface and continue stabilization.

The size of the nanoparticles is expected to influence ROS production. The electronic properties of a material are strongly correlated with the size of the material and thus the surface reactivity is dependent on size. For the TiO_2 nanoparticles to produce ROS an electron-hole pair has to be created by light excitation, the electron and hole need to separate from each other, and the electron and hole need to independently travel to the surface.(*27*) It is hypothesized that the largest amount of ROS would be generated by particles of an intermediate size. Since larger particles have an increased volume, the electron and hole would be less likely to travel to the surface to react with water and oxygen before recombining. As the particles approach quantum confinement, the electron and hole would not be able to separate due to the infinitely small volume at the quantum confinement of the material (< 1.5 nm diameter) and would therefore recombine at the surface before generating ROS.(*28*, *29*) These competing processes suggest an intermediate size that would optimize the oxidation and reduction processes.

A variety of ways have been developed to describe and determine the size of a nanoparticle.(*11*) First of all is the principal particle size, or diameter of a single particle without influence of the surface species. This is determined using techniques such as Transmission Electron Microscopy (TEM) or X-Ray Diffraction (XRD). Size can also be described by the hydrodynamic diameter of the particles. This method determines the size of the particles by Brownian motion within a solution, therefore giving the size of the aggregates as well as influences from surface ligands. The hydrodynamic diameter is calculated from the translational diffusion coefficient by using the Stokes-Einstein Equation(*11*)

$$d(H) = \frac{kT}{3\pi\eta D}$$

where d(H) is the hydrodynamic diameter, k is Boltzmann's constant, T is the absolute temperature, η is the solvent viscosity, and D is the translational diffusion coefficient. The hydrodynamic diameter is determined using a Dynamic Light Scattering (DLS) instrument.

For this study, the size of the nanoparticles will be displayed in terms of the principal particle size, however, it important to evaluate the aggregation of the particles since this may reduce the number of available surface active sites.

While ROS is generated, previous research has shown that carboxylate ligands can be oxidized on the surface.(*22*, *24*, *28*, *30–32*) Over time, this can have an effect on

the continuous exposure of the nanoparticles where the initial particles no longer have the same surface coating as the particles illuminated for 24 hours. It is hypothesized that on short scale time periods the generation of reactive oxygen species will reach a steady state, however, once the surface ligands have been degraded the generation will increase due to a lack of organic material to oxidize.

Another key aspect of solution-based nanoparticle experiments is the proper metric to utilize when comparing different samples. Examples of such metrics include mass density (mg/cm^3), number density ($particles/cm^3$), and total surface area (nm^2). The metrics used will depend greatly on the application. For this study, the samples are compared in terms of similar mass density and similar surface area.(*6*)

3.2 Experimental Methods

3.2.1 Chemicals

$TiCl_4$ purchased from Sigma-Aldrich (208556) is ReagentPlus® 99.9% trace metals basis. Anhydrous benzyl alcohol purchased from Sigma-Aldrich (305197) is 99.8% pure. Ethanol 200 proof was purchased from Decon Laboratories Inc. (2716). All samples were functionalized with sodium citrate (51804, Sigma). All water used is brought to 18.0-18.2 ΩM-cm resistivity using a Barnstead NANOpure Infinity ultrapure water system with an organic free filter cartridge. A 0.5 M NaOH solution was made using sodium hydroxide (NaOH) (S318, Fisher Scientific) in 18 MΩ-cm H_2O. HCl (Sigma Aldrich) was used in full concentration of 37%. Degussa (Evonik) P25 (Aeroxide

TiO_2 P 25) and Sun Nano from Sun Innovations Inc. (SN3301) are commercially available TiO_2 nanoparticles.

For reactive oxygen species measurements and quantitative analysis, used the fluorescent probe 3'-(p-aminophenyl) fluorescein (APF) 5mM solution in DMF (A36003, Invitrogen Life Technologies Corporation), phosphate buffer pH 7.2 (319252, Fluka), peroxidase type II from horseradish (P8250, Sigma), hydrogen peroxide 30% solution in H_2O (HX0635, EMD), and spin trap molecule 2,2,6,6-Tetramethylpiperidin-1-yl)oxyl or TEMPO (426369, Aldrich)

3.2.2 Synthesis and Functionalization

TiO_2 nanoparticles were synthesized following the method of Kotsokechagia, et al.(*33*) In a 250 mL round-bottom flask, 5 mL of $TiCl_4$ was added to 25 mL anhydrous ethanol while stirring. After 2 minutes, 100 mL of anhydrous benzyl alcohol was added. The resulting yellow solution was stirred at 85^oC. For the 6.1, 10.1, 13.8, and 15.0 nm samples used in this study, the solutions were heated for 7, 11, 13 and 14 hours respectively. After cooling to room temperature, dimethyl ether was added to the nanoparticle suspension to achieve a 2:1 (v:v) ratio of ether to nanoparticle suspension . The addition of ether caused the nanoparticles to concentrate to the bottom of the vessel. The nanoparticle mixture was then centrifuged at 4000 g for 10 minutes. The supernatant liquid was removed and the remaining nanoparticles were suspended via sonication in a 1:1 (v:v) mixture of deionized water:ethanol, adjusted to pH=1 using HCl.

The size distribution of the TiO_2 nanoparticles was determined using transmission electron microscopy (TEM). Samples of TiO_2 nanoparticles functionalized with sodium

citrate suspended in a 1:1 (v:v) water:ethanol solution were deposited onto a copper mesh grid coated with lacey carbon and were then imaged using a Philips CM200 Ultra Twin TEM. Sample averages were 6.1 ± 1.1, 10.1 ± 1.7, 13.8 ± 2.3, and 15.0 ± 2.2 nm.

The TiO_2 nanoparticles were precipitated from the acidic storage solution by the addition of 3:1 diethyl ether and MeOH. The cloudy precipitate was then agitated to completely homogenize the contents, followed by centrifugation (4000 g for 10 minutes), and then the supernatant was decanted. Sodium citrate (5 mM in 18 MΩ-cm H_2O adjusted to a final pH of 5 using 0.5 M NaOH) was added to the nanoparticle precipitate and the resulting mixture was agitated to free the precipitate from the bottom of the centrifuge tube. The suspension was sonicated for 1.5 hours to yield a translucent suspension, which was then dialyzed using a cellulose membrane (Sigma Aldrich #D9777, molecular weight cut-off 12,400 Da) in 18 MΩ-cm H_2O for two 24 hour periods.

3.2.3 Light Exposure

Sunlight was simulated using a 250 W blue-spectrum metal halide lamp (XM 250W, 10,000K; electronic ballast; XM Lighting, Anaheim, CA) designed to mimic sunlight at shallow depths in the ocean. Studies were carried out in 96-well plates using a quartz plate as the cover. Dark samples were placed under the light completely covered in aluminum foil to allow for the same temperature fluctuations but prevent the exposure to light. Sample volumes were all 300 μL to keep the solution height constant between samples. The sample plates were placed 18 inches under the light for exposure.

3.2.4 Hydroxyl Radical Detection

Hydroxyl radicals (OH·) were measured quantitatively using a fluorescent probe, 3'-(p-aminophenyl) fluorescein (APF) purchased from Life Technologies Corporation. After samples were exposed to light or dark conditions, 10 μM APF and 100 mM phosphate buffer (pH 7.2) were added to each sample. The samples were then transferred to amber vials to prevent additional light exposure. Steady-state fluorescence measurements were taken using an ISS K2 Time-Resolved Spectrofluorometer using slit sizes of 2.0 mm and 0.5 mm for the excitation and emission respectively. The samples were excited at 490 nm and emission peak occurred between 510 and 525 nm. To prevent over-saturation of the photon-counting detector, each of the samples were diluted by a factor of 10. A linear quantitative curve was used to determine concentrations of OH· present in each sample.

To create the linear quantitative curve, 5 mL solutions of 0 to 1000 nM H_2O_2 concentrations in 100 nM increments were made using 18 MΩ-cm H_2O that was purged with Ar gas and left out of the light for at least one month. Added to each solution was 50 mM of pH 7.2 phosphate buffer, 2.95 units/mL of horseradish peroxidase, and 10 μM of APF. To correlate to similar quantities of APF as in the TiO_2 samples, each of the standards was diluted by a factor of 10. Fluorescence measurements were taken using the same conditions as the TiO_2 samples. The peak intensities were used to create a standard quantitative curve.

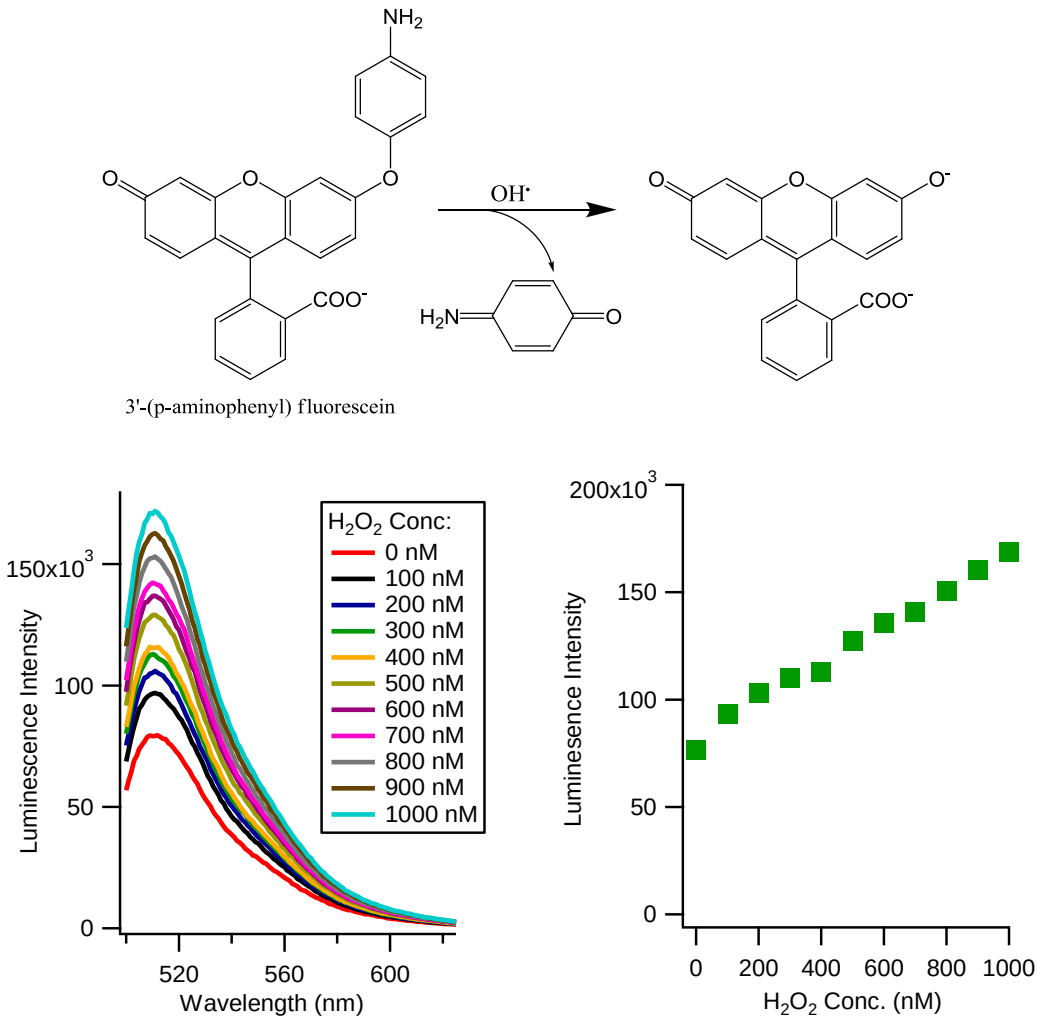

Figure 3.1: Structure of 3'-(p-aminophenyl) fluorescein (APF) along with the standard curve for H_2O_2 detection and corresponding fluorescent spectra.

3.2.5 ROS Generation by Degussa P25 and Sun Nano

The generation of ROS by Degussa P25 and Sun Nano were also determined to compare to the synthesized particles. These products are received in powdered form and have "bare" surfaces where the surface is not specifically modified with an organic ligand. Stock solutions of 2000 mg/L TiO_2 were made of both Degussa P25 and Sun Nano using 18 MΩ-cm H_2O. The stock solutions were bath sonicated for 30 minutes prior to any usage. For the light exposure experiments, the stock solutions were diluted to 10, 100, and 1000 mg/L TiO_2 using 18 MΩ-cm H_2O that was purged with Ar gas and left out of the light for at least one month. The samples were exposed to the metal halide lamp for 24 hours. The APF fluorescent indicator and buffer were added to the light exposed samples just before removing from the light and to the dark samples while still in the dark.

3.2.6 Influence of Buffer on ROS Generation

For this study 10.1 nm nanoparticles were used as the samples. The samples were diluted to 1000 mg/L TiO_2 in 18 MΩ-cm H_2O that was purged with Ar gas and left out of the light for at least one month and were exposed to the metal halide lamp for 24 hours. One set of samples followed the normal procedure (as described in Section 3.2.4) of adding 10 μM APF and 100 mM phosphate buffer pH 7.2 immediately before removing the samples from under the light. The other set of samples added the 100 mM phosphate buffer at the beginning of the light exposure and the 10 μM APF immediate before removing the samples from under the light. Each was carried out in quadruplicate.

3.2.7 ROS Generation in the Presence of Excess Ligand in Solution

For this study used 10.1 nm nanoparticles were used as the samples. The samples were diluted to 1000 mg/L TiO_2 in 18 MΩ-cm H_2O that was purged with Ar gas and left out of the light for at least one month and were exposed to the metal halide lamp for 24 hours. Excess citrate was added prior to light exposure with one sample each of 0, 4, 10, 20, 40, 60, 80 and 100 mM of excess citrate. After 24 hours of light exposure using the metal halide lamp, 10 μM APF and 100 mM phosphate buffer (pH 7.2) were added immediately before removing the samples from under the light.

3.2.8 ROS Generation based on Nanoparticle Size

For the 6.1, 10.1, 13.8, and 15.0 nm nanoparticle samples, light reactions were carried out in the same 96-well plate to ensure similar reaction conditions. Samples were diluted to 250 and 500 mg/L TiO_2 using 18 MΩ-cm H_2O that was purged with Ar gas and left out of the light for at least one month. Each sample was carried out in quadruplicate for both light and dark samples. Samples were exposed to the metal halide lamp for 24 hours. The APF fluorescent indicator and buffer were added to the "light exposed" samples just before removing from the light and to the "dark" samples while in the dark.

3.2.9 Time-Dependent ROS Generation and Ligand Degradation

To get an extended time-dependence of the ROS generation, samples diluted to 1000 mg/L TiO_2 for the 10.1 nm nanoparticles were illuminated for 3, 4.5, 26 and 50 hours by the metal halide lamp. The APF fluorescent indicator and buffer were added to the samples for ROS detection just before removing from the light and were not added to

the samples destined for FTIR spectroscopy. All samples were then transferred to amber vials to prevent further light exposure. Another set of experiment examined a larger number of time points for ROS generation starting with sub-hour time-stamps. Using 12.4 nm particles, solutions of 250 mg/L TiO_2 were exposed to light for 0.25, 0.5, 1, 2, 4, 7, 17, and 24 hours. The APF fluorescent indicator and buffer were added to the samples just before removing from the light and each sample was transferred to an amber vial.

Fourier transform-infrared spectroscopy measurements were performed using a Bruker Model Vertex70. Nanoparticle samples were prepared for FT-IR by placing a small amount of the functionalized nanoparticle suspension that was exposed to light onto a ZnSe salt plate and heating to dryness at 80 °C. The FT-IR measurements were taken in transmission mode using an air background and averaged over 100 scans. The spectra were background corrected within the Opus software.

3.2.10 Computational Studies for Ligand Degradation

To accompany experimental FTIR spectra, frequency computations were conducted. To simulation the vibrational frequencies of a carboxylic anchoring group to TiO_2, acetate was used to simplify the computation. Two conformations were examined: a bidentate bridging conformation of the two oxygen atoms bound to two nearby surface Ti atoms and a mono-ester conformation of one carboxyl oxygen bound to a surface Ti atom with the other surface Ti atom bound to a hydroxyl group. The “surface” of the clusters contained only the two Ti atoms linked together with an oxygen atom and all sites were fully terminated with hydrogen atoms to reduce computational time.

Computations were done using Gaussian09 using UB3LPY as the level of theory and LANL2DZ as the basis set. First, a geometry optimization was carried out, followed by a frequency calculation. Using GaussView, the various frequency peaks were identified with the corresponding molecular vibration.

3.2.11 ROS Total Yield Detection

To capture the total ROS produced over 24 hours, we used the spin trap molecule 2,2,6,6-Tetramethylpiperidin-1-yl)oxyl (TEMPO). TEMPO is well known to react with a wide range of radical species but is unreactive toward most other reactants. We measured the TEMPO concentration in samples using Electron Spin Resonance (ESR) spectroscopy, by integrating the characteristic electron spin signal from TEMPO. Electron spin resonance (ESR) spectra were measured using a Bruker EleXsys E500 EPR using an AquaX cell. A quantitative working curve was generated using the integrated ESR signal measured on samples with known TEMPO concentrations of 48.6, 24.3, 12.2, and 6.1 mM. This working curve was then used to determine the residual TEMPO concentration in the TiO_2 samples. For the determination of ROS produced by the TiO_2 nanoparticles, samples for ESR contained 48.6 mM of a radical trap and 250 mg/L solutions of 6.1 nm nanoparticles in 3 mL volumes to ensure the TEMPO molecule was in excess. Samples were illuminated for 0, 2, 4, 8, and 25 hours.

3.3 Results and Discussion

3.3.1 Synthesis and Functionalization

The success of the synthesis was confirmed using TEM and Raman Spectroscopy as shown in Chapter 2 Section 4.1 yielding anatase particles 6.1 ± 1.1, 10.1 ± 1.7, 13.8 ± 2.3, and 15.0 ± 2.2 nm in size. The size statistics were determined using the TEM images in ImageJ and manually counting and evaluating the size of each particle. The TEM images and corresponding histograms are shown in Figure 5.2. The functionalization of citrate was confirmed using FTIR as shown in Chapter 2 Section 4.2.

3.3.2 Light Exposure

Light exposure experiments were done with the XM 250 W 10,000K metal halide lamp that simulates sunlight at shallow depths in the ocean to correlate with collaborator studies on the toxicity and bioavailability of the particles in zebrafish. From light intensity experiments conducted by Professor Sanjay Joshi at Penn State University, the total absorbed flux above the band gap of anatase (3.2 eV or 387 nm) is 4 W/m^2 shown in Figure 3.3.

The nanoparticle samples are also placed in 24 or 96-well plates to mimic the toxicity studies. These plates and their corresponding lids are composed of polystyrene. A UV-Vis spectrum of a diluted TiO_2 nanoparticle sample overlaid with a UV-Vis spectrum of a lid of the 24-well plate is shown in Figure 3.4. This shows that below 300 nm, the polystyrene lid absorbs effectively all the photons of the lamp. Since the band gap of the nanoparticles is around 387 nm, only photons between 300 and 387 nm will

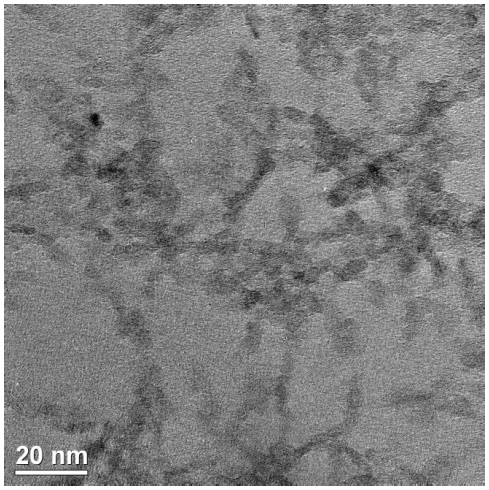
20 nm

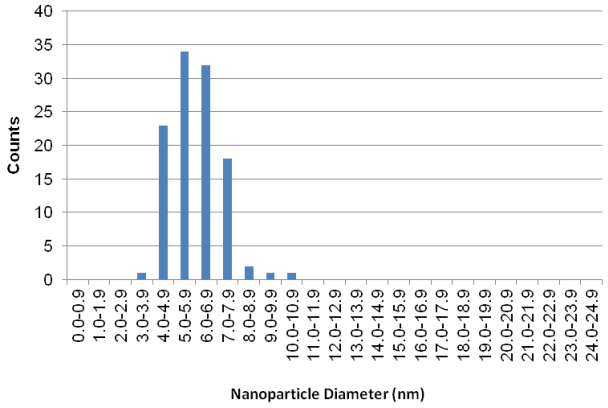
Counts
40
35
30
25
20
15
10
5
0
0.0-0.9
1.0-1.9
2.0-2.9
3.0-3.9
4.0-4.9
5.0-5.9
6.0-6.9
7.0-7.9
8.0-8.9
9.0-9.9
10.0-10.9
11.0-11.9
12.0-12.9
13.0-13.9
14.0-14.9
15.0-15.9
16.0-16.9
17.0-17.9
18.0-18.9
19.0-19.9
20.0-20.9
21.0-21.9
22.0-22.9
23.0-23.9
24.0-24.9
Nanoparticle Diameter (nm)

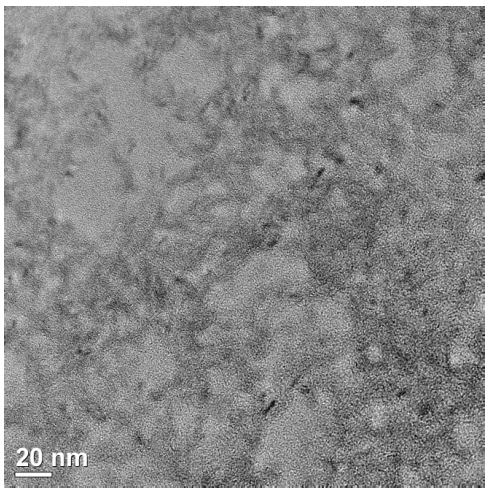
20 nm

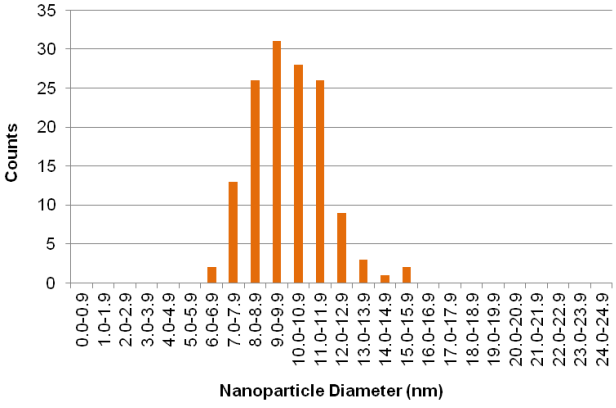
Counts
35
30
25
20
15
10
5
0
0.0-0.9
1.0-1.9
2.0-2.9
3.0-3.9
4.0-4.9
5.0-5.9
6.0-6.9
7.0-7.9
8.0-8.9
9.0-9.9
10.0-10.9
11.0-11.9
12.0-12.9
13.0-13.9
14.0-14.9
15.0-15.9
16.0-16.9
17.0-17.9
18.0-18.9
19.0-19.9
20.0-20.9
21.0-21.9
22.0-22.9
23.0-23.9
24.0-24.9
Nanoparticle Diameter (nm)

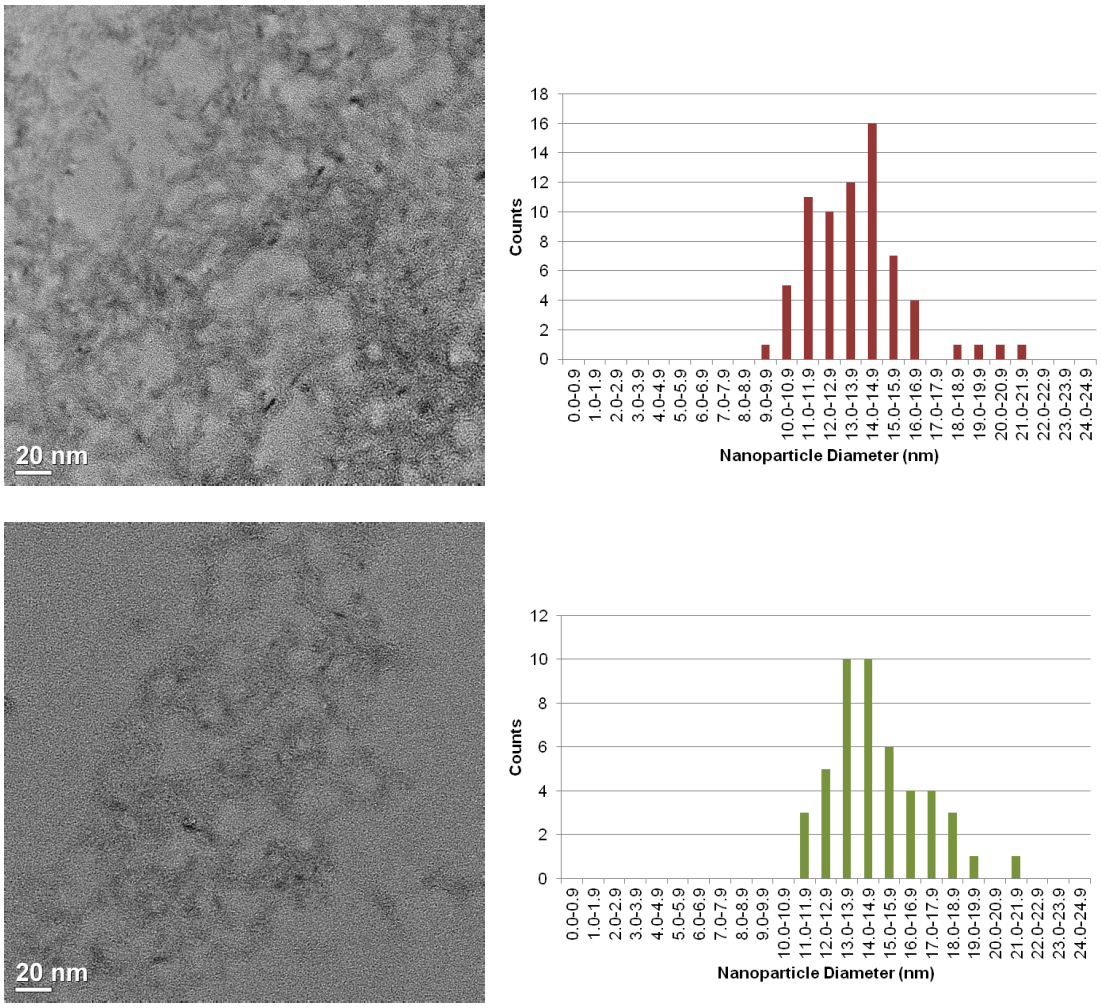

Figure 3.2: TEM images and size distributions of select TiO_2 samples used for size analysis. (Blue = 6.2 nm, Orange = 10.1 nm, Red = 13.8 nm, Green = 15.0 nm)

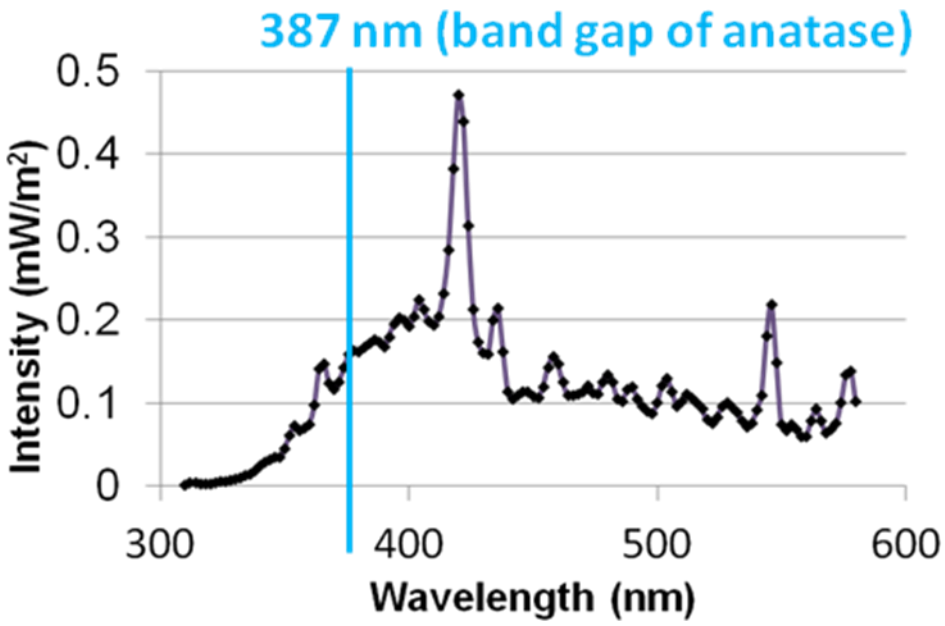

Figure 3.3: Lamp intensity spectrum of XM 250W 10,000K bulb. Intensity below the blue line at 387 nm is absorbed by the TiO_2 anatase nanoparticles.

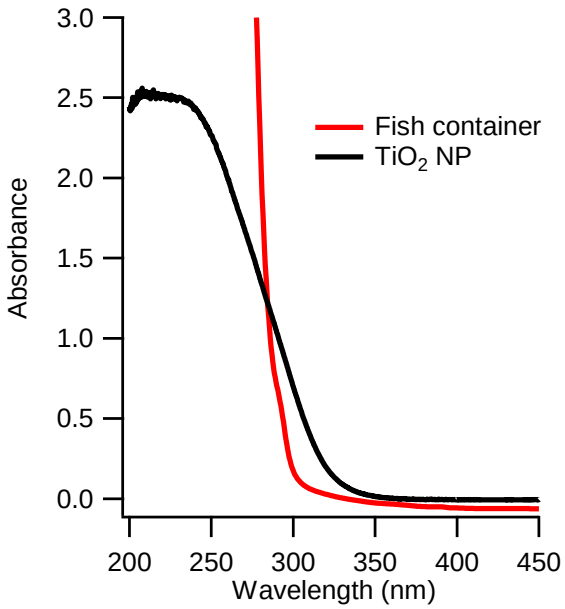

Figure 3.4: UV-Vis spectrum of a TiO_2 nanoparticle solution overlaid with the spectrum of a polystyrene 24-well plate fish container.

activate the TiO_2. Since the purpose of the lamp is to simulate sunlight under water, it is important for the nanoparticle solutions to be absorbing all the light below 387 nm. Therefore, for all studies, a quartz plate was used as the cover, which allows the UV light to pass through to the samples while preventing evaporation of the solutions.

3.3.3 Hydroxyl Radical Detection

There are two direct reactive oxygen species formed with the light activation of TiO_2, hydroxyl radicals and superoxide anion. The hydroxyl radical is a species with an unpaired electron, which will react nonspecifically with most organic materials within nanoseconds after their formation and has a short solution lifetime reacting within 1 to 5 molecular diameters of their formation.(*34–36*) Hydroxyl radicals have detrimental effects in genotoxicity and oxidative stress. The detection of hydroxyl radicals requires high sensitivity, high selectivity, and low detection limits.(*36*, *37*)

Fluorescence spectroscopy is a convenient laboratory method, making the use of a fluorescent indicator for ROS detection an attractive method. APF was chosen as the indicator since it is highly selective for hydroxyl radicals.(*36*, *37*) APF is a non-fluorescent molecule until it reacts with hydroxyl radicals resulting in the cleavage of the aminophenyl ring from the fluorescein and becoming highly fluorescent.(*36*, *37*) HRP can also catalyze the oxidation of APF by H_2O_2.(*36*, *37*)

The initial light reactions using Degussa P25 nanoparticle samples did not include the phosphate buffer at pH 7.2. Figure 3.5 shows pictures of samples with buffer added post-illumination and samples with buffer added initially. Without the buffer the solution is too acidic from the 18 MΩ-cm H_2O and the fluorescent indicator does not fluoresce.

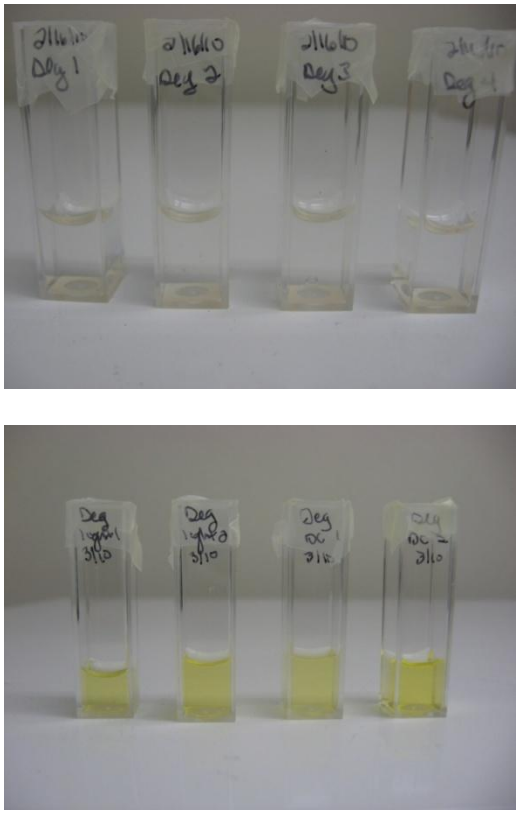

Figure 3.5: Light reaction samples of Degussa P25 TiO_2 nanoparticles with the addition of the APF fluorescent indicator. The top image does not contain the phosphate buffer pH 7.2 and the bottom image does.

However, at a buffered pH 7.2 the solution turns a yellow color and the fluorescence can be detected.

3.3.4 ROS Generation by Degussa P25 and Sun Nano

Degussa P25 is a TiO_2 photocatalyst that is used widely because of its relatively high levels of activity in many photocatalytic reaction systems.(*21*, *22*, *24–26*, *30*, *32*, *38–42*) It is composed of about 70% anatase and 30% rutile phases, however these percentages can range by up to 10%.(*26*) Sample TEM images in Figure 3.6 were used to measure an average size of 23 ± 9 nm for the batch of Degussa P25 used for these studies, which is more polydisperse than the synthesized particles (using 214 particles). The Sun Nano nanoparticles are a less studied TiO_2 nanoparticle that is reported to be completely of the anatase phase with a purity of 99.7% and an approximate particle size of 5-10 nm. The TEM images of the purchased batch are shown in Figure 3.7, where many of the particles are larger than 10 nm. The Degussa P25 and Sun Nano particles therefore differ in both phase composition and average size.

The quantification of ROS generation for the 10, 100, and 1000 mg/L is shown for both Degussa P25 and Sun Nano samples in Figure 3.8. This data was converted from fluorescence intensity of the APF indicator into a concentration of hydroxyl radicals using a standard curve. From this data an obvious increasing trend is noticed for both types of TiO_2 with increase in concentration. The Degussa P25 particles generate significantly less ROS for all three of the concentrations than the Sun Nano particles which can either be related to the different sizes and/or crystal phase. Since the

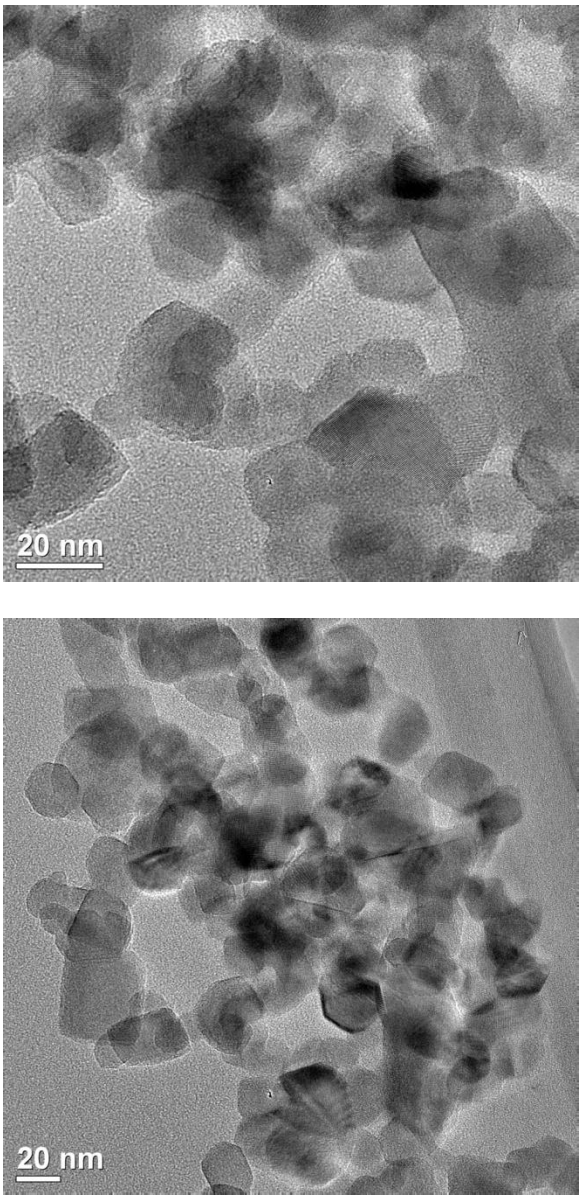

Figure 3.6: TEM images of purchased Degussa P25 nanoparticles.

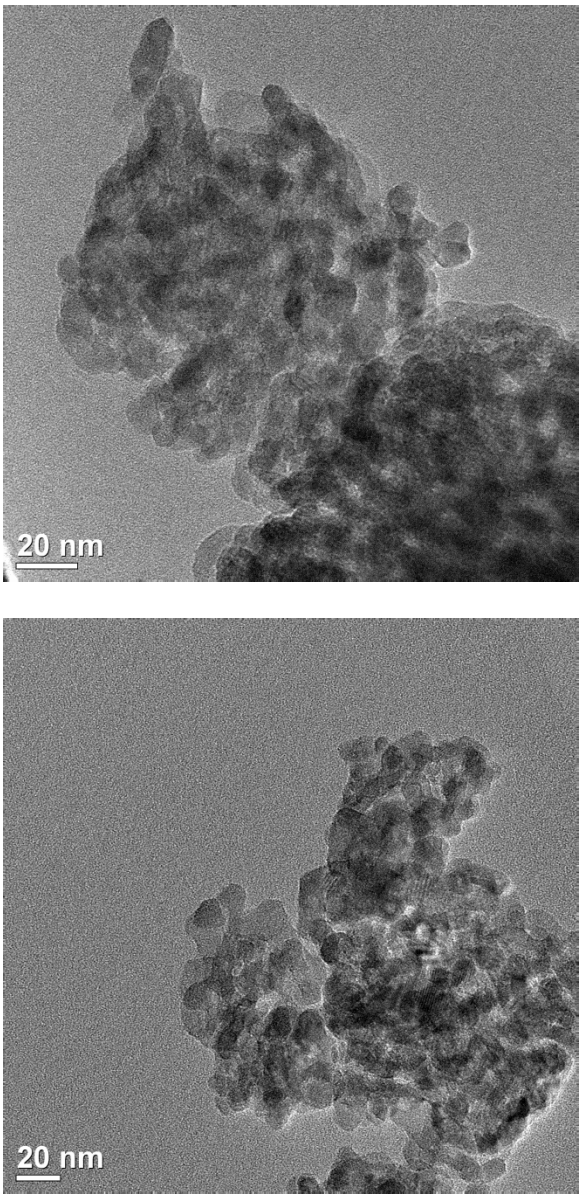

Figure 3.7: TEM images of purchases Sun Nano TiO_2 nanoparticles.

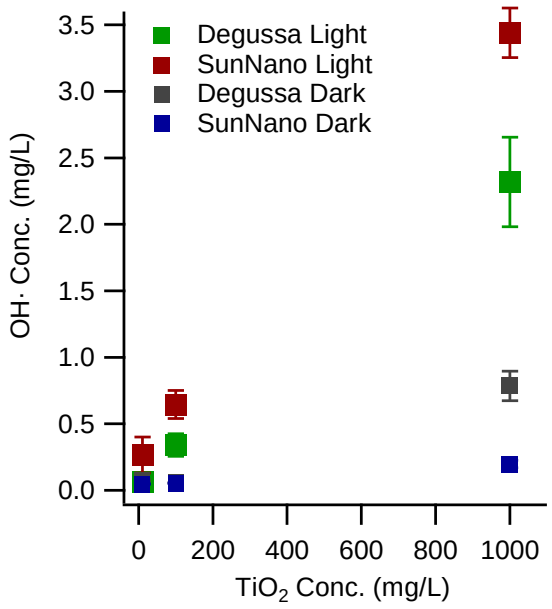

Figure 3.8: The quantization of ROS generation for the 10, 100, and 1000 mg/L of both Degussa P25 and Sun Nano samples using the APF fluorescent indicator for hydroxyl radicals.

differences could be attributed to either size or crystal phase, looking at well defined particles by synthesis is needed to determine the effects of both properties.

3.3.5 Influence of Buffer on ROS Generation

Although the phosphate buffer is important to ensure the APF indicator is at the proper pH for fluorescent detection, adding it to the nanoparticle samples can alter the nanoparticle-ligand system and environment. Phosphate groups are another anchoring group that is known to have an affinity for bonding to the surface of TiO_2 and could therefore undergo ligand exchange with the carboxylic acid ligands.(*42*, *43*) Originally, the buffer was added to the samples prior to light exposure where the phosphate ligands could eventually migrate to the surface, replacing the carboxylic acids. Since the surface ligands could affect ROS generation, adding the phosphate buffer initially can change the amount of ROS generated by the original TiO_2-citrate system. With the buffer added after the light exposure, any ROS generated would have been from the TiO_2-citrate system. Figure 3.9 shows the amount of ROS generated from the samples with the buffer added before exposure and the samples exposed after exposure. The amount of ROS detected is statistically different, making it important to add the buffer after light exposure at the same time as the APF indicator to ensure the ROS detected is from TiO_2-citrate system. In the presence of the buffer, more ROS is detected which indicates that the phosphate groups on the surface are less protective than the citrate.

3.3.6 ROS Generation in the Presence of Excess Ligand in Solution

The generation of hydroxyl radicals in the presence of excess citrate in solution is shown in Figure 3.10 for 0, 4, 10, 20, 40, 60, 80 and 100 mM of excess citrate in the 2

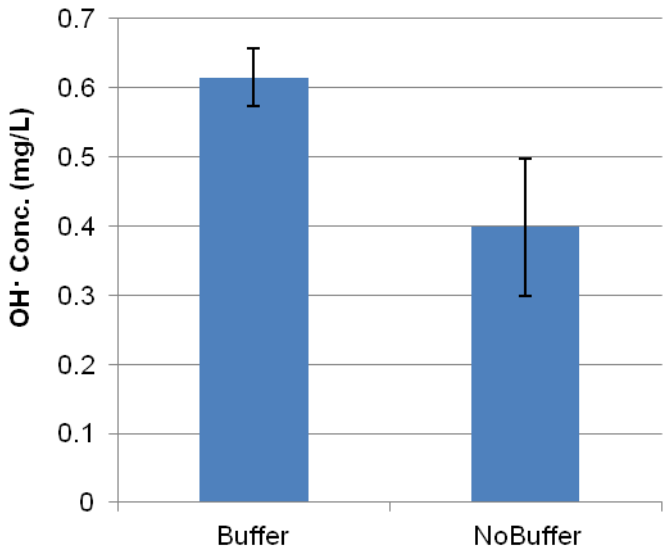

Figure 3.9: ROS generated from the TiO_2-citrate samples with the buffer added before exposure (buffer) and the samples exposed after exposure (no buffer).

mL solutions. A small variation can be seen with the initial addition of 4 mM of excess citrate to the solution, however, a large difference in ROS generation does not occur until 60 mM of excess citrate. At 100 mM of excess citrate, only about one third of the original ROS is being detected. Although the same amount of ROS might be generated in each of the cases, the more citrate that is present gives way to more organic material that can interact with the hydroxyl radicals before detection. The excess citrate also allows degraded organic ligands on the surface to be in equilibrium with the ligands in solution, therefore, giving a longer protection of the TiO_2 core. This gives insight not only to the presence of citrate itself, but also any organic materials that may appear in the environment.

3.3.7 ROS Generation based on Nanoparticle Size

It was hypothesized that the largest amount of ROS would be generated by particles of an intermediate size. Large particles would have increased volume recombination since electron and holes would be more likely to recombine than make their way to the surface to react with oxygen and water whereas in small particles the electron-hole pair would not be able to separate due to the small volume and would therefore recombine at the surface before generating ROS. These competing processes would suggest an intermediate size that would optimize the oxidation and reduction processes.

The graph in Figure 3.11 shows the hydroxyl radical concentrations generated by 250 and 500 mg/L TiO_2 for 6.1, 10.1, 13.8, and 15.0 nm nanoparticle samples for both light exposed and dark conditions. The generation of ROS in the dark is significantly less

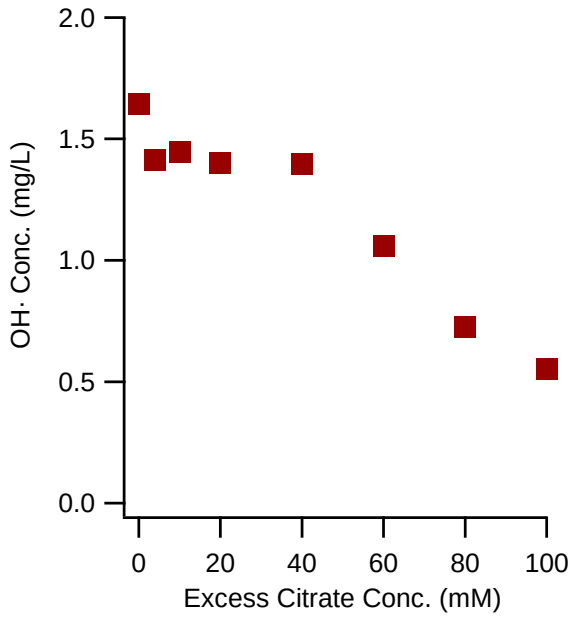

Figure 3.10: The generation of hydroxyl radicals based on excess citrate in solution for 0, 4, 10, 20, 40, 60, 80 and 100 mM of excess citrate in the solutions.

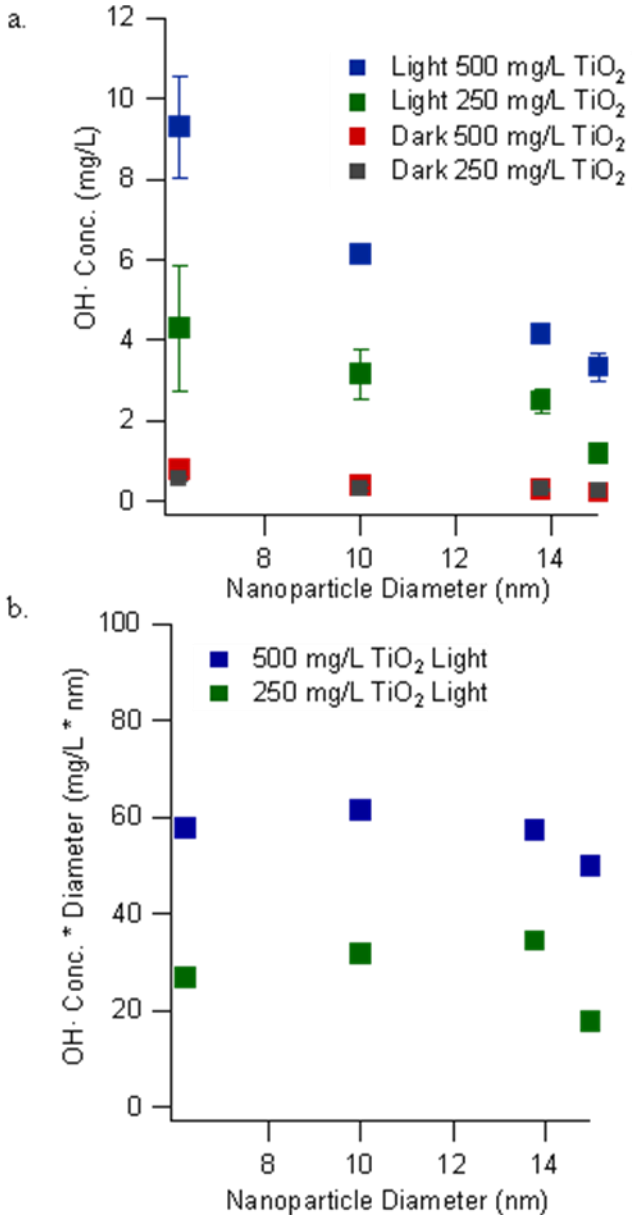

Figure 3.11: Hydroxyl radical concentrations generated by 250 and 500 mg/L TiO_2 for 6.1, 10.1, 13.8, and 15.0 nm nanoparticle samples for both light exposed and dark conditions. The second graph multiples the original data by the corresponding nanoparticle diameter.

than the amount generated under the simulated light, which confirms photoactivation of the TiO_2 nanoparticles. Also, the amount of ROS produced for the 500 mg/L samples is double (average of 2.2x) that produced by the 250 mg/L TiO_2 samples which shows that the production of ROS is linear with concentration. Among the different sizes there is a linear relationship where the largest detection of ROS occurred for the 6.1 nm samples. This indicates that the production of ROS is highly dependent on the surface area since these particles would have the most surface area available. The second graph shows the orginal data for the 250 and 500 mg/L illuminated samples multiplied by the diameter of the corresponding nanoparticles to further elucidate the impact of surface area. This shows a fairly uniform response, with a slight peak for the intermediate 10.1 nm and 13.8 nm samples.

3.3.8 Time-Dependent ROS Generation and Ligand Degradation

Figure 3.12 shows the time-dependent ROS generation of the 250 mg/L TiO_2 solutions of 12.4 nm particles sampled at 0.25, 0.5, 1, 2, 4, 7, 17, and 24 hours illumination times. The graph shows that the production of ROS reaches a steady state concentration of about 1.5 mg/L by 17 hours.

The FTIR spectra of the 1000 mg/L TiO_2 samples of 10.1 nm nanoparticles illuminated for 3, 4.5, 26 and 50 hours are shown in Figure 3.13. Since the spectra were taken in transmission mode, the absolute value of each peak cannot be compared from one sample to another. However, relative peak heights can give insight into the comparative amounts of each molecular species. Therefore, all the spectra are normalized to having the same peak height for the asymmetric CO_2^- stretch at 1620 cm^{-1}.

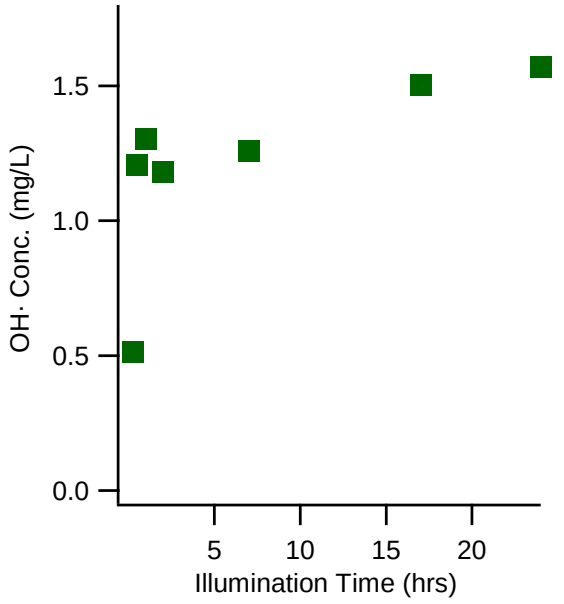

Figure 3.12: Time-dependent ROS generation of the 250 mg/L TiO_2 solutions of 12.4 nm particles sampled at 0.25, 0.5, 1, 2, 4, 7, 17, and 24 hours illumination times.

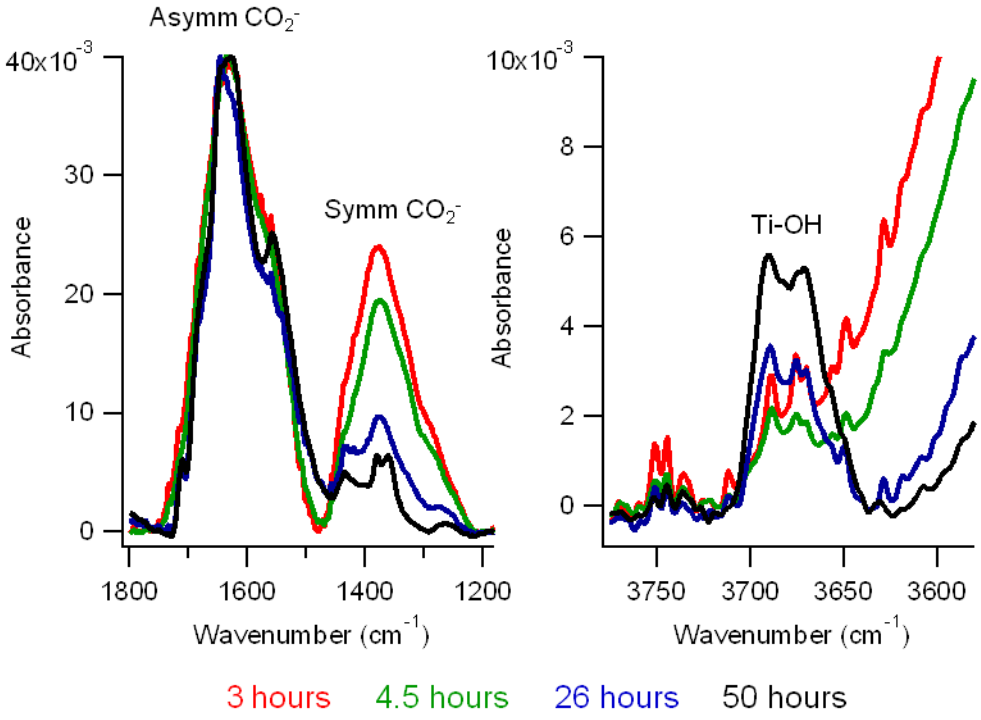

Figure 3.13: FTIR spectra of the 1000 mg/L TiO_2 samples of 10.1 nm nanoparticles illuminated for 3, 4.5, 26 and 50 hours.

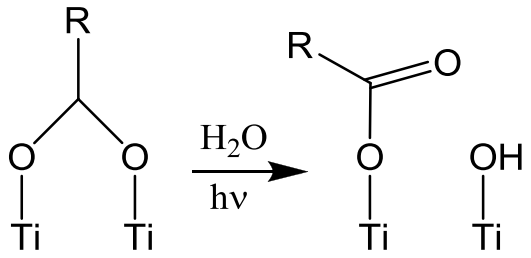

Figure 3.14: Possible degradation scheme for the carboxylate groups on the TiO_2 surface where in the presence of water and UV-light the carboxyl group changes from a bidentate bridging conformation to a monodentate ether conformation.

Relative to the asymmetric CO_2^- peak, the symmetric CO_2^- peak decreases and gains structure with illumination time and the TiO_2 surface hydroxyl peak at 3675 cm^{-1} increases in intensity. This indicates that the surface interaction between the citrate and the TiO_2 is changing with a proposed degradation scheme is shown in Figure 3.14, where in the presence of water and UV-light the carboxyl group changes from a bidentate bridging conformation to a monodentate ether conformation. The increase in surface hydroxyl groups indicates that the second surface Ti atom that was once associated with the carboxyl group is now hydroxylated.

3.3.9 Computational Studies for Ligand Degradation

The computational software program Gaussian09 has a molecular imaging program, GaussView, that allows for the visualization of each of the vibrations and the corresponding frequency they occur at. Therefore, although the models used for these calculations contained hydrogen atoms for termination, it is possible to distinguish which frequency vibrations are important to the molecular species of concern. This also is useful since the absolute value of the calculated frequencies is not accurate. Shown in Figure 3.15 are the molecular clusters and the corresponding simulated FTIR spectra in the range from 800-1600 cm^{-1}. The peaks highlighted in purple correspond to the asymmetric CO_2^- vibrations and the red highlighted peaks correspond to the symmetric CO_2^- vibrations. For the bidentate bridging conformation, the symmetric peak is larger than that of the asymmetric peaks and in the monodentate ether conformation the symmetric peak greatly decreases compared to the asymmetric peak. The spectra also show the growth of a Ti-OH peak at 3464 cm^{-1} for the mono-ether conformation not

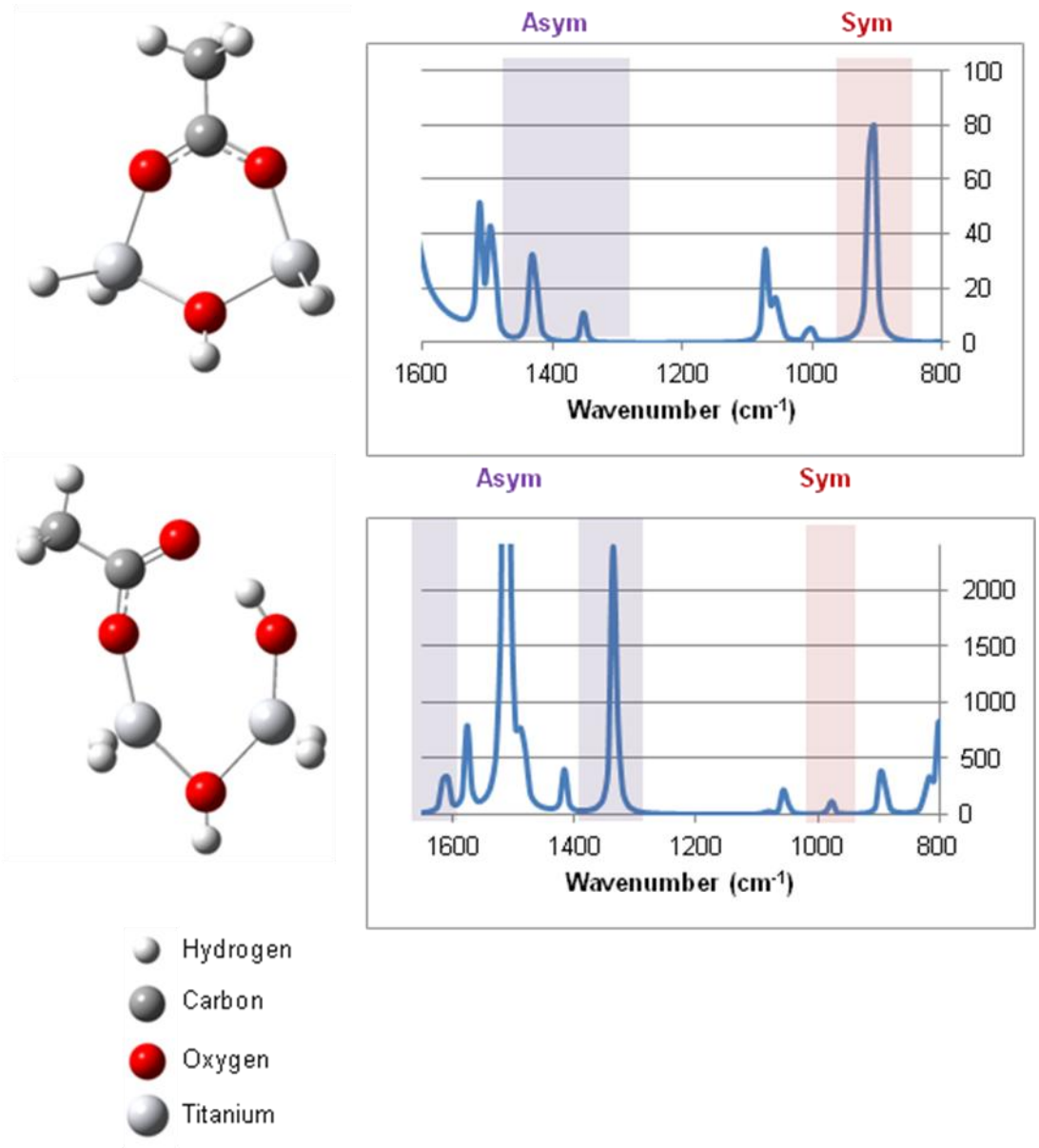

Figure 3.15: Molecular clusters of the bidentate bridging and monodentate ether conformations and the corresponding simulated FTIR spectra in the range from 800-1600 cm^{-1}. The highlighted purple sections correspond to the asymmetric CO_2^- vibrations and the red highlighted sections correspond to the symmetric CO_2^- vibrations.

shown. This gives insight that the proposed degradation scheme in Figure 3.14 is possible.

3.3.10 ROS Total Yield Detection

The AquaX cell for the ESR measurements was instrumental in allowing for the data to be taken in the original aqueous environment. The standard curve was created using the integrated areas of the 6.1, 12.2, 24.3, and 48.6 mM TEMPO signals and is linear with a R^2 value of 0.9942 using a y-intercept of zero. The integrated signals from each of the TiO_2 nanoparticle samples were adjusted to concentrations of ROS using the standard curve.

The 6.1 nm particles used for the total integrated ROS generation over 25 hours were from the same sample used in the size-dependent ROS study. For the size-dependent study using the 250 mg/L TiO_2 at 24 hours of illumination, 7 mg/L hydroxyl radicals were detected using the APF fluorescent indicator. The total integration using TEMPO as a spin trap in Figure 3.16, shows a generation of 222 mg/L ROS over the 25 hours. The total amount of ROS produced is also linear (R^2 = 0.9798)for the 25 hours which indicates that ROS is continuously being generated at constant amounts. This is consistent with the time-dependent data in Figure 3.16 showing a steady-state production of ROS.

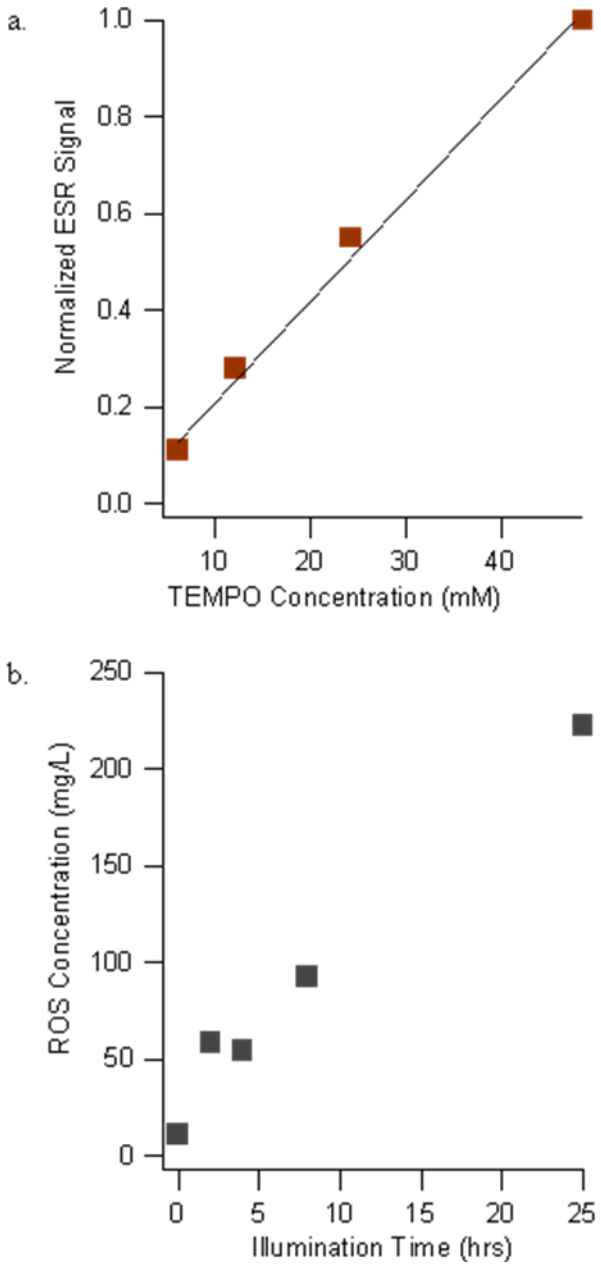

Figure 3.16: a) A standard concentration curve for TEMPO signal in the ESR and b) is the total integration of ROS generated over 25 hours using TEMPO as a spin trap.

3.4 Conclusions

This chapter has combined a number of factors that can influence the generation of ROS by TiO_2 nanoparticles in aqueous solution including the presence of a buffer, presence of excess ligand, nanoparticle size, light exposure time, and ligand degradation. At the molecular scale each of these parameters can have a significant impact on the detected ROS. To achieve reproducible and reliable results, it is important to understand if these factors have an impact and if so how. These results show that in fact all the factors do have an impact on the detection of generated ROS showing that the size and surface chemistry of the particles, as well as the surrounding environment, can greatly impact how TiO_2 nanoparticles affect the health and safety of society.

3.5 References

(1) Auffan, M.; Pedeutour, M.; Rose, J.; Mason, A.; Ziarelli, F.; Borschneck, D.; Chaneac, C.; Botta, C.; Chaurand, P.; Labille, J.; Bottero, J.-Y. Structural degradation at the surface of a TiO(2)-based nanomaterial used in cosmetics. *Environmental Science & Technology* **2010**, *44*, 2689-94.

(2) Fenoglio, I.; Greco, G.; Livraghi, S.; Fubini, B. Non-UV-induced radical reactions at the surface of TiO_2 nanoparticles that may trigger toxic responses. *Chemistry* **2009**, *15*, 4614-21.

(3) Jones, C. F.; Grainger, D. W. In vitro assessments of nanomaterial toxicity. *Advanced Drug Delivery Reviews* **2009**, *61*, 438-56.

(4) Kiser, M. A.; Westerhoff, P.; Benn, T.; Wang, Y.; Pérez-Rivera, J.; Hristovski, K. Titanium nanomaterial removal and release from wastewater treatment plants. *Environmental Science & Technology* **2009**, *43*, 6757-63.

(5) Liu, Y.; Liu, C.-yan; Zhang, Z.-ying Effects of carboxylic acids on the microstructure and performance of titania nanocrystals. *Chemical Engineering Journal* **2008**, *138*, 596-601.

(6) Nel, A.; Xia, T.; Mädler, L.; Li, N. Toxic potential of materials at the nanolevel. *Science* **2006**, *311*, 622-7.

(7) Sanders, K.; Degn, L. L.; Mundy, W. R.; Zucker, R. M.; Dreher, K.; Zhao, B.; Roberts, J. E.; Boyes, W. K. In vitro phototoxicity and hazard identification of nano-scale titanium dioxide. *Toxicology and Applied Pharmacology* **2012**, *258*, 226-36.

(8) Teow, Y.; Asharani, P. V.; Hande, M. P.; Valiyaveettil, S. Health impact and safety of engineered nanomaterials. *Chemical Communications* **2011**, *47*, 7025-38.

(9) Turkez, H. The role of ascorbic acid on titanium dioxide-induced genetic damage assessed by the comet assay and cytogenetic tests. *Experimental and Toxicologic Pathology* **2011**, *63*, 453-7.

(10) Birdi, K. S. *Handbook of Surface and Colloid Chemistry*; 3rd ed.; CRC Press: Boca Raton, FL, 2009.

(11) Grassian, V. H. When size really matters: Size-dependent properties and surface chemistry of metal and metal oxide nanoparticles in gas and liquid phase environments. *Journal of Physical Chemistry C* **2008**, *112*, 18303-18313.

(12) Karlsson, H. L.; Gustafsson, J.; Cronholm, P.; Möller, L. Size-dependent toxicity of metal oxide particles--a comparison between nano- and micrometer size. *Toxicology Letters* **2009**, *188*, 112-8.

(13) Heinlaan, M.; Ivask, A.; Blinova, I.; Dubourguier, H.-C.; Kahru, A. Toxicity of nanosized and bulk ZnO, CuO and TiO_2 to bacteria *Vibrio fischeri* and crustaceans *Daphnia magna* and *Thamnocephalus platyurus*. *Chemosphere* **2008**, *71*, 1308-16.

(14) Fabian, E.; Landsiedel, R.; Ma-Hock, L.; Wiench, K.; Wohlleben, W.; van Ravenzwaay, B. Tissue distribution and toxicity of intravenously administered titanium dioxide nanoparticles in rats. *Archives of Toxicology* **2008**, *82*, 151-7.

(15) Warheit, D. B.; Hoke, R. a; Finlay, C.; Donner, E. M.; Reed, K. L.; Sayes, C. M. Development of a base set of toxicity tests using ultrafine TiO_2 particles as a component of nanoparticle risk management. *Toxicology Letters* **2007**, *171*, 99-110.

(16) Chen, J.; Zhou, H.; Santulli, A. C.; Wong, S. S. Evaluating cytotoxicity and cellular uptake from the presence of variously processed TiO_2 nanostructured morphologies. *Chemical Research in Toxicology* **2010**, *23*, 871-9.

(17) Sayes, C. M.; Wahi, R.; Kurian, P. a; Liu, Y.; West, J. L.; Ausman, K. D.; Warheit, D. B.; Colvin, V. L. Correlating nanoscale titania structure with toxicity: a cytotoxicity and inflammatory response study with human dermal fibroblasts and human lung epithelial cells. *Toxicological Sciences* **2006**, *92*, 174-85.

(18) Wang, J.; Zhou, G.; Chen, C.; Yu, H.; Wang, T.; Ma, Y.; Jia, G.; Gao, Y.; Li, B.; Sun, J.; Li, Y.; Jiao, F.; Zhao, Y.; Chai, Z. Acute toxicity and biodistribution of different sized titanium dioxide particles in mice after oral administration. *Toxicology Letters* **2007**, *168*, 176-85.

(19) Baccheta, R., Santo, N., Fascio, U., et al. Nano-sized CuO, TiO_2 and ZnO affect *Xenopus laevis* development. *Nanotoxicology* **2012**, *6*, 381-398.

(20) Bar-Ilan, O.; Louis, K. M.; Yang, S. P.; Pedersen, J. A; Hamers, R. J.; Peterson, R. E.; Heideman, W. Titanium dioxide nanoparticles produce phototoxicity in the developing zebrafish. *Nanotoxicology* **2011**, *Early Online*, 1-10.

(21) Davydov, L. Quantification of the primary processes in aqueous heterogeneous photocatalysis using single-stage oxidation reactions. *Journal of Catalysis* **2000**, *191*, 105-115.

(22) Dolamic, I.; Burgi, T. Photocatalysis of dicarboxylic acids over TiO_2: An in situ ATR-IR study. *Journal of Catalysis* **2007**, *248*, 268-276.

(23) Erdem, B.; Hunsicker, R. a.; Simmons, G. W.; Sudol, E. D.; Dimonie, V. L.; El-Aasser, M. S. XPS and FTIR surface characterization of TiO_2 particles used in polymer encapsulation. *Langmuir* **2001**, *17*, 2664-2669.

(24) Fan, J.; Yates, J. T. Mechanism of photooxidation of trichloroethylene on TiO_2: Detection of intermediates by infrared spectroscopy. *Journal of the American Chemical Society* **1996**, *118*, 4686-4692.

(25) Karunakaran, C.; Dhanalakshmi, R. Photocatalytic performance of particulate semiconductors under natural sunshine—Oxidation of carboxylic acids. *Solar Energy Materials and Solar Cells* **2008**, *92*, 588-593.

(26) Long, T. C.; Saleh, N.; Tilton, R. D.; Gregory, V. Titanium dioxide (P25) produces reactive oxygen species in implications for nanoparticle. *Environmental Science & Technology* **2006**, *40*, 4346-4352.

(27) Linsebigler, A. L.; Lu, G.; Yates, J. T. Photocatalysis on TiO_2 surfaces: principles, mechanisms, and selected results. *Chemical Reviews* **1995**, *95*, 735-758.

(28) Mao, Y.; Schoneich, C.; Asmus, K.-dieter Identification of organic acids and other intermediates in oxidative degradation of chlorinated ethanes on TiO_2, surfaces en route to mineralization. A combined photocatalytic and radiation chemical study. *Journal of Physical Chemistry* **1991**, *95*, 10080-10089.

(29) Monticone, S.; Tufeu, R.; Kanaev, A. V.; Scolan, E.; Sanchez, C. Quantum size effect in TiO_2 nanoparticles: Does it exist? *Applied Surface Science* **2000**, *162-163*, 565-570.

(30) Vandermeulen, T.; Mattson, a; Osterlund, L. A comparative study of the photocatalytic oxidation of propane on anatase, rutile, and mixed-phase anatase–rutile TiO_2 nanoparticles: Role of surface intermediates. *Journal of Catalysis* **2007**, *251*, 131-144.

(31) Carraway, E. R.; Hoffman, A. J.; Hoffmann, M. R. Photocatalytic oxidation of organic acids on quantum-sized semiconductor colloids. *Environmental science & technology* **1994**, *28*, 786-93.

(32) Amadelli, R.; Maldotti, A.; Samiolo, L. Adsorption and photo-oxidation of 3,4-dihydroxy-cinnamic acid on TiO_2 films. *Catalysis Today* **2009**, *144*, 149-153.

(33) Kotsokechagia, T.; Cellesi, F.; Thomas, A.; Niederberger, M.; Tirelli, N. Preparation of ligand-free TiO_2 (anatase) nanoparticles through a nonaqueous process and their surface functionalization. *Langmuir* **2008**, *24*, 6988-97.

(34) Pryor, W. A. Oxy-radicals and Related Reactions. *Annual Review of Physiology* **1986**, *48*, 657-667.

(35) Sies, H. Oxidative stress: Oxidants and antioxidants. *Experimental Physiology* **1997**, *82*, 291-295.

(36) Cohn, C. A; Pedigo, C. E.; Hylton, S. N.; Simon, S. R.; Schoonen, M. A. Evaluating the use of 3'-(p-Aminophenyl) fluorescein for determining the formation of highly reactive oxygen species in particle suspensions. *Geochemical Transactions* **2009**, *10*, 8.

(37) Cohn, C. A; Simon, S. R.; Schoonen, M. A. Comparison of fluorescence-based techniques for the quantification of particle-induced hydroxyl radicals. *Particle and Fibre Toxicology* **2008**, *5*, 2.

(38) Schwarz, P. F.; Turro, N. J.; Bossmann, S. H.; Braun, A. M.; Wahab, A.M.; Dürr, H. A New method to determine the generation of hydroxyl radicals in illuminated TiO_2 suspensions. *The Journal of Physical Chemistry B* **1997**, *101*, 7127-7134.

(39) Guzman, F.; Chuang, S. S. C. Tracing the reaction steps involving oxygen and IR observable species in ethanol photocatalytic oxidation on TiO_2. *Journal of the American Chemical Society* **2010**, *132*, 1502-3.

(40) , E. S.; Litter, M. I.; Grela, M. A. Photoinduced reactivity of strongly coupled TiO_2 ligands under visible irradiation: An examination of an alizarin red@TiO_2 nanoparticulate system. *Journal of Physical Chemistry C* **2008**, *112*, 16532-16538.

(41) Carp, O. Photoinduced reactivity of titanium dioxide. *Progress in Solid State Chemistry* **2004**, *32*, 33-177.

(42) Chen, X.; Mao, S. S. Titanium dioxide nanomaterials: synthesis, properties, modifications, and applications. *Chemical Reviews* **2007**, *107*, 2891-959.

(43) Nilsing, M.; Persson, P.; Ojamae, L. Anchor group influence on molecule–metal oxide interfaces: Periodic hybrid DFT study of pyridine bound to TiO_2 via carboxylic and phosphonic acid. *Chemical Physics Letters* **2005**, *415*, 375-380.

Gaussian 09, Revision C.01, Frisch, M. J.; Trucks, G. W.; Schlegel, H. B.; Scuseria, G. E.; Robb, M. A.; Cheeseman, J. R.; Scalmani, G.; Barone, V.; Mennucci, B.; Petersson, G. A.; Nakatsuji, H.; Caricato, M.; Li, X.; Hratchian, H. P.; Izmaylov, A. F.; Bloino, J.; Zheng, G.; Sonnenberg, J. L.; Hada, M.; Ehara, M.; Toyota, K.; Fukuda, R.; Hasegawa, J.; Ishida, M.; Nakajima, T.; Honda, Y.; Kitao, O.; Nakai, H.; Vreven, T.; Montgomery, Jr., J. A.; Peralta, J. E.; Ogliaro, F.; Bearpark, M.; Heyd, J. J.; Brothers, E.; Kudin, K. N.; Staroverov, V. N.; Kobayashi, R.; Normand, J.; Raghavachari, K.; Rendell, A.; Burant, J. C.; Iyengar, S. S.; Tomasi, J.; Cossi, M.; Rega, N.; Millam, J. M.; Klene, M.; Knox, J. E.; Cross, J. B.; Bakken, V.; Adamo, C.; Jaramillo, J.; Gomperts, R.; Stratmann, R. E.; Yazyev, O.; Austin, A. J.; Cammi, R.; Pomelli, C.; Ochterski, J. W.; Martin, R. L.; Morokuma, K.; Zakrzewski, V. G.; Voth, G. A.; Salvador, P.; Dannenberg, J. J.; Dapprich, S.; Daniels, A. D.; Farkas, Ö.; Foresman, J. B.; Ortiz, J. V.; Cioslowski, J.; Fox, D. J. Gaussian, Inc., Wallingford CT, 2009.

GaussView, Version 5, Dennington, R.; Keith, T.; Millam, J. *Semichem Inc.*, Shawnee Mission KS, 2009.

Chapter 4

Design of a Modular Ligand to Reduce Reactive Oxygen Species Generation

4.1 Introduction

Titanium dioxide is a material that has been used commercially as a white pigment because of its brightness, high refractive index, and resistance to discoloration.(*1*) Common products include paints, sunscreens, cosmetics, electronics, pharmaceuticals, food, and health care products.(*2–7*) Traditionally, these products have used particles in the micrometer size ranges, however are moving to the nanometer regime. TiO_2 nanoparticles are becoming prevalent in commercialized products due to the fact that they are transparent to visible light but opaque to ultraviolet light making them attractable as UV blockers in sunscreens and plastics. Also, nanoparticles have unique physicochemical properties and functionalities that are different from their bulk counterparts.(*8*) In 2005, the global production of nanoscale TiO_2 was estimated to be 2000 tons worth $70 million, with large contributions from use in personal care products.(*1, 9*) Like most new technologies, nanomaterials offer the potential for both benefits and risks, and it is necessary to determine the health and safety impacts of these materials that are being introduced to society and the environment.(*9*)

As a well-known photocatalyst, TiO_2 produces reactive oxygen species (ROS) when exposed to light about its band-gap where the electron can reduce molecular oxygen into superoxide anion ($O_2^{\cdot -}$) and the hole can oxidize water into hydroxyl radicals ($OH^{\cdot}$). (*10–15*) These reactive oxygen species are known to cause oxidative stress, DNA

damage, and ultimately toxicity in organisms.(*3*) As the TiO_2 becomes smaller, there is an increase of surface area to volume ratio giving rise to higher surface reactivites.(*16*) As demonstrated in Chapter 3, the size of the nanoparticles plays a key role in the amount of ROS generated. A number of toxicity studies using various organisms have shown an increase in the mortality and malformations in the presence of UV exposed nanoparticles.(*2*, *3*, *16*–*28*)

For many applications of TiO_2, its photocatalytic activity is not necessary and in some cases can be detrimental. For example, TiO_2 (and other inorganics) in the nano-regime have been introduced to sunscreen formulations to reflect the UV radiation and reduce the amount of organic molecules needed to achieve desired SPF factors. When UV light from the sun is absorbed by the TiO_2 particles, photoactivation occurs and can lead to the formation of ROS. (*10*–*15*) Dunford et al. have shown that when DNA was exposed to simulated sunlight in the presence of TiO_2 particles, the hydroxyl radicals accelerated the breakage of the DNA chains.(*29*) With the sunscreen directly on the epidermis, it is important to prevent the photocatalytic activity that is the culprit of DNA damage.

Therefore, we would like to design the nanoparticle surfaces to reduce the photocatalytic activity and therefore also reduce the generation of reactive oxygen species. In order for the redox reactions that produce reactive oxygen species to occur, both the reduction and the oxidation need to take place. In the case of ROS generation, the electron reduces molecular oxygen (O_2) into the superoxide anion ($O_2^{\cdot -}$) and the hole oxidizes water (H_2O) into hydroxyl radicals ($OH^{\cdot}$). To reduce ROS generation, either

one or both of the redox reactions must be inhibited. As shown in Chapter 3, there are a variety of conditions that can affect the generation of ROS by the TiO_2 nanoparticles, including the surface ligands. We have hypothesized functionalizing the TiO_2 nanoparticles with a modular ligand which combines an inner hydrophobic ligand that is then chemically modified with an outer ligand. The hydrophobic ligand will be a barrier to the generation of ROS by preventing water from reaching the nanoparticle core. This would inhibit the creation of hydroxyl radicals through hole oxidation of the water. The outer ligand allows for the adaptation for use in a variety of applications.

A number of organic reactions can be used to produce a modular ligand, many of which are classified as "click" reactions. The phrase "click chemistry" was first coined by K. Barry Sharpless in 2001 as describing a variety of reactions that are modular, wide in scope, give very high chemical yields, generate only inoffensive byproducts, and are stereospecific.(*30*) The process must have simple reaction conditions, readily available starting materials, no solvent or a benign solvent, and simple product isolation. The original driving force for these reactions was to mimic nature by joining small chemical units together with heteroatom links (C-X-C).(*30*)

One of the most popular "click" reactions is the Cu (I) catalyzed azide alkyne cycloaddition (CuAAC), which couples a terminal azide with an alkyne, creating a 1,4-disubstituted 1,2,3-triazole linkage via a [3 + 2] Huisgen cycloaddition. This reaction is an excellent example of "click" chemistry because of its selectivity and tolerance to a variety of reaction conditions.(*31*) In more recent years, this reaction has been demonstrated on a number of surfaces including gold, silicon, carbon nanofibers, and

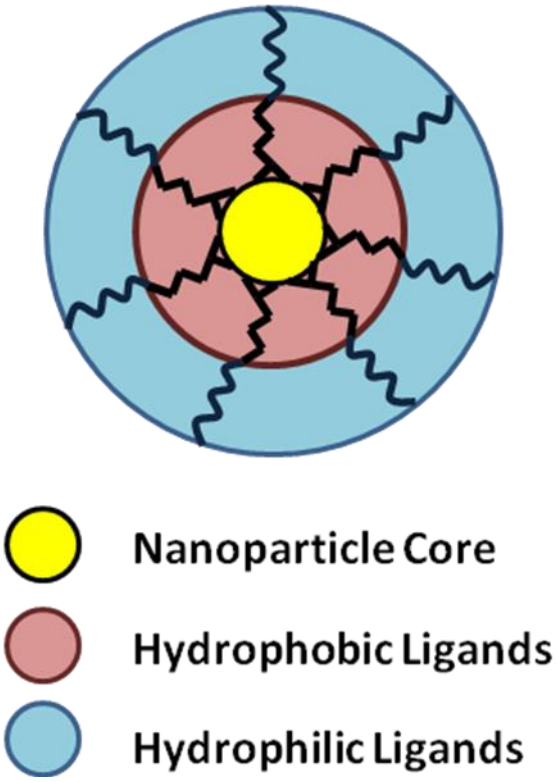

Figure 4.1: Modular functionalization scheme to reduce the generation of ROS by illuminated TiO_2 nanoparticles. The yellow represents the nanoparticles core, the red represents the hydrophobic ligand first attached to the surface, and the blue represents a hydrophilic ligand (or ligand with desired functionality) that is easily attached to the hydrophobic molecule.

metal oxide heterostructures.(*32–36*) Due to the mild conditions of this reaction, there is generally no concern about the etching of the surfaces.

However, the copper catalyzed [3 + 2] Huisgen cycloaddition is shown to leave behind residual amounts of copper which can be problematic for biological applications and could also cause additional toxicity in aquatic life.(*37*) This has led to efforts in developing metal-free synthesis techniques. One technique is to modify the Huisgen cycloaddition reaction to allow the removal of the copper and its reducing agent. This has been explored in the literature, but involves the addition of heat, light, or a limited number of possible reagents making the reaction less modular and less useful for many applications.(*38*, *39*) Another promising method is the family of thiol-ene addition reactions.(*40*, *41*) This type of reaction can proceed via two different routes: anti-Markovnikov radical reaction or a base- or nucleophile-catalyzed Michael addition reaction. The anti-Markovnikov reaction requires the use of an external radical and energy to generate the radicals. Through this mechanism, the thiol compounds may react non-selectively with any vinyl bonds. For the Michael addition reaction, a facile reaction occurs between the nucleophilic species and activated olefins under basic conditions. This reaction has the benefits of mild reaction conditions, minimal by-products, and high conversions when optimized.(*40*, *41*)

Understanding the production of ROS based on the surface functionalization of TiO_2 NPs along with the corresponding ligand degradation is critical in ultimately determining the environmental safety of these nanomaterials.

4.2 Experimental Methods

4.2.1 Chemicals

Reagents used for the Cu(I) catalyzed azide alkyne cycloaddition include 10-undecynoic acid (406546, Aldrich), azido-dPEG®4-alcohol (10541, Quanta Biodesign Limited), azido-dPEG®8-alcohol (10542, Quanta Biodesign Limited), Cu(II) tetrafluoroborate hydrate (366587, Aldrich), tris[(1-benzyl-1H-1,2,3-triazol-4-yl)methyl]amine (TBTA) (678937, Aldrich), (+)-sodium L-ascorbate (A7631, Sigma), and hydroquinone (H9003, Sigma-Aldrich).

For the Michael's Addition reaction, reagents used were 11-mercapto-undecanoic acid (450561, Aldrich), poly(ethylene glycol) methyl ether acrylate (454990, Aldrich), and dimethylphenylphosphine (265020, Aldrich).

For the hydrophilic ligand, a six-unit PEG chain terminated with an alcohol and an acid group (HO-PEG6-COOH) was custom synthesized by ChemPep, Inc. and was >98% pure.

All water used is brought to 18.0-18.2 MΩ-cm resistivity using a Barnstead NANOpure Infinity ultrapure water system with an organic-free filter cartridge. A 0.5 M NaOH solution was made using NaOH (S318, Fisher Scientific) in 18 MΩ-cm H_2O.

4.2.2 Synthesis of TiO_2 Nanoparticles

The TiO_2 nanoparticles used for this study were based on the synthesis by Kotsokechagia et al.(*42*) In a round bottom flask, 5 mL of $TiCl_4$ were added to 25 mL of anhydrous ethanol to create titanol groups. After 2 minutes of stirring, 100 mL of

anhydrous benzyl alcohol were added to the solution as the reaction medium. The solution was heated at 85 °C for 6.5 hours after which the solution became cloudy and was transferred to centrifuge tubes with 15 mL of solution in each. The particles were sedimented out of solution using a 1:2 (v:v) ratio of diethyl ether to nanoparticle suspension. The mixture was centrifuged at 4000 g for 10 minutes or until the supernatant was clear and the nanoparticles created a white solid pellet at the bottom. The liquid supernatant was decanted and the nanoparticles were suspended by sonication in a 1:1 (v:v) solution of 18 MΩ-cm:ethanol adjusted to pH 1 using concentrated HCl. A variety of sizes can be synthesized by varying the time of heating.

4.2.3 Cu Catalyzed Azide Alkyne Cycloaddition (CuAAC)

The initial functionalization was done using a 5 mM solution of undecynoic acid in 18 MΩ-cm H_2O brought to pH 8 using 0.5 M NaOH. The solution was heated at 80 °C for ten minutes to help dissolve the acid. The solution was then added to the particles crashed out of the storage solution. The final solution had a pH of 5, which is below the point of zero charge of the TiO_2 nanoparticles. The samples were sonicated for 3 hours, leaving unstable functionalized particles in water.

The azide-alkyne cycloaddition was carried out by adding to the solution 1.2 mM azido-dPEG8-alcohol, 0.5 mM Cu(II)(tris-benzyltriazolyl-methyl)amine)tetra-fluoroborate hydryte (TBTA), and 6.5 mM sodium ascorbate. Upon addition, the solution immediately turned orange. The solution was stirred for 24 hours at room temperature.

Samples were dialyzed using a cellulose membrane (Sigma Aldrich #D9777, molecular weight cut-off 12,400 Da) in 18 MΩ-cm H_2O for two 24 hour periods to

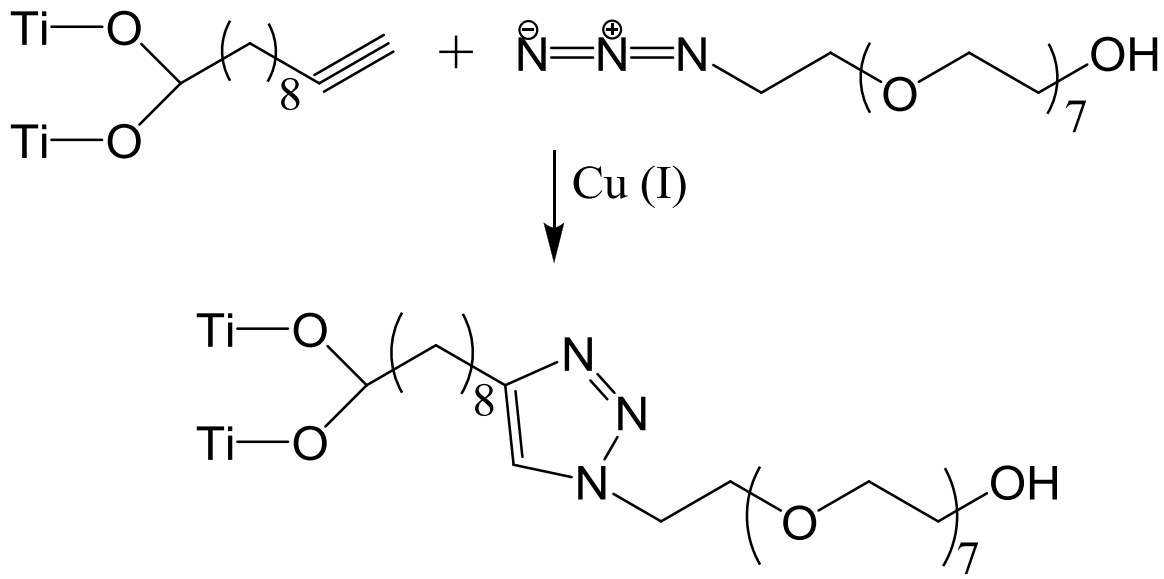

Figure 4.2: Chemical reaction scheme of the copper-catalyzed azide alkyne cycloadditon "click" reaction.

remove any excess ligands.

4.2.4 CuAAC Control Reactions

A control reaction was carried out using all the reagents except the copper catalyst. The nanoparticles were functionalized with a solution of 5 mM undecynoic acid in the same fashion as in secion 4.2.3. After sonication, 1.2 mM azido-dPEG8-alcohol was directly added to the solution. The white, opaque solution was stirred for 24 hours and was dialyzed using a cellulose membrane (Sigma Aldrich #D9777, molecular weight cut-off 12,400 Da) in 18 MΩ-cm H_2O for two 24 hour periods to remove any excess ligands.

4.2.5 Michael Addition Thiol-ene Reaction

The hydrophobic ligand was functionalized to the surface using a 4 mM solution of 11-mercapto-undecanoic acid (MCUA) in 15 mL of acetone. The solution was added to the TiO_2 nanoparticle pellet crashed out of the storage solution. Once agitated into solution, the nanoparticle suspension was bath sonicated for 3 hours giving a well-dispersed colloid solution.

The Michael addition thiol-ene reaction was carried out with a ratio alkene:thiol:catalyst of 1:1.2:0.2. Therefore, 3.3 mM of poly(ethylene glycol) methyl ether acrylate and 0.7 mM dimethylphenylphosphine (DMPP) were used. Due to the odor of dimethylphenylphosphine, this was carried out in a well-ventilated hood. The solution was stirred overnight at room temperature. The particles did not become a stable colloid suspension in the acetone and

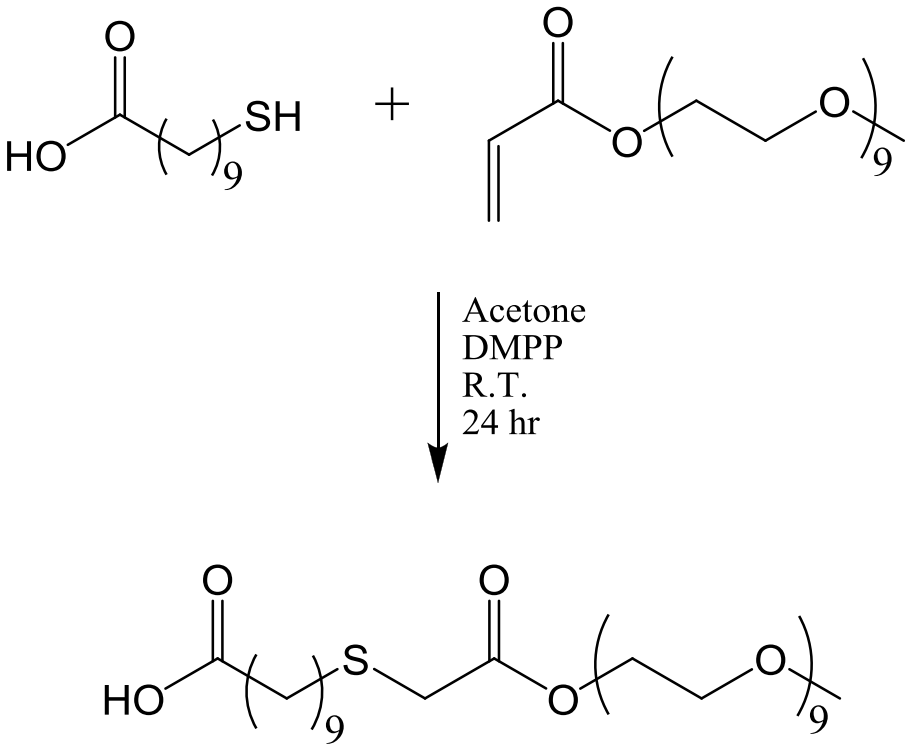

Figure 4.3: Chemical reaction scheme for the Michael's addition thiol-ene "click" reaction.

were centrifuged out of solution without the need for an additional solvent. The pellet of TiO_2 nanoparticles was then re-suspended in a solution of 18 MΩ-cm H_2O.

Samples were dialyzed using a cellulose membrane (Sigma Aldrich #D9777, molecular weight cut-off 12,400 Da) in 18 MΩ-cm H_2O for two 24 hour periods to remove any excess ligands.

4.2.6 Thiol-ene Control Reactions

The first control did not include the dimethylphenylphosphine catalyst. The particles were functionalized with a 4 mM solution of 11- mercapto-undecanoic acid in 15 mL of acetone. The solution was sonicated for 3 hours. Then 3.3 mM of poly(ethylene glycol) methyl ether acrylate was added to the solution and which was stirred for 24 hours at room temperature.

The second control carried out the reaction without first functionalizing with the hydrophobic ligand. A solution of 3.3 mM poly(ethylene glycol) methyl ether acrylate and 0.7 mM dimethylphenylphosphine catalyst in 15 mL of acetone was added to the pellet of TiO_2 nanoparticles crashed out of the storage solution. The solution was first sonicated for 3 hours to break up the pellet into the solution and was then stirred for 24 hours at room temperature.

The two control samples were sedimented of the acetone solutions with centrifugation (10 min at 4000 g) and were re-suspended in 18 MΩ-cm H_2O. Samples were dialyzed using a cellulose membrane (Sigma Aldrich #D9777, molecular weight cut-off 12,400 Da) in 18 MΩ-cm H_2O for two 24 hour periods to remove any excess ligands.

4.2.7 Hydrophilic PEGylation

To determine the effectiveness of the hydrophobic "inner" ligand, a control functionalization was done using a fully hydrophilic PEG ligand. The functionalization was carried out using a 5 mM solution of HO-PEG6-COOH in 25 mL of 18 MΩ-cm H_2O. The solution was added to the sedimented TiO_2 nanoparticles and bath sonicated for 3 hours. The solution was dialyzed using a cellulose membrane (Sigma Aldrich #D9777, molecular weight cut-off 12,400 Da) in 18 MΩ-cm H_2O for two 24 hour periods to remove any excess ligands.

4.2.8 Characterization of Functionalization

Infrared absorption measurements were performed using a Bruker Model Vertex70 Fourier-transform infrared spectrometer equipped with a liquid nitrogen-cooled mercury cadmium telluride detector. Nanoparticle samples were prepared for FT-IR analysis by placing a small amount of the functionalized nanoparticle suspension onto a ZnSe salt plate and heating to dryness at 80 °C. The FT-IR measurements were obtained in transmission mode using an air background and averaged over 100 scans. The spectra were background-corrected within the Opus software.

Samples were characterized using XPS in an ultrahigh vacuum system equipped with a load-lock for sample introduction, a monochromatized Al Kα source (1486.6 eV), and a hemispherical analyzer with a 16-channel detector array. The survey was taken from 0-1400 eV, with 0.8 eV/step, a pass energy of 187.85, and averaged over 5 sweeps. All multiplex measurements were taken with a 58.7 eV pass energy with 0.125 eV/step. The number of scans for each element were C (1s) 10 scans, Cu (2p) 20 scans, N (1s) 30

scans, O (1s) 5 scans, P (2p) 10 scans, S (2p) 30 scans, S (2s) 20 scans, and Ti (2p) 5 scans. All data was taken with an electron take-off angle was 45º and peak positions and areas were calculated by fitting raw data to Voigt functions after a Shirley background correction performed using the software package IGOR.

4.2.9 Light Exposure

Sunlight was simulated using a 250 W blue-spectrum metal halide lamp (XM 250W, 10,000K; electronic ballast; XM Lighting, Anaheim, CA) designed to mimic sunlight at shallow depths in the ocean. From light intensity experiments conducted by Professor Sanjay Joshi at Penn State University, the total absorbed flux above the band gap of anatase (3.2 eV or 387 nm) is 4 W/m^2. Studies were carried out using 300 μL of solution in 96-well plates using a quartz plate as the cover. Dark samples were placed under the light but were completely covered in aluminum foil to allow for the same temperature fluctuations but prevent the exposure to light. The sample plates were placed 18 inches under the metal halide lamp.

Samples were diluted to 250 mg/L TiO_2 using 18 MΩ-cm H_2O that was purged with Ar gas and left out of the light for at least one month. The samples were left under the light for 0, 0.5, 1, 2, 4, 8, 16, 24, and 48 hours. Each sample was performed in triplicate for hydroxyl detection and one sample of each was also made for both FTIR and XPS where the APF indicator was omitted.

4.2.10 Characterization of Light Exposed Samples

Hydroxyl radicals ($OH^{\cdot}$) were measured quantitatively using a fluorescent probe,

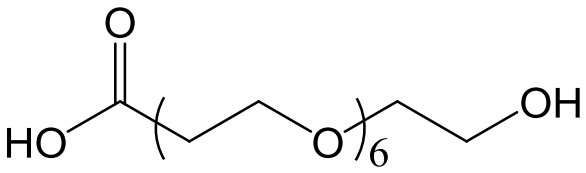

Figure 4.4: Hydrophilic HO-PEG6-COOH molecule.

3'-(*p*-aminophenyl) fluorescein (APF).(*43*, *44*) After samples were exposed to light or dark conditions, 10 μM APF and 100 mM phosphate buffer pH 7.2 were added to each sample. The samples were then transferred to amber vials to prevent additional light exposure. Steady-state fluorescence measurements were taken using an ISS K2 Time-Resolved Spectrofluorometer using slit sizes of 2.0 mm and 0.5 mm for the excitation and emission respectively. The samples were excited at 490 nm and emission peak occurred between 510 and 525 nm. To prevent over-saturation of the photon-counting detector, each of the samples were diluted by a factor of 10. A linear quantitative curve was used to determine concentrations of $OH^{\cdot}$ present in each sample.

4.3 Results and Discussion

4.3.1 Cu Catalyzed Azide Alkyne Cycloaddition (CuAAC)

Although the hydrophobic nanoparticles should not be a stable suspension in water, they do give a small amount of repulsion to prevent the particles from agglomerating according to DLVO theory. However, since the hydrophobically-coated particles did not form a stabile colloidal suspension, the solution was most likely in a secondary minimum from DLVO theory.

FTIR and XPS spectra were evaluated after both the hydrophobic attachment and after the hydrophilic molecule were added. The results were compared to those of the control reaction. From an FTIR perspective, it would be easier to characterize an azide attached to the surface and track its disappearance after the “click” reaction since there is a strong azide vibration at 2098 cm^{-1}. The characteristic peaks of an alkyne are much

weaker at 2118 and 3312 cm^{-1}. However, for this study, the alkyne was attached to the surface due to the availability of commercial products.

In Figure 4.5, the FTIR spectra of the alkyne functionalized nanoparticles, the neat azide terminated PEG, and the full CuAAC click reaction performed on TiO_2 nanoparticles after dialysis are shown. The key molecular vibrations of the N_3, C=O, and C-O-C are highlighted in green, blue, and red respectively. The full CuAAC spectrum shows the lack of an N_3 peak but also maintains the C=O vibration from the acid group of the alkyne as well the C-O-C vibration of the azide-PEG molecule.

In the XPS spectra shown in Figure 4.6, the N (1s) peak of the full CuAAC click reaction and the control reaction without the addition of the Cu catalyst are shown. These data show the presence of the triazole ring nitrogen at 399 eV and the absence of a peak at 402 eV attributed to unreacted azide due to the positively charged nitrogen species.(*36*) By quantitative analysis of the N(1s) and Ti (2p) peaks of the CuAAC functionalization, about 1-2 molecules/nm^2 are on the surface. The N (1s) spectrum from the control reaction (no copper) does not show the presence of any nitrogen, including non-specifically bound azide-PEG.

For chemical studies of the surface species on nanoparticles a “neat” surface with few impurities is preferred. One problem encountered with the CuAAC reaction is that the ascorbate used as the reducing agent has reactive sites for binding to the TiO_2 as well. This caused a mixed surface of “click” ligands interspersed with ascorbate molecules.

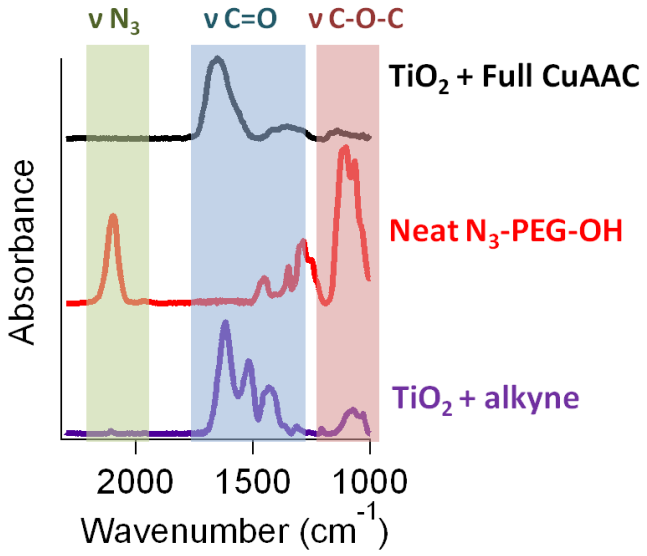

Figure 4.5: FTIR spectra of the alkyne functionalized nanoparticles, the neat azide terminated PEG, and the full CuAAC click reaction on TiO_2 nanoparticles after dialysis are shown. The key molecular vibrations of the N_3, C=O, and C-O-C are highlighted in green, blue, and red respectively.

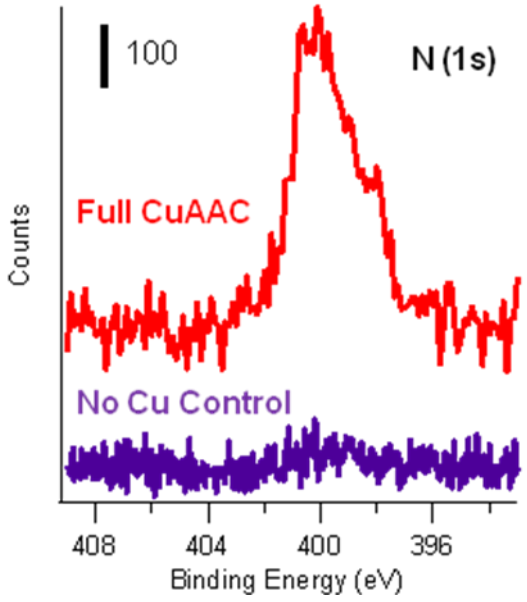

Figure 4.6: The N (1s) XPS spectra of the full CuAAC functionalized nanoparticles and the control nanoparticles functionalized without the addition of the Cu catalyst.

4.3.2 Michael Addition Thiol-ene Reaction

The Michael addition thiol-ene reaction used reagents that were optimized by Li et al.(*40*) To prevent similar issues as with the ascorbate in the CuAAC reaction, dimethylphenylphosphine was chosen as the catalyst since it does not contain any group that would be likely to react with the TiO_2 surface. In the literature, Li et al. do not report the reaction between the thiol-acid with poly(ethylene glycol) methylether acrylate using the dimethylphenylphosphine catalyst.(*40*) Other thiol-ene reactions using this catalyst have reported yields mostly ranging from 70 to 100% conversion.(*40*) For the purposes of catalyst solubility, the reaction was conducted in acetone instead of water.

Unfortunately, for this reaction there was no element present that could be tracked using XPS to help determine in the thiol-ene "click" reaction had occurred. The reaction does contain sulfur which could be used as a tag in the XPS, however, the nanoparticle solutions are cast onto silicon wafers and the S (2p) peak can be overlapped with a Si (2s) peak. Also, peak positions from a primary thiol to a secondary thiol would be very difficult to discern in the XPS spectra. However, there is a high amount of oxidized carbon in the functionalized samples at 287.6 eV shown in the C (1s) spectrum in Figure 4.7. This is due to the presence of the –C-O-C- species of the poly(ethylene glycol) methylether acrylate molecule. Therefore, the ligands have either undergone the "click" reaction, or the poly(ethylene glycol) methylether acrylate is non-specifically binding to the nanoparticles. By comparing the oxidized carbon peaks from the MCUA only, the control with no DMPP catalyst, and the full thiol-ene click reaction, there is some oxidized carbon for the MCUA, slightly more for the control and the most for the full

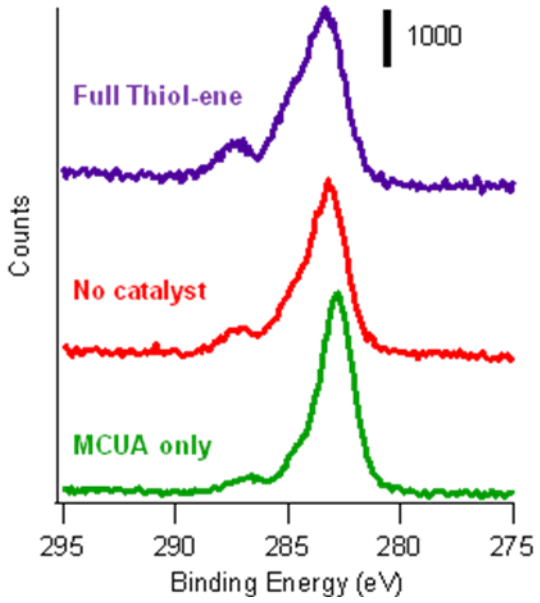

Figure 4.7: XPS spectra of the carbon (1s) peak for MCUA, full thiol-ene "click" reaction, and no catalyst control functionalized TiO_2 nanoparticles.

thiol-ene. There is some non-specific binding in the no catalyst control, however, the full thiol-ene is most successful for the addition of the PEG chain.

4.3.3 ROS Generation

The ROS concentrations detected after 24 hours of illumination of the two methods of "click" reaction modified nanoparticles were compared to the ROS detected from hydrophilic HO-PEG6-COOH functionalized nanoparticles and citrate coated 6.1 nm particles of Chapter 3. The citrate modified particles produce over 4 mg/L hydroxyl radicals. The HO-PEG6-COOH functionalized nanoparticles reduce the amount ROS generated down to slightly more than 2 mg/L. The nanoparticles modified by the CuAAC reaction and the thiol-ene reaction dramatically reduce the ROS generation further by producing negligible amounts of hydroxyl radicals in the light as they do in the dark. The reduction of ROS generation by the hydrophilic HO-PEG6-COOH without the hydrophobic coating can be attributed to the addition of excess organic ligand than the smaller citrate ligands. As shown in Chapter 3 section 3.3.7, the excess organic material can reduce the amount of ROS detected since the hydroxyl radicals can react with the organic material at the surface. However, with the "click" modified particles less than half of the hydroxyl radicals were detected than for the hydrophilic particles, the hydrophobic coating does provide a better barrier to ROS generation.

The time-dependent ROS generation of the CuAAC and thiol-ene "click" reaction modified nanoparticles is shown in Figure 4.9. There is a rise in the hydroxyl radical concentration at 4 hours, but then the generation reaches a steady state of about 1.5 mg/L for the CuAAC modified and 1.0 mg/L for the thiol-ene modified nanoparticles.

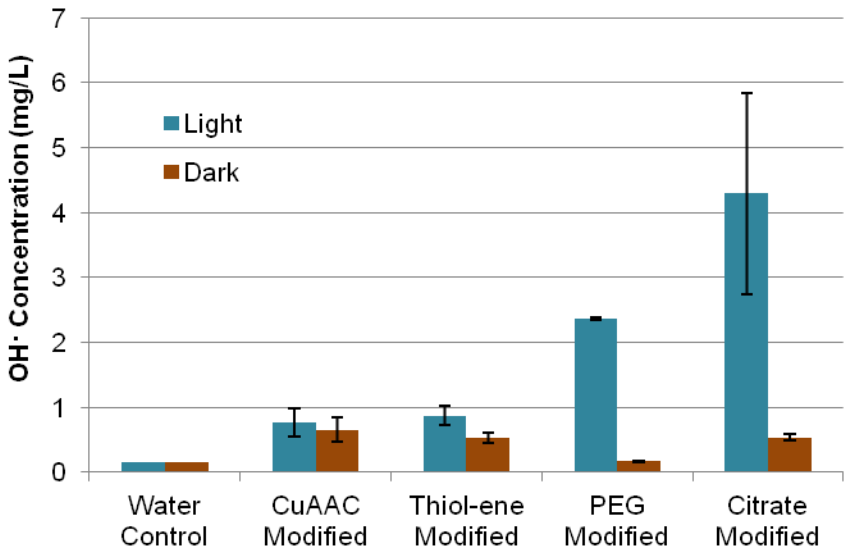

Figure 4.8: Concentration of hydroxyl radicals produced by CuAAC, thiol-ene, HO-PEG6-COOH, and citrate modified TiO_2 nanoparticles. The hydroxyl radicals were detected by the APF fluorescent indicator.

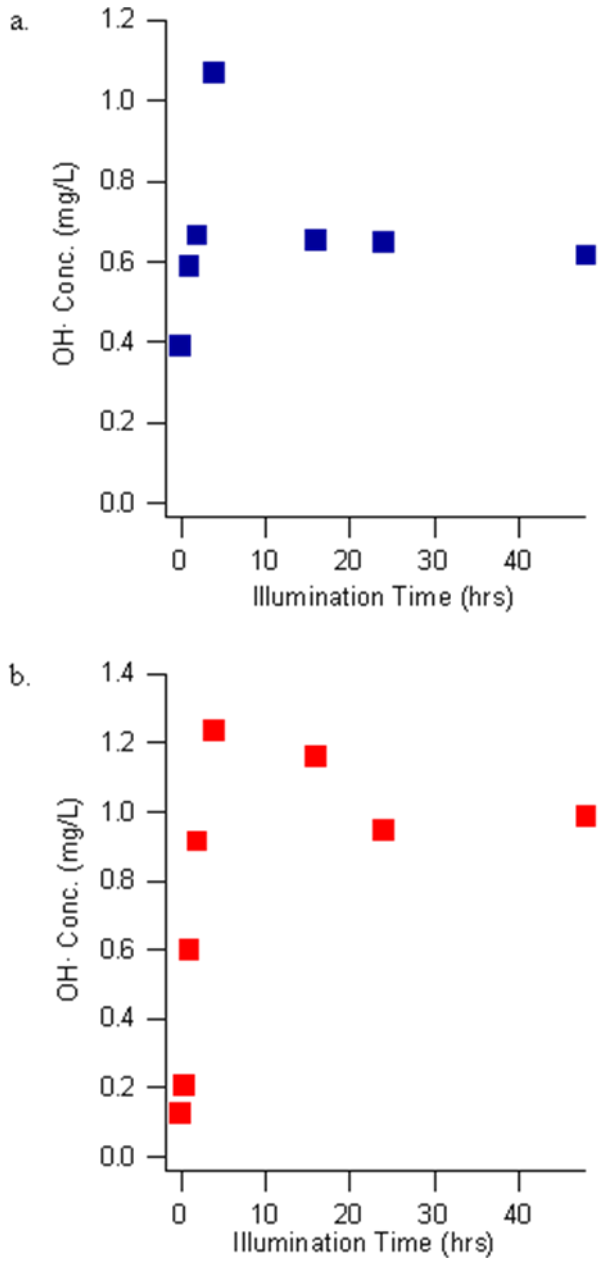

Figure 4.9: Time-dependent ROS generation of a) CuAAC modified TiO_2 nanoparticles and b) Thiol-ene modified TiO_2 nanoparticles. The hydroxyl radicals were detected by the APF fluorescent indicator.

4.3.4 Ligand Degradation after Light Exposure

The XPS multiplex data for the CuAAC nanoparticles was tracked for each of the 0, 0.5, 1, 2, 4, 8, 16, 24, and 48 hours of light exposure. Figure 4.10 shows the multiplex of the C (1s) for each of the time stamps of exposure. The spectra were corrected to have the C-C peak at 284.7 eV.(*45*) The oxidized carbon peaks are at 286.1 and 288.4 eV. The amount of oxidized carbon at 288.4 eV increases from 5.5% of the total carbon at zero hours of illumination to 17% after 48 hours.

Similarly the XPS multiplex data for the thiol-ene modified nanoparticles was tracked for the 0, 0.5, 1, 2, 4, and 7 hours of illumination. Figure 4.11 shows the multiplex of the C (1s) peak for each of the time stamps of exposure. Again the spectra were corrected to have the C-C peak at 284.7 eV and the oxidized carbon peaks occur at 286.1 and 288.4 eV. By 4 hours, a large increase in the oxidized peak at 288.4 eV has occurred.

Both types of "click" reaction modifications of the TiO_2 nanoparticles show oxidization of the ligands, although they are shown to produce only small amounts of hydroxyl radicals in Figure 4.8. Although the hydrophobic ligand attached directly to the surface of the nanoparticles might protect the TiO_2 surface from water and thus prohibiting the hole from oxidizing the water to hydroxyl radicals, dissolved oxygen is smaller and might be able to migrate to the surface and get reduced into the superoxide anion. Since the reduction reaction would be occurring, there must be oxidation. This could be a direct oxidation of the organic ligands by the hole of the TiO_2 as described by the photo-kolbe reaction.(*46, 47*) However, even though the ligands are being oxidized,

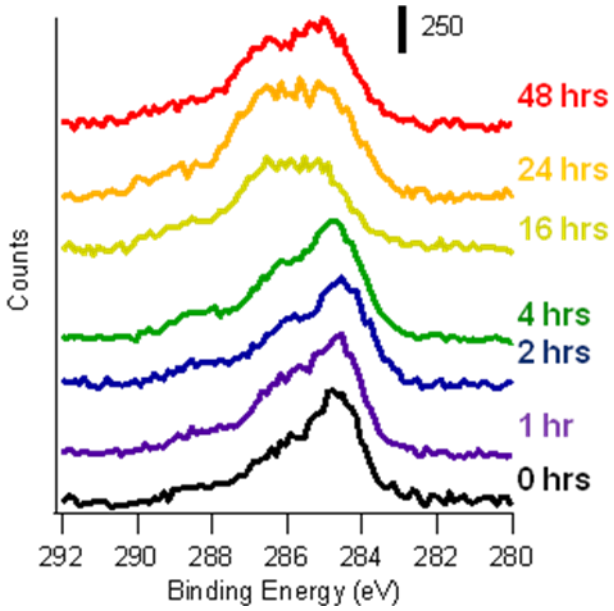

Figure 4.10: XPS spectra of the carbon (1s) peak of the CuAAC modified TiO_2 nanoparticles for the 0, 0.5, 1, 2, 4, 8, 16, 24, and 48 hours of light exposure. The oxidized carbon peaks occur at 286.1 and 288.4 eV.

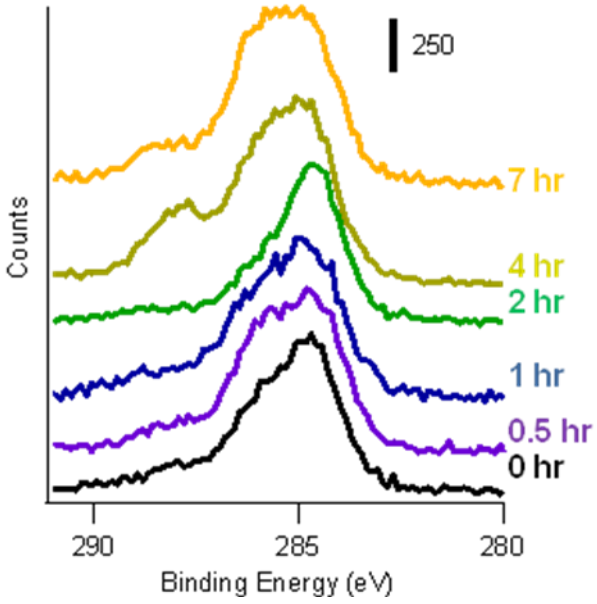

Figure 4.11: XPS spectra of the carbon (1s) peak of the thiol-ene modified TiO_2 nanoparticles for the 0, 0.5, 1, 2, 4, and 7 hours of light exposure. The oxidized carbon peaks occur at 286.1 and 288.4 eV.

after 48 hours of illumination there is still the same low steady-state production of hydroxyl radicals shown in Figure 4.9.

4.4 Conclusions

Surface functionalization of TiO_2 nanoparticles has shown to have a drastic effect on the amount of reactive oxygen species produced by the photo-activation of the nanoparticles. The CuAAC and thiol-ene "click" reactions have been successfully performed on the TiO_2 nanoparticle surfaces where the core is protected by a hydrophobic inner ligand. Compared to citrate coated nanoparticles and a complete hydrophilic PEG ligand, the "click" modified particles greatly reduce the amount of hydroxyl radicals detected after light exposure of the TiO_2. This reduction of detected ROS is sustained for at least 48 hours. Further studies can determine the long-term effects of direct hole oxidation of the ligands on ROS generation.

4.5 References

(1) Weir, A.; Westerhoff, P.; Fabricius, L.; Hristovski, K.; von Goetz, N. Titanium dioxide nanoparticles in food and personal care products. *Environmental Science & Technology* **2012**, *46*, 2242-50.

(2) Sanders, K.; Degn, L. L.; Mundy, W. R.; Zucker, R. M.; Dreher, K.; Zhao, B.; Roberts, J. E.; Boyes, W. K. In vitro phototoxicity and hazard identification of nano-scale titanium dioxide. *Toxicology and Applied Pharmacology* **2012**, *258*, 226-36.

(3) Nel, A.; Xia, T.; Mädler, L.; Li, N. Toxic potential of materials at the nanolevel. *Science* **2006**, *311*, 622-7.

(4) Teow, Y.; Asharani, P. V.; Hande, M. P.; Valiyaveettil, S. Health impact and safety of engineered nanomaterials. *Chemical Communications* **2011**, *47*, 7025-38.

(5) Turkez, H. The role of ascorbic acid on titanium dioxide-induced genetic damage assessed by the comet assay and cytogenetic tests. *Experimental and Toxicologic Pathology* **2011**, *63*, 453-7.

(6) Kiser, M. A.; Westerhoff, P.; Benn, T.; Wang, Y.; Pérez-Rivera, J.; Hristovski, K. Titanium nanomaterial removal and release from wastewater treatment plants. *Environmental Science & Technology* **2009**, *43*, 6757-63.

(7) Jones, C. F.; Grainger, D. W. In vitro assessments of nanomaterial toxicity. *Advanced Drug Delivery Reviews* **2009**, *61*, 438-56.

(8) Jiang, J.; Oberdörster, G.; Elder, A.; Gelein, R.; Mercer, P.; Biswas, P. Does nanoparticle activity depend upon size and crystal phase? *Nanotoxicology* **2008**, *2*, 33-42.

(9) Agency, U. S. E. P. External review draft nanomaterial case studies: Nanoscale titanium dioxide in water treatment and in topical sunscreen. **2009**.

(10) Berger, T.; Sterrer, M.; Diwald, O.; Knözinger, E.; Panayotov, D.; Thompson, T. L.; Yates, J. T. Light-induced charge separation in anatase TiO_2 particles. *The Journal of Physical Chemistry B* **2005**, *109*, 6061-8.

(11) Thompson, T. L.; Yates, J. T. Surface science studies of the photoactivation of TiO_2--new photochemical processes. *Chemical Reviews* **2006**, *106*, 4428-53.

(12) Linsebigler, A. L.; Lu, G.; Yates, J. T. Photocatalysis on TiO_2 surfaces: principles, mechanisms, and selected results. *Chemical Reviews* **1995**, *95*, 735-758.

(13) Satterfield, C. N. *Heterogeneous catalysis in inductrial practice*; 2nd ed.; McGraw-Hill: New York, 1991.

(14) Carp, O. Photoinduced reactivity of titanium dioxide. *Progress in Solid State Chemistry* **2004**, *32*, 33-177.

(15) Hagfeldt, A.; Graetzel, M. Light-induced redox reactions in nanocrystalline systems. *Chemical Reviews* **1995**, *95*, 49-68.

(16) Grassian, V. H. When size really matters: Size-dependent properties and surface chemistry of metal and metal oxide nanoparticles in gas and liquid phase environments. *Journal of Physical Chemistry C* **2008**, *112*, 18303-18313.

(17) Karlsson, H. L.; Gustafsson, J.; Cronholm, P.; Möller, L. Size-dependent toxicity of metal oxide particles--a comparison between nano- and micrometer size. *Toxicology Letters* **2009**, *188*, 112-8.

(18) Heinlaan, M.; Ivask, A.; Blinova, I.; Dubourguier, H.-C.; Kahru, A. Toxicity of nanosized and bulk ZnO, CuO and TiO_2 to bacteria *Vibrio fischeri* and crustaceans *Daphnia magna* and *Thamnocephalus platyurus*. *Chemosphere* **2008**, *71*, 1308-16.

(19) Fabian, E.; Landsiedel, R.; Ma-Hock, L.; Wiench, K.; Wohlleben, W.; van Ravenzwaay, B. Tissue distribution and toxicity of intravenously administered titanium dioxide nanoparticles in rats. *Archives of Toxicology* **2008**, *82*, 151-7.

(20) Ivask, A.; Bondarenko, O.; Jepihhina, N.; Kahru, A. Profiling of the reactive oxygen species-related ecotoxicity of CuO, ZnO, TiO_2, silver and fullerene nanoparticles using a set of recombinant luminescent *Escherichia coli* strains: differentiating the impact of particles and solubilised metals. *Analytical and Bioanalytical Chemistry* **2010**, *398*, 701-16.

(21) Warheit, D. B.; Hoke, R. a; Finlay, C.; Donner, E. M.; Reed, K. L.; Sayes, C. M. Development of a base set of toxicity tests using ultrafine TiO_2 particles as a component of nanoparticle risk management. *Toxicology Letters* **2007**, *171*, 99-110.

(22) Sayes, C. M.; Wahi, R.; Kurian, P. a; Liu, Y.; West, J. L.; Ausman, K. D.; Warheit, D. B.; Colvin, V. L. Correlating nanoscale titania structure with toxicity: a cytotoxicity and inflammatory response study with human dermal fibroblasts and human lung epithelial cells. *Toxicological Sciences* **2006**, *92*, 174-85.

(23) Wang, J.; Zhou, G.; Chen, C.; Yu, H.; Wang, T.; Ma, Y.; Jia, G.; Gao, Y.; Li, B.; Sun, J.; Li, Y.; Jiao, F.; Zhao, Y.; Chai, Z. Acute toxicity and biodistribution of different sized titanium dioxide particles in mice after oral administration. *Toxicology Letters* **2007**, *168*, 176-85.

(24) Chen, J.; Zhou, H.; Santulli, A. C.; Wong, S. S. Evaluating cytotoxicity and cellular uptake from the presence of variously processed TiO_2 nanostructured morphologies. *Chemical Research in Toxicology* **2010**, *23*, 871-9.

(25) Clemente, Z., Castro, V.L., Jonsson, C.M., et al. Ecotoxicology of nano-TiO_2: An evaluation of its toxicity to organisms of aquatic ecosystems. *International Journal of Environmental Research* **2012**, *6*, 33-50.

(26) Baccheta, R., Santo, N., Fascio, U., et al. Nano-sized CuO, TiO_2 and ZnO affect *Xenopus laevis* development. *Nanotoxicology* **2012**, *6*, 381-398.

(27) Bar-Ilan, O.; Louis, K. M.; Yang, S. P.; Pedersen, J. A; Hamers, R. J.; Peterson, R. E.; Heideman, W. Titanium dioxide nanoparticles produce phototoxicity in the developing zebrafish. *Nanotoxicology* **2011**, *Early Onli*, 1-10.

(28) Yang, H. W.; Hwang, K. J.; Kwon, H. C.; Kim, H. S.; Choi, K. W.; Oh, K. S. Detection of reactive oxygen species (ROS) and apoptosis in human fragmented embryos. *Human Reproduction* **1998**, *13*, 998-1002.

(29) Dunford, R.; Salinaro, A.; Cai, L.; Serpone, N.; Horikoshi, S.; Hidaka, H.; Knowland, J. Chemical oxidation and DNA damage catalysed by inorganic sunscreen ingredients. *FEBS Letters* **1997**, *418*, 87-90.

(30) Kolb, H. C.; Finn, M. G.; Sharpless, K. B. Click chemistry: Diverse chemical function from a few good reactions. *Angewandte Chemie* **2001**, *40*, 2004-2021.

(31) Rostovtsev, V. V.; Green, L. G.; Fokin, V. V.; Sharpless, K. B. A stepwise huisgen cycloaddition process: copper(I)-catalyzed regioselective "ligation" of azides and terminal alkynes. *Angewandte Chemie* **2002**, *41*, 2596-9.

(32) Collman, J. P.; Devaraj, N. K.; Chidsey, C. E. D. "Clicking" functionality onto electrode surfaces. *Langmuir* **2004**, *20*, 1051-3.

(33) Ciampi, S.; Böcking, T.; Kilian, K. A; James, M.; Harper, J. B.; Gooding, J. J. Functionalization of acetylene-terminated monolayers on Si(100) surfaces: A Click chemistry approach. *Langmuir* **2007**, *23*, 9320-9.

(34) Rohde, R. D.; Agnew, H. D.; Yeo, W. S; Bailey, R. C.; Heath, J. R. A Non-oxidative approach toward chemically and electrochemically functionalizing Si(111). *Journal of the American Chemical Society* **2006**, 9518-9525.

(35) Shah, S.; Benson, M. C.; Bishop, L. M.; Huhn, A. M.; Ruther, R. E.; Yeager, J. C.; Louis, M.; Hamers, R. J. Chemically assembled heterojunctions of SnO_2 nanorods with TiO_2 nanoparticles via "click" chemistry. *Journal of Materials Chemistry* **2012**, *accepted*.

(36) Landis, E. C.; Hamers, R. J. Covalent grafting of redox-active molecules to vertically aligned carbon nanofiber arrays via " click " chemistry. *Chemistry of Materials* **2009**, *21*, 724-730.

(37) Santore, R. C.; Di Toro, D. M.; Paquin, P. R.; Allen, H. E.; Meyer, J. S. Biotic ligand model of acute toxicity in metals. 2. Application to acute copper toxicity in freshwater fish and *Daphnia*. *Environmental Toxicology and Chemistry* **2001**, *20*, 2397-2402.

(38) Tasdelen, M. A.; Yagci, Y. Light-induced copper(I)-catalyzed click chemistry. *Tetrahedron Letters* **2010**, *51*, 6945-6947.

(39) Limapichat, W.; Basu, A. Reagentless functionalization of gold nanoparticles via a 3 + 2 Huisgen cycloaddition. *Journal of Colloid and Interface Science* **2008**, *318*, 140-4.

(40) Li, G.-Z.; Randev, R. K.; Soeriyadi, A. H.; Rees, G.; Boyer, C.; Tong, Z.; Davis, T. P.; Becer, C. R.; Haddleton, D. M. Investigation into thiol-(meth)acrylate Michael addition reactions using amine and phosphine catalysts. *Polymer Chemistry* **2010**, *1*, 1196.

(41) Kumari, S.; Malvi, B.; Ganai, A. K.; Pillai, V. K.; Gupta, S. S. Functionalization of SBA-15 mesoporous materials using "thiol-ene click" Michael Addition reaction. *Journal of Physical Chemistry C* **2011**, *115*, 17774-17781.

(42) Kotsokechagia, T.; Cellesi, F.; Thomas, A.; Niederberger, M.; Tirelli, N. Preparation of ligand-free TiO_2 (anatase) nanoparticles through a nonaqueous process and their surface functionalization. *Langmuir* **2008**, *24*, 6988-97.

(43) Cohn, C. a; Simon, S. R.; Schoonen, M. A. Comparison of fluorescence-based techniques for the quantification of particle-induced hydroxyl radicals. *Particle and Fibre Toxicology* **2008**, *5*, 2.

(44) Cohn, C. a; Pedigo, C. E.; Hylton, S. N.; Simon, S. R.; Schoonen, M. Evaluating the use of 3'-(p-Aminophenyl) fluorescein for determining the formation of highly reactive oxygen species in particle suspensions. *Geochemical Transactions* **2009**, *10*, 8.

(45) Powell, C. J. Quantitative surface analysis by X-ray photoelectron spectroscopy. *Applications of Surface Science* **1978**, *1*, 186-201.

(46) Yang, D.; Ni, X.; Chen, W.; Weng, Z. The observation of photo-Kolbe reaction as a novel pathway to initiate photocatalytic polymerization over oxide semiconductor nanoparticles. *Journal of Photochemistry and Photobiology A: Chemistry* **2008**, *195*, 323-329.

(47) Mao, Y.; Schoneich, C.; Asmus, K.-dieter Identification of organic acids and other intermediates in oxidative degradation of chlorinated ethanes on TiO_2, surfaces en route to mineralization. A combined photocatalytic and radiation chemical study. *Journal of Physical Chemistry* **1991**, *95*, 10080-10089.

Chapter 5

Density Functional Theory Computations of Geometry Optimization and Stability of Molecules Adsorbed onto Metal Oxide Surfaces

5.1 Introduction

5.1.1 Density Functional Theory *(1)*

Density Functional Theory (DFT) is a quantum mechanical modeling method used to determine the electronic structure of many-body systems. DFT utilizes functionals (functions where the variables themselves are functions) to determine the properties of the system, specifically the spatially dependent electron density. DFT models date back to the 1970s, however, they were not considered accurate enough for useful predictions until the 1990s when the approximations were refined to include exchange and correlation interactions. For Kohn-Sham DFT, the interacting electrons in a static external potential are reduced to a tractable problem of non-interacting electrons moving in an effective potential which includes the effects of Coulomb interactions between the electrons. To find the ground state of a system using DFT, the Kohn-Sham equations are solved self-consistently

$$\left(T + V + V_H(n) + V_{xc}(n)\right)\varphi_i = \epsilon_i \varphi_i$$

where T is the kinetic energy, V is the potential energy from the external field due to positively charged nuclei, V_H is the Hartree energy, V_{xc} is the exchange-correlation potential, φ_i is the Kohn-Sham orbital, and ε_i is the orbital energy.

The charge density is described by

$$n(r) = \sum_i f_i |\varphi_i(r)|^2$$

where i is the combined k and band index, f_i is the occupancy of states, and orthonormality constraints $\langle \varphi_i | \varphi_j \rangle = \delta_{ij}$.

Although DFT correlates nicely to experiments for ground state energy calculations, there are still difficulties in using the model to describe intermolecular interactions, charge transfer excitations, transition states, global potential energy surfaces, and band gap calculations for semiconductors.

5.1.2 Plane-wave Pseudopotential Methods *(1, 2)*

Many-electron calculations can be very expensive as the computation time increases drastically the number of electrons. The cost of the computation describes the length of time it takes for the job to finish. Since surface calculations require not only the use of many atoms to create a sufficient slab of both surface and "bulk" atoms but also the metal oxide semiconductors contain heavy metal atoms with many electrons. However, the electrons can be divided into valence electrons and inner core electrons.

The inner core electrons are strongly bound to the nucleus and do not play a significant role in the bonding of atoms. A pseudopotential method uses an effective potential where the valence electrons are treated explicitly while the core electrons are "frozen" and considered together with the nuclei as rigid, non-polarizable ion cores. Early empirical pseudopotentials were designed by fitting computational results to some known experimental data such as band gaps or ionization potentials. Norm-conserving pseudopotentials are used to describe electronic-ionic core interactions where the pseudo-wavefunctions contain no "orthonormality wiggles."

In solid state calculations, the local density approximations (where the functional depends only on the density at the coordinate where the functional is evaluated) are commonly used along with plane wave basis sets, as an electron gas approach is more appropriate for electrons delocalized through an infinite solid.

In molecular calculations, however, more sophisticated functionals are needed, and a number of exchange-correlation functionals have been developed for chemical applications. One of the most widely used functional is the revised Perdew–Burke–Ernzerhof exchange model (a direct generalized-gradient parametrization of the free electron gas).

5.1.3 VASP Computational Software

VASP (Vienna Ab-Initio Simulation Package) is a computational program developed by Georg Kresse, Martijn Marsman, and Jürgen Furthmüller at the Universität Wien in Vienna, Austria (for VASP references see section 5.6). VASP uses pseudopotentials and periodic systems. Periodic systems are described as a unit cell

repeated to form an infinite system. Periodicity can be in one, two, or three dimensions. Examples are a polymer (one dimension), a surface (two dimensions), and a crystal (three dimensions). For this research, two dimensions are used to create a surface. The unit cell is described by three vectors **a**, **b**, and **c** and the angles between them.

VASP has four input files necessary to run a job: INCAR, KPOINTS, POSCAR, and POTCAR. These files provide the information inherent to specific system as well as the computational details. The INCAR file is the central input file that contains the parameters for what the computation needs to do and how it should do it. These include whether to start a new job or continue from a previous job, number of bands, charges, precision of the calculation, energy difference stopping criterion for electronic self-consistent loop, number of maximum ionic steps, ionic relaxation, and electron smearing. The KPOINTS file contains the k-point mesh size for creating a k-point grid or explicitly contains the k-point coordinates and weights. The POSCAR file includes the lattice geometry and ionic positions. The POTCAR file contains the pseudopotential for each atomic species used in the calculations.

Once a computation has started using VASP, a number of output files are created where each one stores specific information. The IBZKPT file generates the automatic k-mesh from the KPOINTS file. This is important because once this file is constructed it can be used for further computations eliminating the need to recalculate the k-mesh. The CONTCAR file stores the atom positions after each ionic step of the calculation and is formatted in the same fashion as the POSCAR file. The CHGCAR file contains information about the charge densities and can be used to restart VASP from an existing

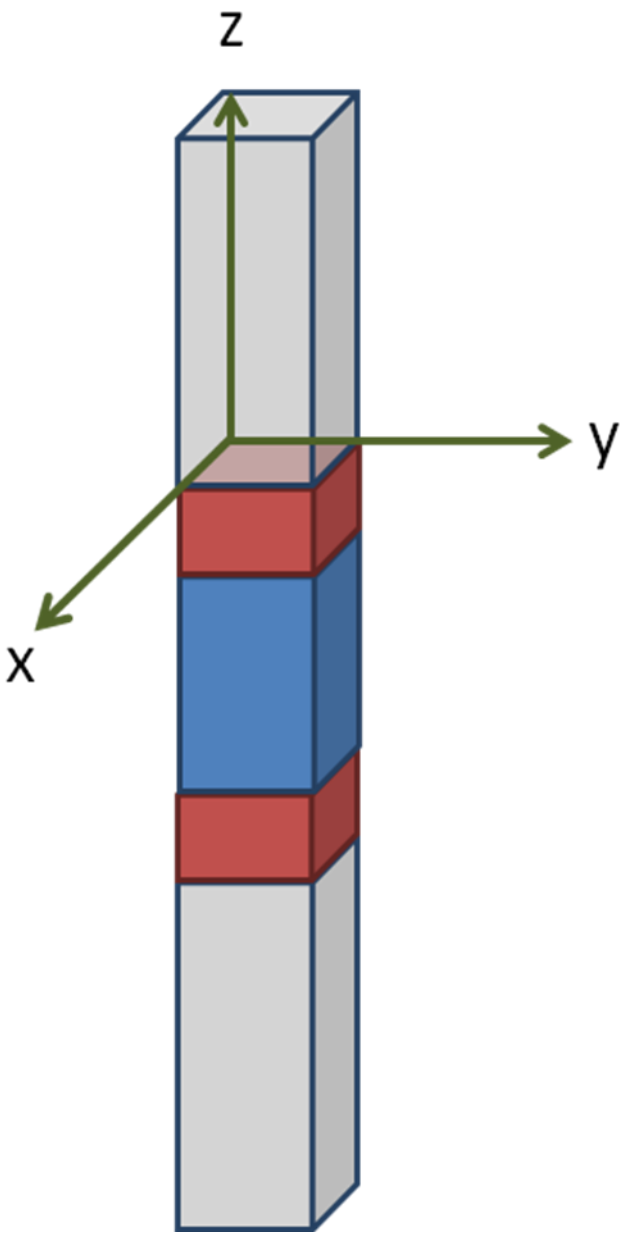

Figure 5.1: Slab geometry used for computations of surfaces. Red indicates surface atoms, blue represents bulk atoms and grey is the vacuum space between slabs. Periodic systems are created by the lattice vectors in the x, y, and z directions.

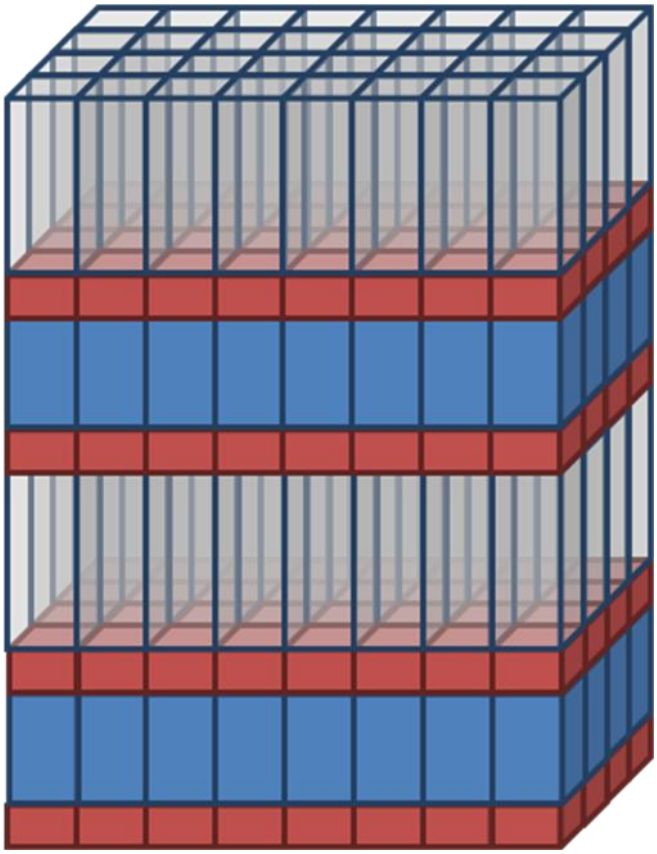

Figure 5.2: Slab geometry used for computations of surfaces. Red indicates surface atoms, blue represents bulk atoms and grey is the vacuum space between slabs. Periodic systems are created by the lattice vectors in the x, y, and z directions.

charge density. The WAVECAR file stores the wavefunctions, the EIGENVALUE file contains the Kohn-Sham-eigenvalues for all k-points, at the end of the simulation, the DOSCAR file contains the DOS and integrated DOS, and the PROCAR contains the spd- and site projected wave function character of each band. The OUTCAR file contains the k-mesh, charges, atom positions, and total energy for each of the ionic steps. Together these files define the geometry optimization and ground state energy of the periodic system.

5.1.4 Metal Oxide Surfaces

Previous chapters have given in-depth introductions of TiO_2 and its wide-spread use in societal applications. However, many metal oxides are also prevalent in applications including catalysis, sensors, electronic materials, and environmental remediation.(*3*)

A number of well-known theoretical and computational scientists have examined in-depth the first-principles of the structure and energetics of many metal oxide surfaces as well as reactivities, predicting vibrational frequencies, defects, ligand binding geometries, and many other properties.(*4–31*) These studies have given insight into the experimental work of their coworkers and a more solid understanding of the crystalline structures at the molecular scale.

For these calculations, a flat surface is created using the "slab geometry." Although many of these studies are compared to experimental data on colloidal or thin film nanoparticles, once the nanoparticles reach a certain size, the curvature of the surface can be represented by a flat geometry.

5.2 Adsorption of Various Anchoring Groups onto Anatase (001) TiO_2 Surface

5.2.1 VASP Computational Method

For TiO_2 slab, the surface was the (001) face of the anatase phase which is the most reactive but not the most prevalent face. For the simulations of a monolayer, the TiO_2 slab consisted of 24 atoms and had lattice vectors of 3.7842 x 3.7842 x 50 angstroms. To create a half-monolayer, the TiO_2 slab was doubled consisting of 48 atoms with lattice vectors of 3.7842 x 7.5684 x 50 Å. The lattice vector of 50 angstroms created the vacuum space between the surface slabs. All simulations used a 6 x 6 x 1 k-point mesh that was gamma centered. The molecules were adsorbed to both sides of the slab and during the structural optimizations the adsorbates and all atoms of the slab were allowed to move. An energy cutoff of 400.0 eV and an energy difference of 1E-4 were used. The tetrahedron method with Block corrections was used for electron smearing. All calculations were performed using the Perdew-Burke-Ernzerhof (PBE) exchange correlation functional.

The bare surface of TiO_2 and each of the anchoring ligands were structurally optimized using the same conditions as the functionalized surfaces. Any additional products necessary to balance the chemical equations were also optimized. The anchoring groups examined were an alcohol, aldehyde, carboxylate, and hydroxamate. Each of the molecules had four carbon atoms. The carboxylate was examined using monodentate ether, bidentate bridging, and bidentate chelating conformations. The hydroxamate molecule was simulated with bidentate bridging and bidentate chelating conformations.

5.2.2 Results

The relative stability of the different ligands on the surface of (001) anatase TiO_2 is determined using the functionalization energy given as

$$E_{func} = \frac{1}{A}\left(E_T^{func} - E_T^{surf} - N\mu\right)$$

where A is the surface area of the slab, E_T^{func} is the total energy of the functionalized surface, E_T^{surf} is the total energy of the bare surface, and μ is the chemical potential (or total energy) of the adsorbed molecule, and N is the number of molecules adsorbed to the surface. The adsorption phase diagram can be plotted in terms of the adsorbed molecule concentration by representing the chemical potential by

$$\mu = \mu_0 + \Delta\mu = \mu_0 + RT \ln P(atm)$$

where the variational parameter $\Delta\mu$ accounts for the range of chemical potentials that occur during experimental conditions. The functionalization energy per unit area versus $\Delta\mu$ is graphed in Figure 5.3. For comparison, the functionalizations that have the highest stability will have the lowest functionalization energies.

From this data, the alcohol and aldehyde have the weakest functionalization energies and in most cases the geometry optimizations did not keep the molecules anchored to the surface. The greatest stabilities were found for carboxylate and

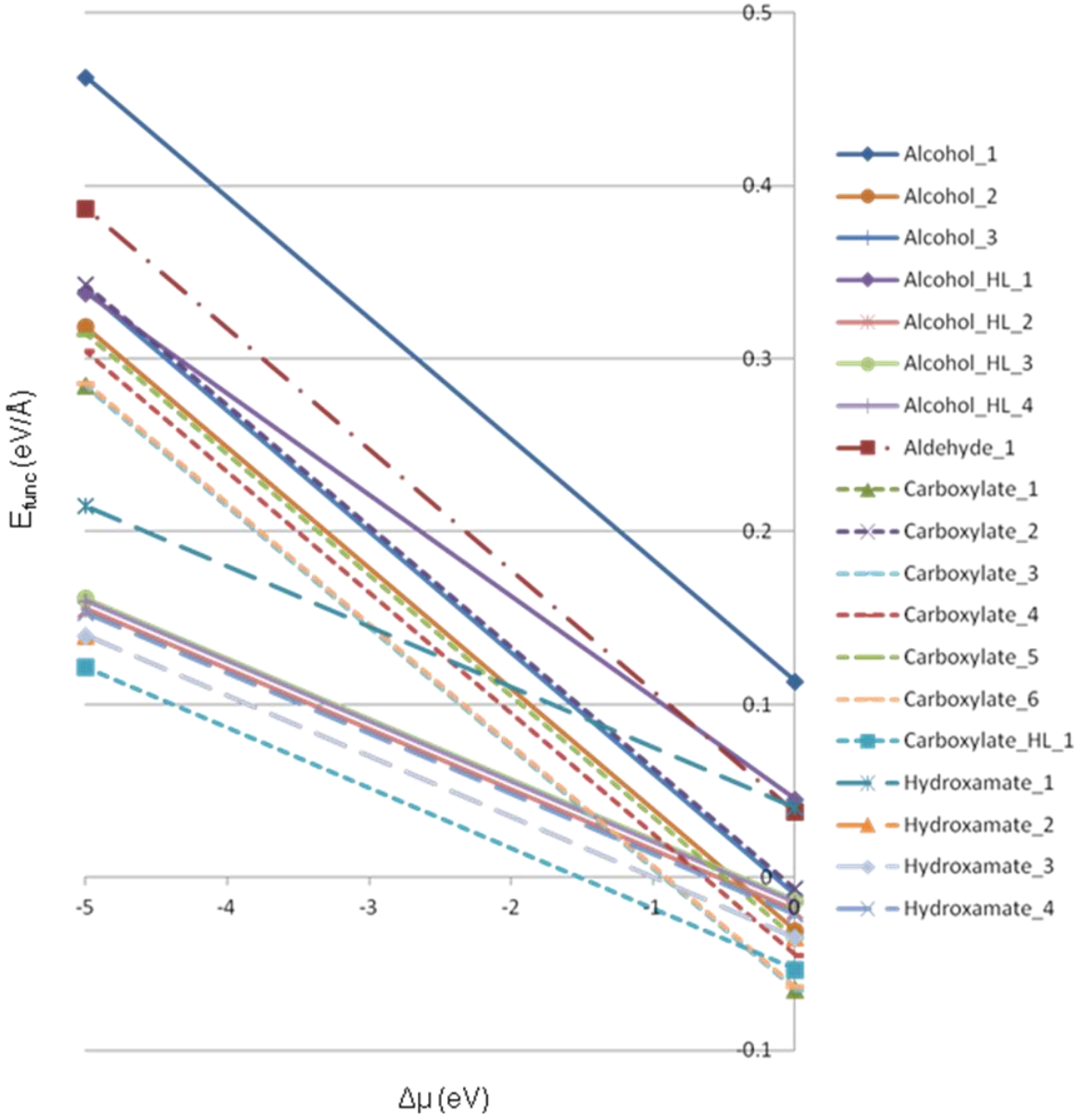

Figure 5.3: Functionalization energies per unit area versus chemical potential for the different molecular anchoring groups on an anatase (001) surface. For each chemical potential, the lower the energy of the functionalization the more stable the molecule on the surface is.

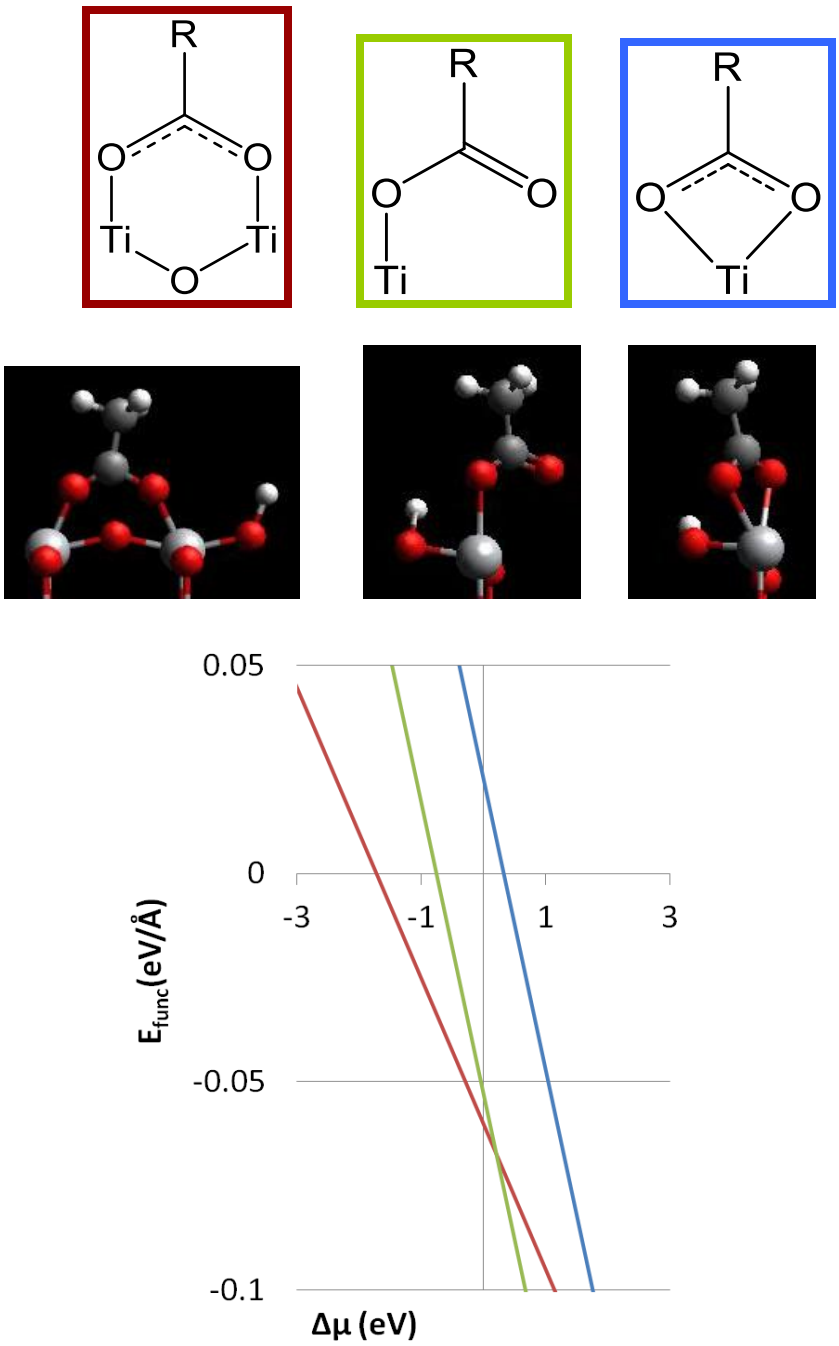

Figure 5.4: Functionalization energies per unit area versus chemical potential for the different binding modes of a carboxylate molecule on an anatase (001) surface. Red indicates a bidentate bridging mode, green indicates a monodentate ether mode, and blue indicates a bidentate chelating mode.

hydroxymate anchoring groups. A more in depth comparison was done with the carboxylate groups in terms of the different binding modes shown in Figure 5.4: bidentate bridging, monodentate ether, and bidentate chelating. In Figure 5.4 the graph of the functionalization energies versus chemical potential is given for each of the binding modes for $\Delta\mu$ = -3 to 3 eV. For negative chemical potentials, the bidentate bridging conformation is the most stable. This can be attributed to solution phase conditions were the concentrations of the adsorbing molecules are lower giving rise to a half- monolayer coverage. When the adsorbing molecule concentrations are higher, where $\Delta\mu$ is greater than about 0.2, the monodentate ether binding mode is most stable. Under all conditions, the bidentate chelating conformation is never the most stable.

5.3 Comparison of Covalent Bonding of Ligand to Various Metal Oxide Surfaces through a Williamson-Ether Type Reaction

5.3.1 VASP Computational Method

For this study, a three different metal oxide surfaces were compared: TiO_2, ZnO, and SnO_2. The reaction scheme being modeled is shown in Figure 5.5. There are a number of possibilities for the binding of the molecule to the surface; two of the simulated possibilities are displayed where under heated conditions the alkyl attaches to the surface through either a surface oxygen atom or the hydroxyl group of a surface metal atom. For these simulations the water and heated temperatures are not taken into consideration, therefore, the byproducts of the reactions are unknown. For comparison the byproduct is kept the same as HI.

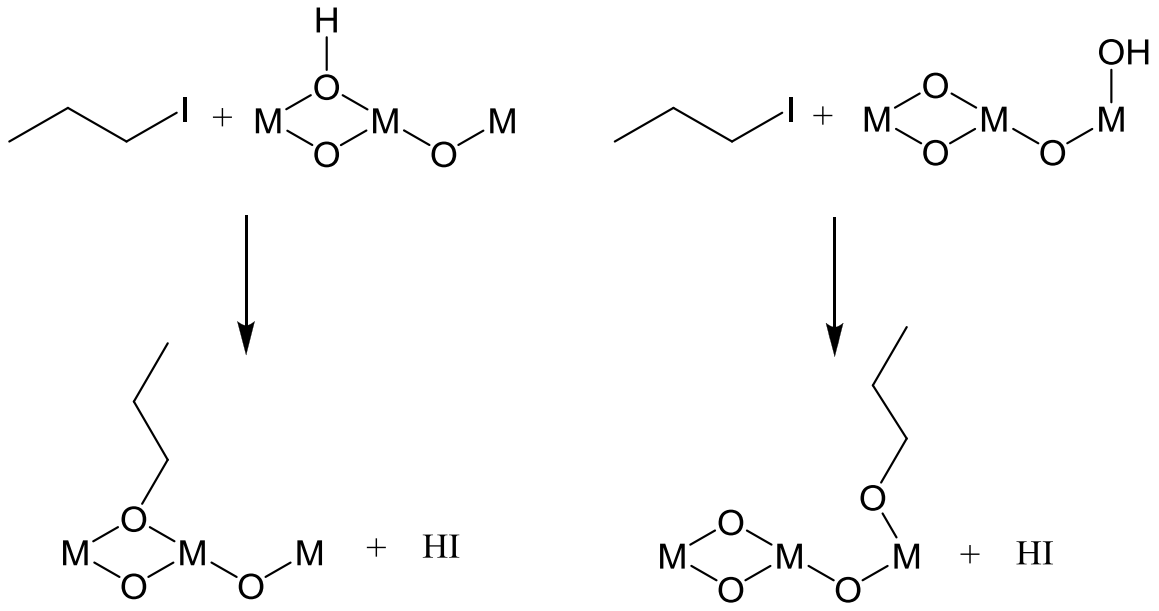

Figure 5.5: Two examples of the Williamson-ether type reaction of an iodo-alkane binding to the surface of a metal oxide (M denotes metal). A covalent attachment can be made through a surface oxygen or the oxygen of a hydroxylated metal surface atom.

For TiO_2, the surface was the (001) face of the anatase phase which is the most reactive but not the most prevalent face. The slab consisted of 24 atoms with lattice vectors of 3.7842 x 3.7842 x 50 Å. The 50 Å lattice vector created the vacuum space between the surface slabs. All simulations used a 6 x 6 x 1 k-point mesh that was gamma centered.

ZnO was simulated using the (10-10) hexagonal face of the wurzite phase. This is a non-polar face with both Zn and O atoms present at the surface. The ZnO slab consisted of 32 atoms with lattice vectors of 50 x 3.2828 x 5.2597 Å where the 50 Å lattice vector created the vacuum space between surfaces. The simulations used a 1 x 8 x 8 k-point mesh that was gamma centered.

SnO_2 was modeled using the (110) face of the rutile phase. This is the most prominate face of the rutile phase and is often used for simulations. The SnO_2 slab consisted of 30 atoms with lattice vectors of 6.7010 x 50 x 3.1865 Å where the 50 Å lattice vector created the vacuum space between surfaces. The simulations used a 12 x 1 x 12 k-point mesh that was gamma centered.

All calculations used an energy cutoff of 400.0 eV and an energy difference of 1E-4. The tetrahedron method with Block corrections was used for electron smearing. All calculations were performed using the Perdew-Burke-Ernzerhof (PBE) exchange correlation functional. The molecules were adsorbed to both sides of each of the metal oxide slabs and all atoms were allowed to geometry optimize.

The bare surface and hydroxylated surfaces of each of the metal oxides and the anchoring ligand were structurally optimized using the same conditions as the

Simulation	E_{func}(eV)	Attached?
Anatase		
1	-0.26	yes
2	-0.27	no
3	-0.02	no
4	-0.65	no
5	-0.28	yes
6	-0.35	yes
7	-0.32	no
8	-0.33	yes
ZnO		
1	0.01	no
2	0.02	yes/no
3	0.08	yes
4	-0.28	yes
5	0.35	yes
6	-0.02	yes
SnO_2		
1	-0.37	yes
2	-0.30	yes
3	-0.34	yes
4	-0.32	yes
5	-0.39	yes
6	-0.36	yes

Table 5.1: Functionalization energies of the Williamson-ether type covalent linkage to each of the surfaces. The first column indicates the simulation number (structures shown in Figures 5.7, 5.8, and 5.9), the second column is the functionalization energies, and the third column indicates whether the molecule remained on the surface after optimization.

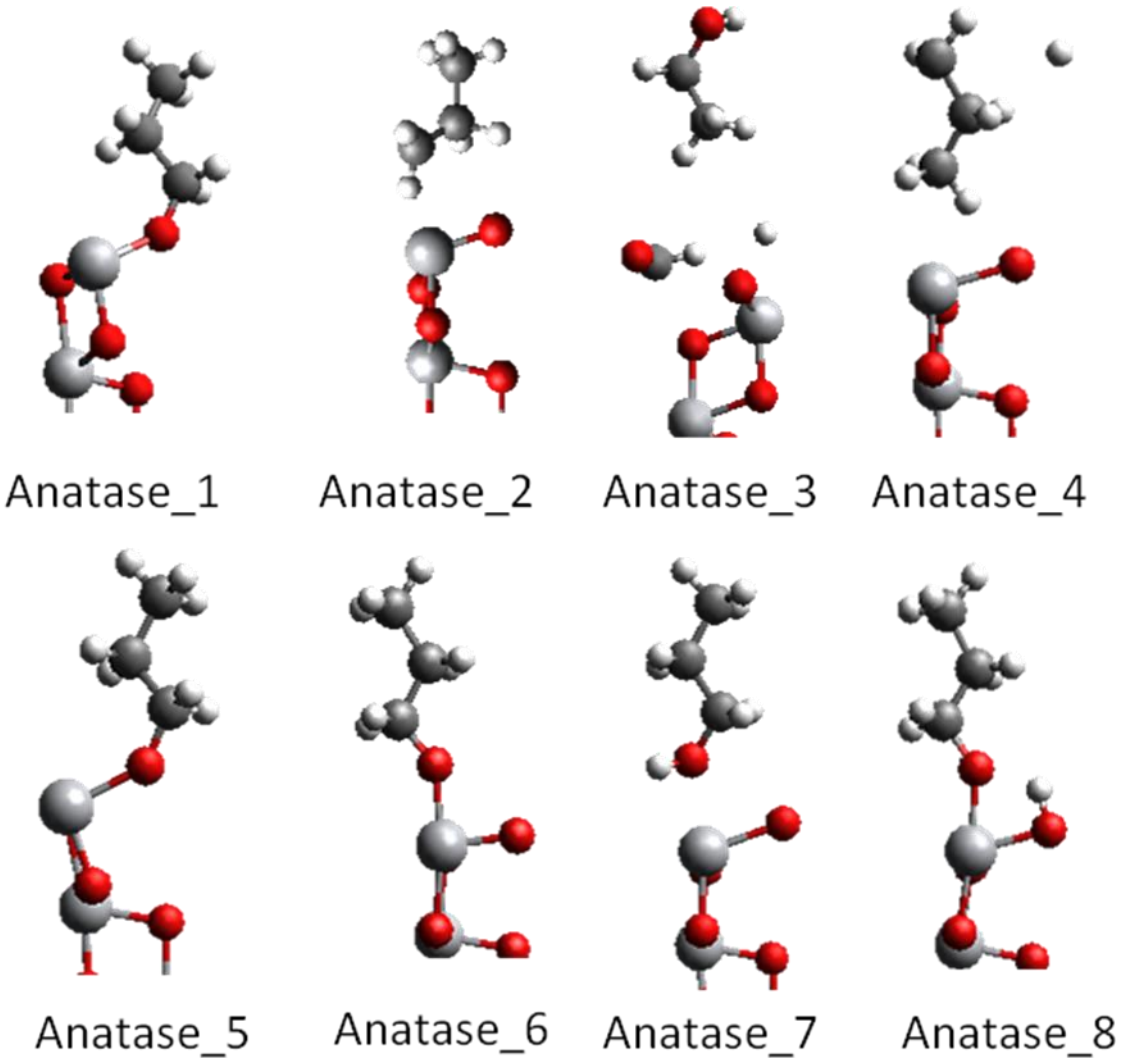

Figure 5.7: Images of the geometry optimizations of the eight simulations performed on the surface of anatase (001) TiO_2. Only one of the surfaces for each slab is shown for simplicity.

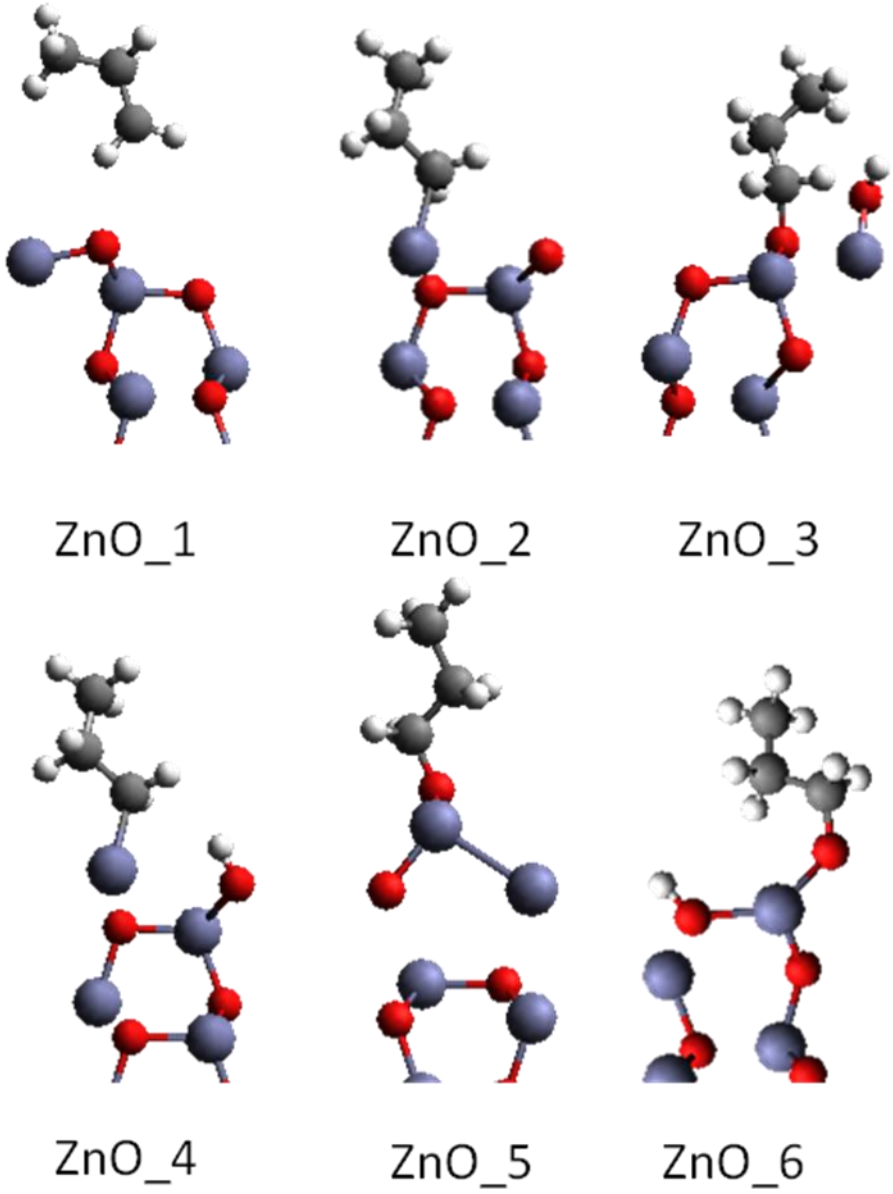

Figure 5.8: Images of the geometry optimizations of the eight simulations performed on the surface of wurtzite (10-10) ZnO. Only one of the surfaces for each slab is shown for simplicity.

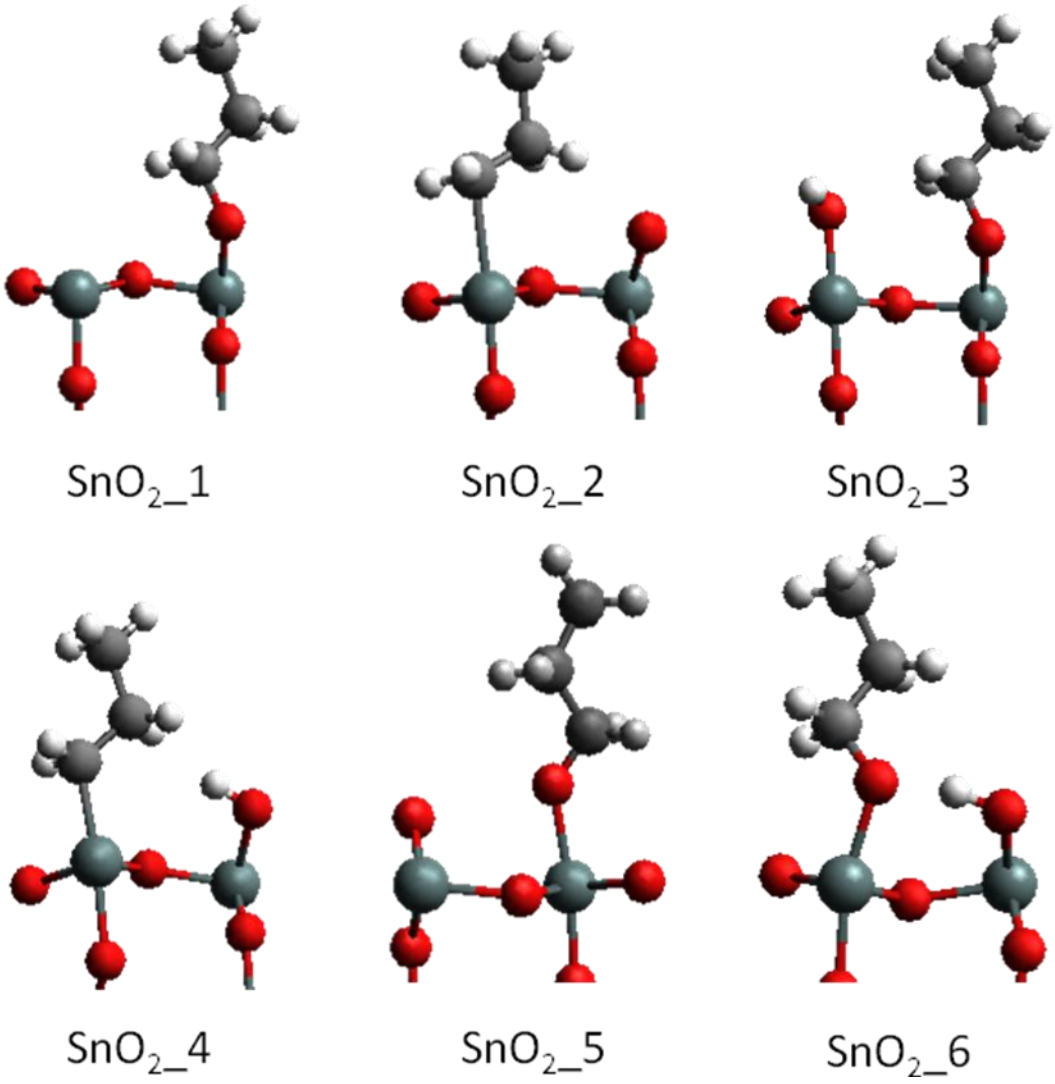

Figure 5.9: Images of the geometry optimizations of the eight simulations performed on the surface of rutile (110) SnO_2. Only one of the surfaces for each slab is shown for simplicity.

functionalized surfaces. Any byproducts necessary to balance the chemical equations were also optimized.

5.3.2 Results

The relative stability of the ligand on the surfaces of anatase TiO_2, ZnO, and SnO_2 is determined using the functionalization energy given as the equation in section 5.2.2.

The results of the simulated functionalization energies per unit area are displayed in Table 5.1. The table also indicates whether the molecules remained attached to the surface after the geometry optimization. The corresponding images are shown in Figures 5.7, 5.8, and 5.9 where only one of the sides of the slab is shown for simplicity. A direct comparison can be made between the metal oxide surfaces since the HI byproduct is kept constant even though there is no addition of water into the simulation. From this data, it appears the molecular linkage can be relatively stable on all three surfaces, with SnO_2 showing the most stabile attachments and ZnO showing the least stabile attachments. The molecule on anatase TiO_2 has the strongest functionalization energy when attached to the hydroxyl oxygen bound to a Ti atom of the surface (simulations 6 and 8).

5.4 Conclusions

The simulation results of this study can be used for comparisons with experimental work on the functionalization of various metal oxide surfaces. When comparing a variety of surface anchoring groups on anatase (001) TiO_2, carboxylate linkages were the most stabile and depending on the concentration of the molecule, the binding mode is either bidentate bridging or monodentate ether.

Experimental work in the Hamers group has concentrated on a Williamson-ether type reaction of the surfaces of metal oxides with iodo-alkane groups.(*32*) When comparing the stability of the covalent organic linkage to TiO_2, ZnO, and SnO_2, the stability appears to be strongest for SnO_2 then TiO_2 then ZnO. These computations can be used to help elucidate a mechanism of binding as well as help determine if a reaction should take place experimentally.

5.5 References

(1) Jensen, F. *Introduction to Computational Chemistry*; 2nd ed.; Wiley: West Sussex, England, 2007.

(2) Meyer, B. The Pseudopotential plane wave approach. *Computational Nanoscience: Do It Yourself!* **2006**, *31*, 71-83.

(3) Oskam, G. Metal oxide nanoparticles: Synthesis , characterization and application. *Journal of Sol-Gel Science Technology* **2006**, *37*, 161-164.

(4) Aschauer, U.; Chen, J.; Selloni, A. Peroxide and superoxide states of adsorbed O(2) on anatase TiO(2) (101) with subsurface defects. *Physical Chemistry Chemical Physics* **2010**, *12*, 12956-60.

(5) Aschauer, U.; He, Y.; Cheng, H.; Li, S.-C.; Diebold, U.; Selloni, A. Influence of subsurface defects on the surface reactivity of TiO_2: Water on anatase (101). *The Journal of Physical Chemistry C* **2010**, *114*, 1278-1284.

(6) Bredow, T. Theoretical investigation of water adsorption at rutile and anatase surfaces. *Surface Science* **1995**, *327*, 398-408.

(7) Burello, E.; Worth, A. P. A theoretical framework for predicting the oxidative stress potential of oxide nanoparticles. *Nanotoxicology* **2011**, *5*, 228-35.

(8) Cheng, H.; Selloni, A. Hydroxide ions at the water/anatase TiO_2(101) interface: Structure and electronic states from first principles molecular dynamics. *Langmuir* **2010**, *26*, 11518-25.

(9) Cheng, H.; Selloni, A. Energetics and diffusion of intrinsic surface and subsurface defects on anatase TiO_2(101). *The Journal of Chemical Physics* **2009**, *131*, 054703.

(10) De Angelis, F.; Fantacci, S.; Selloni, A.; Nazeeruddin, M. K.; Grätzel, M. First-principles modeling of the adsorption geometry and electronic structure of Ru(II) dyes on extended TiO_2 substrates for dye-sensitized solar cell applications. *The Journal of Physical Chemistry C* **2010**, *114*, 6054-6061.

(11) Deskins, N. A.; Rousseau, R.; Dupuis, M. Localized electronic states from surface hydroxyls and polarons in TiO_2 (110). *The Journal of Physical Chemistry C* **2009**, *113*, 14583-14586.

(12) Deskins, N. A.; Kerisit, S.; Rosso, K. M.; Dupuis, M. Molecular dynamics characterization of rutile-anatase interfaces. *Journal of Physical Chemistry C* **2007**, *111*, 9290-9298.

(13) Di Valentin, C.; Pacchioni, G.; Selloni, A. Reduced and n-type doped TiO_2: Nature of Ti 3+ species. *The Journal of Physical Chemistry C* **2009**, *113*, 20543-20552.

(14) Finazzi, E.; Di Valentin, C.; Pacchioni, G.; Selloni, A. Excess electron states in reduced bulk anatase TiO2: comparison of standard GGA, GGA+U, and hybrid DFT calculations. *The Journal of Chemical Physics* **2008**, *129*, 154113.

(15) Greuling, A.; Rahe, P.; Kaczmarski, M.; Kühnle, A.; Rohlfing, M. Combined NC-AFM and DFT study of the adsorption geometry of trimesic acid on rutile TiO_2 (110). *Journal of Physics: Condensed Matter* **2010**, *22*, 345008.

(16) Jonsson, C. M.; Jonsson, C. L.; Estrada, C.; Sverjensky, D. a.; Cleaves II, H. J.; Hazen, R. M. Adsorption of l-aspartate to rutile (α-TiO_2): Experimental and theoretical surface complexation studies. *Geochimica et Cosmochimica Acta* **2010**, *74*, 2356-2367.

(17) Lany, S. Semiconductor thermochemistry in density functional calculations. *Physical Review B* **2008**, *78*, 1-8.

(18) Lany, S.; Zunger, A. Accurate prediction of defect properties in density functional supercell calculations. *Modelling and Simulation in Materials Science and Engineering* **2009**, *17*, 084002.

(19) Lany, S.; Zunger, A. Many-body GW calculation of the oxygen vacancy in ZnO. *Physical Review B* **2010**, *81*.

(20) Lazzeri, M.; Vittadini, A.; Selloni, A. Structure and energetics of stoichiometric TiO_2 anatase surfaces. *Physical Review B* **2001**, *63*, 1-9.

(21) Li, W.-K.; Gong, X.-Q.; Lu, G.; Selloni, A. Different reactivities of TiO_2 polymorphs: Comparative DFT calculations of water and formic acid adsorption at anatase and brookite TiO_2 surfaces. *Journal of Physical Chemistry C* **2008**, *112*, 6594-6596.

(22) Mcnamara, W. R.; Milot, R. L.; Song, H.-eun; Iii, R. C. S.; Batista, V. S.; Schmuttenmaer, C. A.; Brudvig, G. W.; Crabtree, R. H. Water-stable , hydroxamate anchors for functionalization of TiO_2 surfaces with ultrafast interfacial electron transfer. *Energy & Environmental Science* **2010**, *3*, 917-923.

(23) Mendive, C. B.; Bredow, T.; Feldhoff, A.; Blesa, M. a; Bahnemann, D. Adsorption of oxalate on anatase (100) and rutile (110) surfaces in aqueous systems: Experimental results vs. theoretical predictions. *Physical Chemistry Chemical Physics* **2009**, *11*, 1794-808.

(24) Ménétrey, M.; Markovits, A.; Minot, C.; Pacchioni, G. Formation of Schottky defects at the surface of MgO, TiO_2, and SnO_2: A Comparative density functional theoretical study. *The Journal of Physical Chemistry B* **2004**, *108*, 12858-12864.

(25) Pacchioni, G. Oxygen vacancy: the invisible agent on oxide surfaces. *Chemphyschem* **2003**, *4*, 1041-7.

(26) Pacchioni, G. Modeling doped and defective oxides in catalysis with density functional theory methods: room for improvements. *The Journal of Chemical Physics* **2008**, *128*, 182505.

(27) Panagiotou, G. D.; Petsi, T.; Bourikas, K.; Garoufalis, C. S.; Tsevis, A.; Spanos, N.; Kordulis, C.; Lycourghiotis, A. Mapping the surface (hydr)oxo-groups of titanium oxide and its interface with an aqueous solution: the state of the art and a new approach. *Advances in Colloid and Interface Science* **2008**, *142*, 20-42.

(28) Vittadini, a.; Selloni, A.; Rotzinger, F. P.; Grätzel, M. Structure and energetics of water adsorbed at TiO_2 Anatase (101) and (001) Surfaces. *Physical Review Letters* **1998**, *81*, 2954-2957.

(29) Vittadini, A.; Casarin, M.; Selloni, A. Structure and stability of TiO_2 -B surfaces: A Density functional study. *The Journal of Physical Chemistry C* **2009**, *113*, 18973-18977.

(30) Vittadini, A.; Casarin, M.; Selloni, A. Hydroxylation of TiO_2-B: insights from density functional calculations. *Journal of Materials Chemistry* **2010**, *20*, 5871.

(31) Xu, Y.; Chen, W.-K.; Liu, S.-H.; Cao, M.-J.; Li, J.-Q. Interaction of photoactive catechol with TiO_2 anatase (101) surface: A Periodic density functional theory study. *Chemical Physics* **2007**, *331*, 275-282.

(32) Chen, J.; Franking, R.; Ruther, R. E.; Tan, Y.; He, X.; Hogendoorn, S. R.; Hamers, R. J. Formation of molecular monolayers on TiO2 surfaces: a surface analogue of the Williamson ether synthesis. *Langmuir* **2011**, *27*, 6879-89.

5.6 VASP References

G. Kresse and J. Hafner. Ab initio molecular dynamics for liquid metals. *Phys. Rev. B*, 47:558, 1993.

G. Kresse and J. Hafner. Ab initio molecular-dynamics simulation of the liquid-metal-amorphous-semiconductor transition in germanium. *Phys. Rev. B*, 49:14251, 1994.

G. Kresse and J. Furthmüller. Efficiency of ab-initio total energy calculations for metals and semiconductors using a plane-wave basis set. *Comput. Mat. Sci.*, 6:15, 1996.

G. Kresse and J. Furthmüller. Efficient iterative schemes for ab initio total-energy calculations using a plane-wave basis set. *Phys. Rev. B*, 54:11169, 1996.

PAW potentials

P. E. Blochl. Projector augmented-wave method. *Phys. Rev. B*, 50:17953, 1994.
G. Kresse and D. Joubert. From ultrasoft pseudopotentials to the projector augmented-wave method. *Phys. Rev. B*, 59:1758, 1999.

Generalized Gradient Approximation PBE (GGA-PBE)

J. P. Perdew, K. Burke, and M. Ernzerhof. Generalized gradient approximation made simple. *Phys. Rev. Lett.*, 77:3865, 1996.

J. P. Perdew, K. Burke, and M. Ernzerhof. Erratum: Generalized gradient approximation made simple. *Phys. Rev. Lett.*, 78:1396, 1997.